BONE MEASUREMENT IN RHEUMATOID ARTHRITIS

BONE EROSION MEASUREMENT

IN

SUBJECTS WITH RHEUMATOID ARTHRITIS

USING

MAGNETIC RESONANCE IMAGING

By

PATRICK D. EMOND, BSc, MSc

A Thesis

Submitted to the School of Graduate Studies

in Partial Fulfillment of the Requirements

for the Degree

Doctorate of Philosophy

McMaster University

DOCTORATE OF PHILOSOPHY (2011)	McMaster University
(Medical Physics)	Hamilton, Ontario

TITLE:	Volumetric bone erosion measurement in subjects with rheumatoid arthritis using magnetic resonance imaging
AUTHOR:	Patrick D. Emond, BSc. (Laurentian University), MSc. (McMaster University)
SUPERVISOR:	Christopher L. Gordon
NUMBER OF PAGES:	186

Abstract

Rheumatoid arthritis (RA) is a systemic disease that can affect the nervous system, lungs, heart, skin, reticuloendothelium and joints. Currently, the gold-standard measurement for tracking the progression of the disease involves a semi-quantitative assessment of bone erosion, bone marrow edema and synovitis, as seen in magnetic resonance (MR) images, by a musculoskeletal radiologist. The work presented in this thesis identifies how computer automation can be used to quantify bone erosion volumes in MR images without a radiologists' expert and time consuming intervention.

A new semi-automated hybrid segmentation algorithm that combines two established techniques: region growing and level-set segmentation, is described and evaluated for use in a clinical setting. A total of 40 participants with RA were scanned using a 1-Tesla peripheral MR scanner. Eight of the participant scans were used to train the algorithm with the remaining used to determine the accuracy, precision, and speed of the technique. The reproducibility of the hybrid algorithm and that of manual segmentation were defined in terms of intra-class correlation coefficients (ICCs). Both techniques were equally precise with ICC values greater than 0.9. According to a least squares fit between erosion volumes obtained by the hybrid algorithm with those obtained from manual tracings drawn by a radiologist, the former was found to be highly accurate (m=1.030, b=1.385: r-squared=0.923). The hybrid algorithm was significantly faster than manual segmentation, which took two to four times longer to complete.

In conclusion, computer automation shows promise as a means to quantitatively assess bone erosion volumes. The new hybrid segmentation algorithm described in this thesis could be used in a clinical setting to track the progression of RA and to evaluate the effectiveness of treatment.

Acknowledgements

This thesis is the culmination of several years of hard work which I could not have completed without the help and support of several people, each of which I wish to thank. My thesis adviser, Dr. Chris Gordon, guided me through both my Master's and Doctoral graduate studies. Without his support and advice I could have never completed this work. The nature of this thesis, which combines physics, rheumatology, radiology and computer science, required advice from a varying number of backgrounds. Dr. Colin Webber often reminded me to remember the basic science which is so important in developing a successful thesis. Dr. Rick Adachi provided me with the idea for this project which allowed me to apply my technical background to the medical sciences in a challenging and relevant manner. Dr. Dean Inglis, with whom I continue to work with on a variety of projects, introduced me to the world of medical visualization and analysis, a topic which still holds my interest. Over the course of my studies James Snetsinger, Sabrina Royal and Carly Shields endured my sometimes difficult company; I am thankful for the years we spent together in the House of Robes Divine. My parents, Roger and Pauline Emond, provided me with constant encouragement and cheer-leading, particularly when I needed it most. Finally, my wife, Kendra Fleck, whose continued love and support provided me with the perseverance which was necessary to successfully complete my graduate work.

Table of Contents

List of Figures

List of Tables

Chapter 1

Introduction

1.1 Rheumatoid Arthritis (Hochberg et al. 2003)

1.1.1 History

Rheumatoid Arthritis (RA) was given its name by Sir Alfred Baring Garrod in 1859. The first detailed medical description of RA was recorded by Landre-Beauvais of Paris in 1800 (Snorrason 1952, Short 1974). However, other descriptions of RA include Flemish paintings depicting joint deformities suggesting the occurrence of RA in the 15th, 16th and 20th centuries (Dequeker 1977, 1987), ancient descriptions by Hippocrates (460 BC) and Galen (2nd century) (Dieppe 1988), and new world paleopathological findings denoting RA-like erosive changes in bones dating as far back as 6500 BC (Rothschild and Woods 1990).

It is still not known when RA originated. Until recently, there was no evidence of the existence of RA prior to the 17th century. Unlike other forms of arthritis such as spondylitis, osteoarthritis (OA) and gout, unequivocal evidence of RA had not been identified in paleopathology. Due to the recent findings in the skeletal remains of pre-Columbian native-Americans and lack of such findings in the old world, it has been hypothesized that RA originated in the Americas and was transported back by explorers (Rothschild and Woods 1990). However, opposition to this theory include neolithic skeletal remains found in Sweden denoting erosive change compatible with RA (Leden et al. 1988), and disputes concerning the

interpretation of ancient skeletal remains (Rogers and Dieppe 1990). Overall, there is still no undeniable proof as to whether or not RA is a modern illness, or where it originated. Today, RA is identified by classification criteria created in 1958 and since revised in 1987 by Arnett et al.

1.1.2 Economics

RA imposes a staggering burden on the health care system and the lives of those affected by the disease. This burden is usually separated into two categories: direct costs, which include all health care costs, and indirect costs, which include lost wages and productivity. Due to the debilitating nature of RA, the indirect costs are usually equal to or greater than the direct costs of the disease, making it important to consider both types of economic burden.

A comprehensive study of the economics of RA and OA determined the direct and indirect costs to be US$64.8 billion in the United States in 1992, which is in the same order as the cost of coronary heart disease (Callahan 1998). The average annual individual direct cost of RA ranged from $2298 to US$13,549 in North America from 1981 to 2000 (Kvien 2004) and €1812 to €11,792 in North America and Europe from 1978 to 2002 (Rat and Boissier 2004). Maetzel et al. (2004) compared the economic burden of RA, OA and high blood pressure in Ontario, Canada, and found that direct costs of RA were 63% higher than OA and

138% higher than high blood pressure. Furthermore, they reported the indirect costs to be up to five times greater.

1.1.3 Classification

The classification of RA has changed several times over the study of the condition. The American Collage of Rheumatology (ACR) 1987 revised criteria for the classification of RA, defined by Arnett et al. (1988), is the currently accepted paradigm though it has recently been updated by the 2010 Rheumatoid Arthritis Classification Criteria (Aletaha et al. 2010). The criteria include seven features of interest (table 1.1) of which at least four must be fulfilled for a diagnosis of RA. Alternatively, classification of RA can be defined by a decision tree formulation (figure 1.1), where alternative variables based on swelling of the metacarpophalangeal (MCP) joints in place of radiographic changes and swelling of the wrist in place of rheumatoid factor are proposed. A number of studies examining the validity of the ACR 1987 criteria in clinical settings against the gold standard of physician diagnosis found that the sensitivity and specificity of the four of seven and decision tree formats of the criteria to be 66% to 95% and 74% to 98% for the four of seven format, respectively, and 71% to 96% and 89% to 96% for the decision tree format, respectively (Moens et al. 1992). Nevertheless, there is no agreed upon “gold-standard” for the classification of RA.

Table 1.1: The American College of Rheumatology (ACR) 1987 revised criteria for the classification of RA (Arnett et al. 1988)

	Criteria
1.	Morning stiffness lasting at least 1 hour
2.	Soft tissue swelling of 3 or more joint areas
3.	Swelling of the hand or wrist joints
4.	Bi-lateral swelling for at least 6 weeks
5.	Rheumatoid nodules
6.	Positive rheumatoid factor
7.	Radiographic changes in hand or wrist joints

Table 1.2: The range of overall prevalence and incidence as reported by 4 review articles, excluding data from Native Americans.

	Continents	**Prevalence (per 1000)**	**Incidence (per 1000)**
Gabriel (2001)	Europe and North America	2.1 - 17.8	0.038 - 0.75
Kvien (2004)	Europe and North America	4.0 - 30.0	0.09 - 0.75
Alamanos and Drosos (2005)	Africa, Asia, Europe and North America	0.0 - 11.0	0.10 - 3.0
Alamanos et al. (2006)	Asia, Europe and North America	1.8 - 10.7	0.10 - 0.5

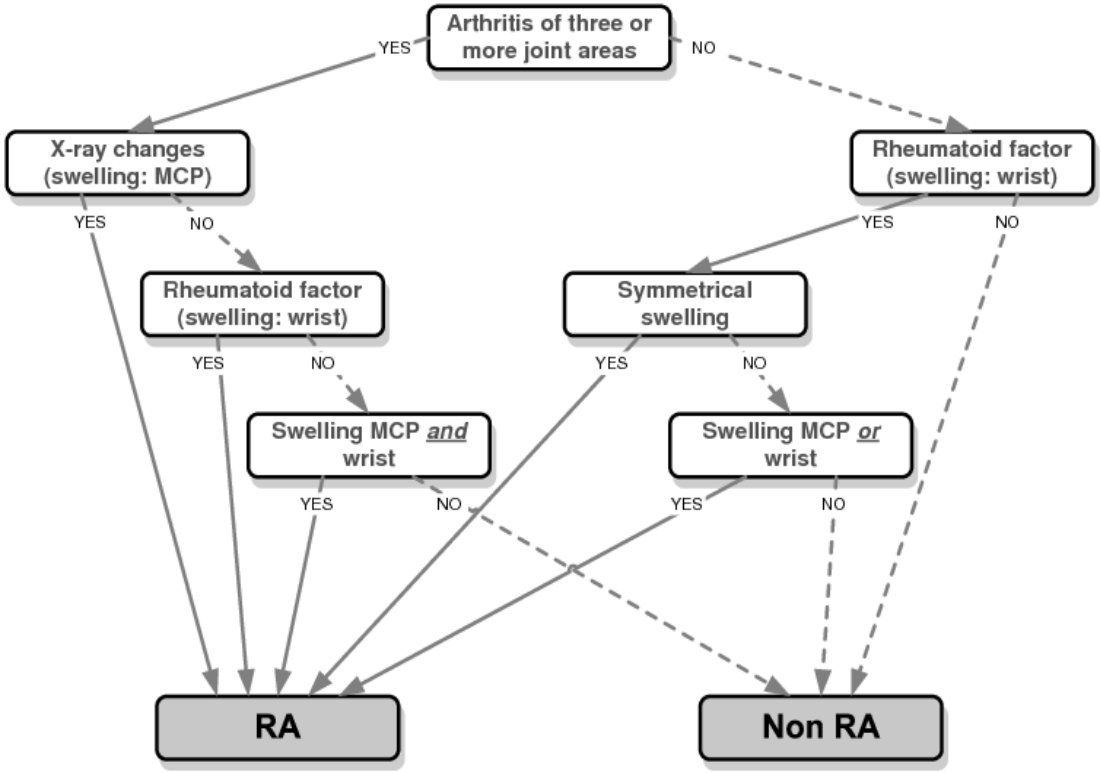

Figure 1.1: The ACR 1987 criteria as a classification tree. Variables in parentheses can be used when data on the first listed variable is unavailable (From MacGregor (1995)).

Though it has been shown that the ACR 1987 criteria is effective for long standing RA, it has been criticized as inadequate for the early diagnosis of the disease since the last 3 items of the criteria, rheumatoid nodules, positive rheumatoid factor and radiographic changes, are often not present in the early stages of the disease (Aletaha et al. 2005, Moens et al. 1992, Saraux et al. 2001).

1.1.4 Epidemiology

Two common metrics in epidemiology are prevalence, the number of people affected by a condition at any particular time, and incidence, the number of annual new occurrences of a condition. Determining the prevalence and incidence of RA poses several challenges due to poor understanding of the etiology of the disease. The ACR 1987 revised criteria for the classification of RA is most widely accepted as a standard for use in characterizing the distribution of RA in populations. However, as described in the section above there is no ideal method for the classification of the disease. Furthermore, due to the low occurrence of RA very few studies have had enough statistical power to adequately perform epidemiological measurements. The ranges of prevalence and incidence of RA, as reported in a number of review articles, are listed in table 1.2.

It has been observed that the incidence of RA is higher in women than men, and increases with age (Alamanos and Drosos 2005, Gabriel 2001, Kvien 2004,

Symmons et al. 2002). In general, most autoimmune diseases are predominant in women, with possible explanations being differences in exposure, chronobiology of X and Y chromosomes, though the latter has not been thoroughly examined (Lockshin 2006). The incidence rate of RA in the Norwich Health Authority, England, as defined by the decision tree format of the ACR 1987 criteria, grouped by age, shows a positive correlation between incidence and age for both sexes, with a stronger trend in women than men (figure 1.2). A follow-up by Symmons et al. in 2002 concluded that the prevalence of RA in women had decreased over the past 50 years.

An important epidemiological finding is the higher occurrence of RA in Native Americans compared to most other populations. Ferucci et al. (2005) have compiled 15 studies examining prevalence in 13 distinct Native American populations. Of the 13 groups, the prevalence of the Tlingit, Yakima, Pima and Chippewa populations were many times greater than non-native populations, ranging from 2.4% to 7.1%. This finding is important since it may help to explain what roles genetic and environmental factors may play in the etiology of RA.

It has been hypothesized that the global incidence of RA has been declining over the past 50 years (figure 1.3). The cause of the observed decline is not known, though change in classification of RA in addition to an increase of patients with

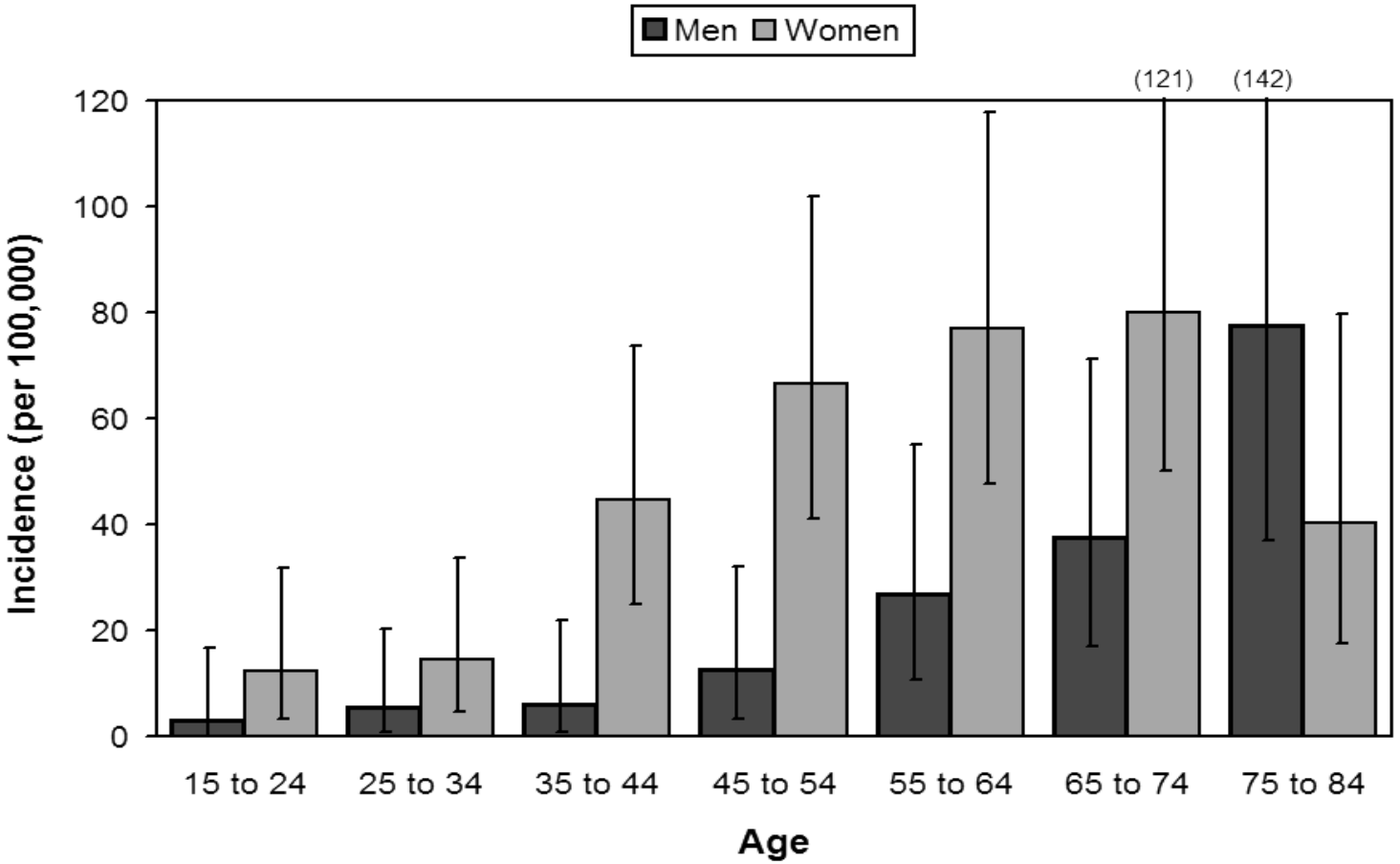

Figure 1.2: Incidence of RA in the Norwich Health Authority defined by the decision tree format of the 1987 ACR criteria, grouped by age. The error bars represent the 95% confidence intervals (adapted from Symmons et al. (1994)).

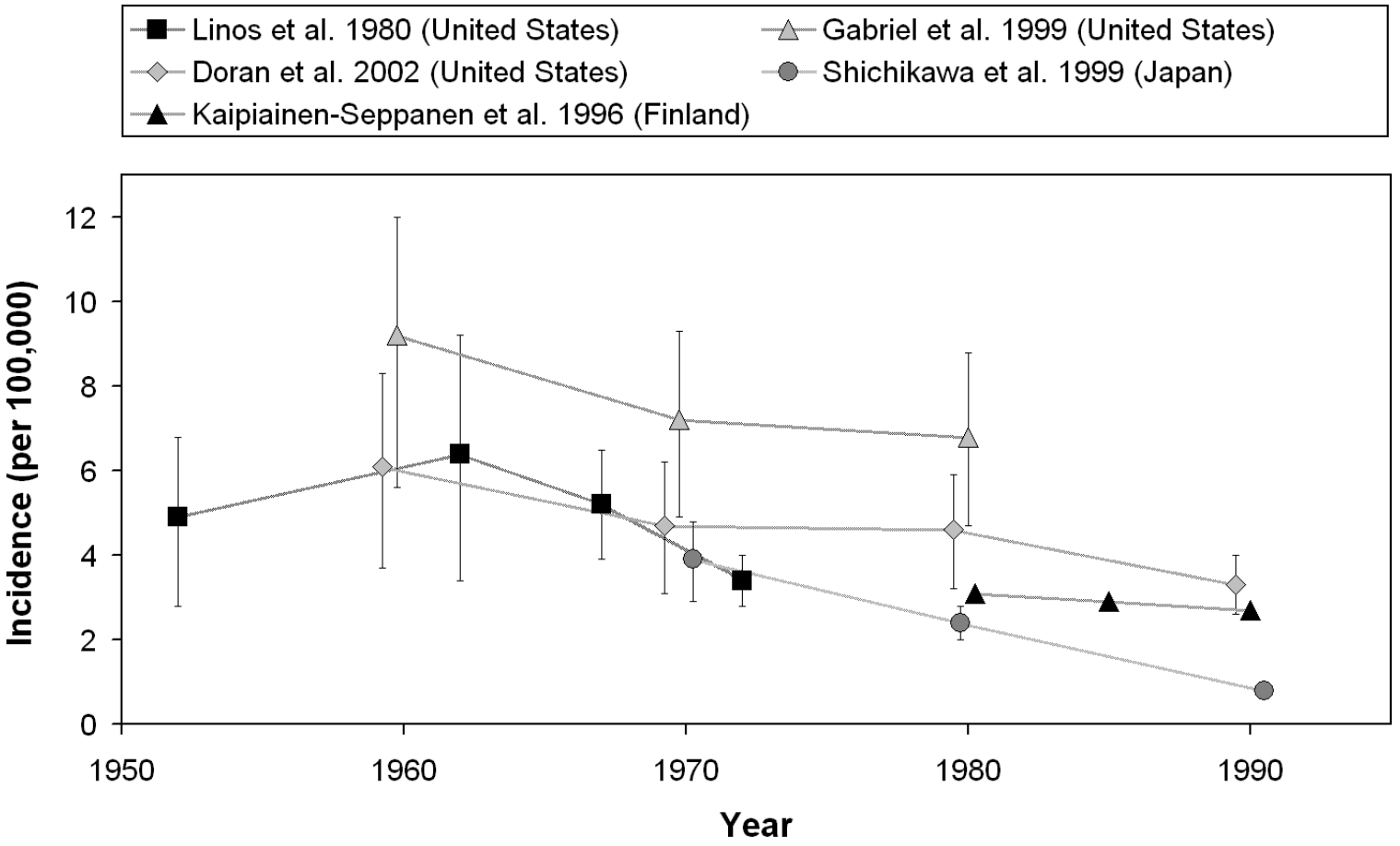

Figure 1.3: RA incidence trends in the United States, Finland and Japan. Vertical lines represent upper and lower ranges taken from female and male incidences, respectively (from Kvien (2004), in which full references are given).

uncategorized arthritis has been put forth as an alternative to actual decline in the incidence of RA (Uhlig and Kvien 2005).

1.1.5 Etiology and Pathology

Though many observations have been made about the causes of RA, the specific etiology remains unknown. Bacterial antigens have been identified as playing a role in the inflammatory response through the interaction with T lymphocytes (Miller-Blair et al. 1996). Genetic factors contributing to RA have also been investigated. In particular, linkage and association studies have been used to explore genetic associations (Orozco et al. 2006). The initiation of RA is assumed to be a complex combination of genetic, environmental and infectious agents (Weyand 2000, Alamanos and Drosos 2005) that is still poorly understood. More recently, there has been evidence that smoking in the genetically predisposed individual may cause RA, particularly in those who are anti-cyclic citrullinated positive (Mahdi et al 2009, Vittecoq et al 2008), an antibody which targets the body's proteins and is commonly found in people with RA. The anti-cyclic citrullinated biomarker has been added to the 2010 RA classification criteria (Aletaha et al. 2010).

RA is a systemic disease that can affect the nervous system, lungs, heart, skin, reticuloendothelium and joints. Bone and joint involvement include inflammation, synovitis, pannus, bone edema and erosion, cartilage loss and gross deformity,

usually found in the hands, wrists, elbows, shoulders, knees, ankles and feet. A comparison of a normal joint and one affected by RA is illustrated in figure 1.4. Synovitis, labeled in figure 1.4(b) as (I), is inflammation of the synovial membrane which encapsulates synovial fluid. The inflammation causes the joint capsule to visibly swell, a symptom included in the ACR 1987 classification criteria. Synovitis has been closely investigated as a means to investigate the pathophysiologic mechanisms of RA (Tak and Bresnihan 2000). Pannus, labeled in figure 1.4(b) as (III), occurs when inflammation overgrows the articular surface, causing synovial tissue to breakdown. One of the hallmark effects of RA is the destruction of bone within the joint capsule. Bone edema, labeled in figure 1.4(b) as (IV), is visualized as an area of free water with poorly defined margins in magnetic resonance (MR) images replacing bone marrow fat. As edema progresses, the cortical shell within the joint capsule is broken and bone is eroded by the inflamed synovium. The erosion of bone, labeled in figure 1.4(b) as (V), is also included in the ACR criteria as radiographic change. Since bone edema is not visible in conventional radiography (CR) it has only been studied since the advent of MR imaging. In a review article, McQueen and Ostendorf (2006) suggest that bone edema may play the dominant role in the immunopathogenesis of RA instead of synovitis. This suggests that the causal link between bone edema and inflammation may begin with edema instead of inflammation. Another hypothesis is that inflammation results from edema.

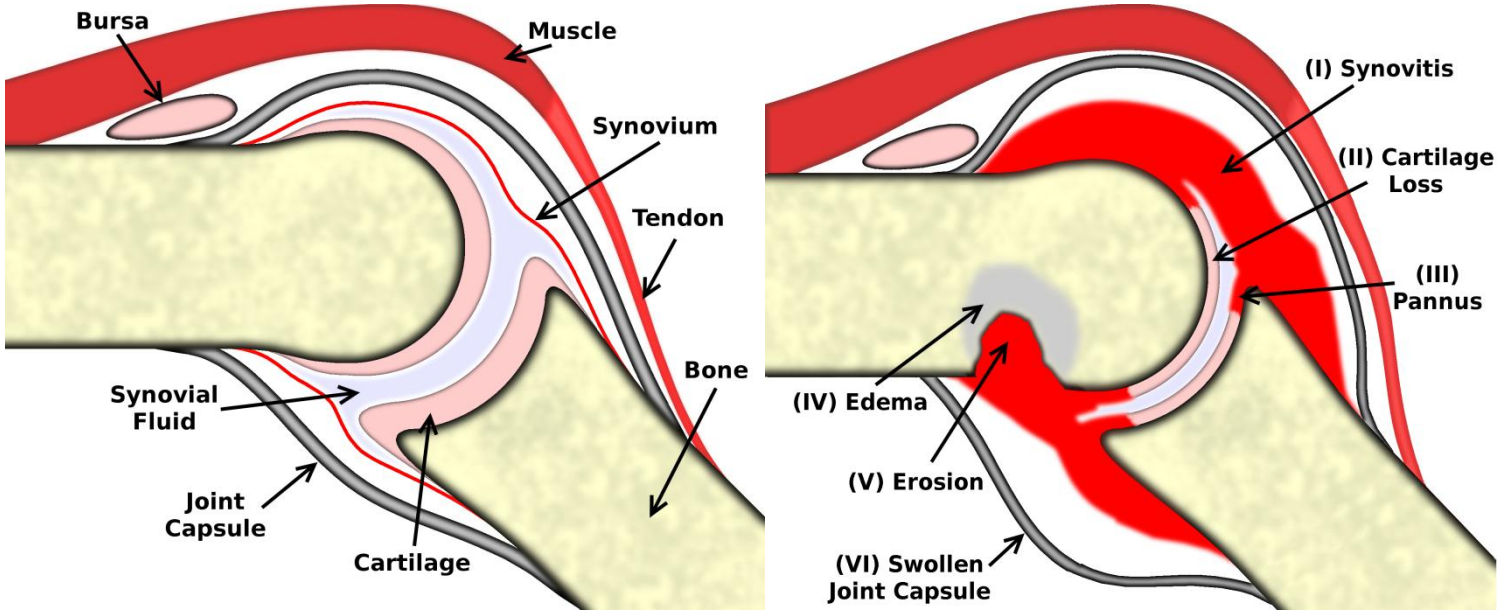

(a) Healthy joint

(b) RA joint

Figure 1.4: A comparison of a normal joint and a joint affected by rheumatoid arthritis.

Erosions are caused by osteoclasts that have been activated by the inflammatory process. Erosions do not repair because the pannus and inflammatory tissues release factors that inhibit osteoblastic bone repair (Goldring 2009). Finally, cartilage loss, labeled in figure 1.4(b) as (II), and, if the disease is left untreated, gross deformity of the joint can occur.

1.1.6 Treatment

There are a number of different treatments used to manage RA which fall into one of three categories: Non-Steroidal Anti-Inflammatory Drugs (NSAIDs), corticosteroids, and Disease Modifying Antirheumatic Drugs (DMARDs). NSAID treatments reduce inflammation which in turn reduces pain and increases function in affected joints. Corticosteroids reduce inflammation and help to control the auto-immune responses caused by RA. Finally, DMARD treatments modify disease activity by improving symptoms and retarding outcomes. Since DMARDS have a longer onset time than other treatments they are often paired with inflammation reducing therapies.

More recently, powerful new DMARDs, in particular the TNF inhibitors (agents which block TNF cytokines), Adalimumab, Etanercept and Infliximab, have been shown to work faster than conventional DMARDs and are recommended for the treatment of moderate to severe RA in order to inhibit structural damage. However, these so-called biologics incur a much higher cost than conventional

DMARDs. Pucino et al. (2006) determined the annual cost of TNF antagonists to be up to $38,992 for Adalimumab, $19,496 for Etanercept and up to US$62,816 for Infliximab. Due to these biologics costing several times more than conventional DMARDs, their use is controversial (Bansback et al. 2005).

The efficacy of TNF inhibitors was demonstrated in a review article by Alonso-Ruiz et al. (2008) using the ACR efficacy response criteria, wherein ACR20, ACR50 and ACR70 responses correspond to 20, 50 and 70% improvement, respectively. The adverse effects of treatment were calculated in terms of Relative Risk (RR), which is defined as:

$$RR = \frac{p'(treated)}{p'(control)} \tag{1.1}$$

where p'(treated) and p'(control) are the probabilities of adverse effects in the treated and control groups, respectively. The beneficial effects of treatment were calculated in terms of Number Needed to Treat (NNT), which is defined as:

$$NNT = \frac{1}{p(treated) - p(control)} \tag{1.2}$$

where p(treated) and p(control) are the probabilities of attaining response in the treated and control groups, respectively. The NNT and RR values for

Adalimumab, Etanercept and Infliximab for ACR20, ACR50 and ACR70 are presented in table 1.3.

Adverse effects of TNF inhibitors include serious infections and risk of cancer. In a review article by Cunnane et al. (2003), the links between biological agents and infection are discussed. In short, these inhibitors interfere with TNF cytokines which are important for fighting infection. The exact nature of this interaction is still under investigation. The relationship between biological agents and risk of cancer is less clear. In a review article by Williams (2008), TNF inhibiting therapies are reported to potentially facilitate or inhibit the development of cancer.

1.2 Imaging Rheumatoid Arthritis

1.2.1 Overview

Modern medical imaging has provided many different techniques for the visualization of anatomy. Such techniques include conventional radiography (CR), computed tomography (CT), ultrasonography (US) and magnetic resonance (MR) imaging. Each of these methods has distinct benefits and limitations due to their reliance on different physical principals. For example, CR and CT rely on the differences in linear attenuation characteristics between human tissues in order to differentiate between them. At diagnostic energies, the X-ray attenuation of

Table 1.3: NNT and RR values of three anti-Tumour Necrosis Factor (TNF) drugs (From Alonso-Ruiz et al. (2008)). Values are provided for the American College of Rheumatology (ACR) ACR20, ACR50 and ACR70 response criteria which represent 20%, 50% and 70% improvement, respectively. NS denotes non-significant results.

	ACR	**NNT**	**RR (CI 95%)**
Adalimumab	ACR20	5 (4-6)	2.0 (1.3-2.9)
	ACR50	5 (5-6)	2.8 (1.6-4.7)
	ACR70	7 (6-8)	3.5 (1.9-6.7)
Etanercept	ACR20	6 (5-8)	1.7 (1.1-2.7)
	ACR50	6 (4-7)	2.2 (1.1-4.3)
	ACR70	NS	2.1 (0.9-4.5)
Infliximab	ACR20	5 (4-6)	1.7 (1.1-2.6)
	ACR50	6 (5-7)	2.2 (1.2-4.1)
	ACR70	9 (7-13)	2.4 (1.2-5.0)
Combined	ACR20	5 (5-6)	1.8 (1.4-2.3)
	ACR50	5 (5-6)	2.4 (1.7-3.4)
	ACR70	7 (7-9)	2.7 (1.8-4.1)

bone is much greater than that of soft tissue, enabling excellent visualization of bone without obfuscation of the other surrounding tissues. However, since there is little to no difference in the attenuation between different soft-tissues, such as water, fat and muscle, radiation-attenuation based techniques are not ideal for visualizing non-osseous features in anatomy. Whenever possible, this limitation in attenuation differences is overcome by using contract agents. MR imaging relies on a different physical principle for image acquisition than CR and CT, nuclear magnetic resonance, making it an ideal technique for visualization of non-osseous tissues.

1.2.2 Conventional Radiography

The etiopathogenesis of RA has been explored using a variety of imaging techniques. CR is widely used in the diagnosis and monitoring of RA due to it being inexpensive and highly available. However, as outlined in section 0, early development of RA involves changes to non-osseous tissue which CR is unable to detect. Furthermore, CR is limited to 2D projections of 3D anatomy and, despite superior resolution, it is not as sensitive and does not detect erosions as early as 3D imaging techniques (McQueen et al. 1998, Sugimoto et al. 1996, Jorgensen et al. 1993, Foley-Nolan et al. 1991). Since there is no known way to reverse severe damage to bone caused by RA, early detection is of high priority. For this reason

CR, though useful in the monitoring of more advanced RA, is not ideal for imaging the condition in its early stages.

1.2.3 Computed Tomography

CT has the advantage over CR of tomographic visualization which overcomes the limitations of projection-based 2D images. However, this comes at the cost of much greater radiation exposure. Furthermore, like CR, the types of soft tissues that CT is able to image is limited by the relatively small differences in linear attenuation characteristics of non-osseous tissue. This limitation makes it inferior to imaging techniques able to clearly differentiate soft-tissue from fluids, such as MR imaging, because important early features of RA such as bone edema, synovitis and tenosynovitis all involve fluid in and around soft tissue. Because of its deficiencies in differentiating fluid from soft tissue without the use of contrast agents, CT is unable to provide valuable information concerning early RA, and as such it is considered to be inferior to MR and US for evaluation of early RA (McQueen et al. 1998, Jorgensen et al. 1993, Foley-Nolan et al. 1991).

As previously described in section 0, bone erosions do not manifest as early as inflammation but they have been identified on MR and CT images in early RA. CT images are excellent for the delineation of erosions since their signal is clearly diminished compared to the cortex and surrounding trabecular bone (Perry et al. 2005). Due to CT yielding better images of bone than MR and US it has been

used as a reference, in the absence of a better standard, to validate the imaging of erosions (Dohn et al. 2006, Oostveen et al. 1998, Perry et al. 2005). However, although CT may be superior for imaging bone to MR, the two share similar limitations in terms of in and out of plane resolution compared to erosion size. Therefore, microscopic CT images, such as those acquired by micro-CT scanners, would better serve the purpose of validating MR images. To the author's knowledge no such comparisons have ever been made.

1.2.4 Magnetic Resonance Imaging

MR measures the response of elements to changing magnetic fields. In particular, medical MR imaging primarily relies on the magnetic resonance of hydrogen, which is found throughout most tissues in the body. The major advantage this technique has over X-ray based imaging is that MR images to not require ionizing radiation, so there is no radiation dose associated with image acquisition. Another advantage of MR is that images are taken as slices along any plane, overcoming the inherent limitations of CR caused by projection. As well, there are a multitude of pulse sequences and timings that can be used to improve the contrast resolution between different features of interest. For example, the Rheumatoid Arthritis Magnetic Resonance Image Scoring (RAMRIS) system recommends the use of T1-weighted and T2-weighted images (explained in chapter 2) for the scoring of bone erosions and edema, respectively (Ostergaard et al. 2003a). The challenge

involves a thorough understanding between MR configuration and RA pathology to best visualize features of interest.

As with any imaging technique, MR imaging has its disadvantages. Depending on the pulse sequence used, desired resolution, Field of View (FOV) and Signal to Noise Ratio (SNR), scan times can become excessively long. The better the resolution, greater the FOV and SNR the more time is necessary for image acquisition. Long scan times are undesirable because of the discomfort it causes patients and the increased chance of movement artifact. As well, out of plane resolution must be limited in order to produce an adequate signal. Setting a large slice thickness or low resolution may cause Partial Volume Effects (PVEs) which misrepresent contours and can obfuscate smaller features altogether. Other artifacts inherent in MR imaging that can cause the misrepresentation of the features of RA include susceptibility, chemical shift, truncation and inhomogeneity of fat suppression (McQueen et al. 2005). The causes and appearance of various MR imaging artifacts are described in section 2.3.2.

Some of the limitations of MR imaging can be overcome by specialized scanners designed for particular functions. In particular, peripheral Magnetic Resonance Imaging (pMRI) uses small-bore systems that have been developed specifically for extremity exams. Typical low-field pMRI scanners usually have a main field of 0.2T (Tesla), 0.23T or 0.6T and are limited to low resolution imaging. In

contrast, the main field strength of high-field pMRI scanners are at least 1.0T and have been reported to provide equivalent signal and resolution to large-bore 1.5T scanners (Beattie et al. 2005, Inglis et al. 2007).

Though small-bore scanners are limited to scanning the extremities only, they have advantages over large-bore high-field scanners. Some MR artifacts are less of a concern in pMRI. For example, chemical shift grows linearly with main field strength so artifacts using 1.0T fields will be three times smaller than in 3.0T fields. Movement artifact can be caused by discomfort and claustrophobic reactions in some patients. Due to small-bore pMRI requiring a single limb to be surrounded by a substantially smaller magnet, such anxieties are not an issue. Finally, pMRI is much less expensive than imaging with large-bore MR scanners which, in combination with the high quality images provided by high field pMRI, makes it ideal for imaging RA in the hand and wrist.

1.3 Scoring Rheumatoid Arthritis

1.3.1 Traditional Radiography

Several methods have been developed to track erosion changes in CR, CT and MR images, as compared in Table 1. Historically, X-ray based evaluations were originally scored by a single qualitative measure categorizing damage on a scale of 0 to 4 (Steinbrocker *et al* 1949), 0 to 5 (Kellgren 1956) and 0 to 8 (Sievers

1965). Later, methods assessing joints individually were introduced by Sharp *et al* (1971) and Larsen (1973), which in turn have been modified by several groups (Gofton and O'Brien 1982, Genant 1983, Bluhm *et al* 1983, van der Heijde *et al* 1989). The Sharp and modified Sharp methods categorize erosive damage and joint space narrowing in individual joints and aggregate the result into a single score (Aletaha and Smolen 2006). Erosion size and joint spacing have also been measured quantitatively in CR using digital image processing techniques (Higgs *et al* 1996, Angwin *et al* 2004).

1.3.2 Computed Tomography

No qualitative scoring method has been developed specifically for CT images. Measurement of erosion volume in CT images is described by Duryea *et al* (2008) which involves a semi-automated method for contouring carpal bones, then determining erosion volume by comparing baseline and follow-up images. An assessment of RA in CT images was performed in a clinical trial by Dohn *et al* (2008) using the Rheumatoid Arthritis Magnetic Resonance Image Scoring (RAMRIS) system which is intended for MR images.

1.3.3 Magnetic Resonance Imaging

3D MR imaging is currently the accepted standard for assessing bone and joint changes associated with RA (Peterfy 2004). MR based evaluations of RA can be

divided into semi and fully quantitative measurements. The Outcome Measures In Rheumatology Clinical Trials (OMERACT) RAMRIS system, the established gold standard in radiological assessment of RA and described by Ostergaard *et al* (2003), assesses synovitis, bone edema and bone erosion individually. Synovitis is assessed on a scale from 0 to 3 (none, mild, moderate and severe), edema on a scale from 0 to 3 (none, one third, two thirds and full) and erosions on a scale from 0 to 10 (none, 10%, 20%, etc). Bone erosions are identified as regions within trabecular bone having low signal in T1-weighted images (absence of marrow signal) (Ostergaard *et al* 2003, Sommer *et al* 2005). Erosion volumes have been measured in T1-weighted images by Bird *et al* (2003) using manual tracing and Carano *et al* (2004) by comparing baseline and follow-up scans to quantify change in erosion volume. Manually traced contours in 3D images are, arguably, the most direct quantitative image-based measurement of bone erosions. Manual tracing, although time consuming, can be accurate when performed by a trained radiologist and can serve as a gold standard for the purpose of validating automated segmentation algorithms (Duryea *et al* 2000a, 2000b, Gordon *et al* 2001).

1.4 Purpose of thesis

Though a number of methods have been developed for the quantitative assessment of RA, none of them are adequate to be used in tracking the radiological changes

in early RA. The purpose of this thesis was to determine how automated segmentation algorithms could be used to quantitatively track the changes in early RA using MR images. Baseline and follow-up scans of a small cohort of patients were used to determine the accuracy and reproducibility of volume-based measurements of bone erosions using a newly developed hybrid segmentation algorithm.

Chapter 2

Magnetic Resonance Imaging

2.1 Magnetic Resonance Physics

2.1.1 Nuclear Spin

The basis of MR imaging is the energetic interactions between an external magnetic field, radio frequency (RF) pulses and the nuclear magnetic moment associated with the nuclear spin of a molecule. Nuclear spin, *I*, is defined as the total angular moment of a nucleus which is determined by the total number of protons and neutrons within the nucleus. All nuclides with an even number of protons and neutrons have nuclear spin $I = 0$, whereas all other nuclides exhibiting an odd number of protons, neutrons or both have spin $I \neq 0$. Nuclides with non-zero spin are often referred to simply as spins. Applying an external magnetic field, $\vec{B}_0$, to a spin will cause energetic interactions between the field and the magnetic moment of the spin. This interaction is the basis behind MR imaging.

A magnetic moment, in terms of classical physics, can be described as a vector $\vec{M}$, precessing around the z-axis. As depicted in figure 2.1, this vector can then be broken down into its longitudinal component, M_z, which lies along the z-axis, and its transverse component, M_r which lies along the radial axis. When an external magnetic field, $\vec{B}_0$, is applied along the z-axis, the magnetic moments of

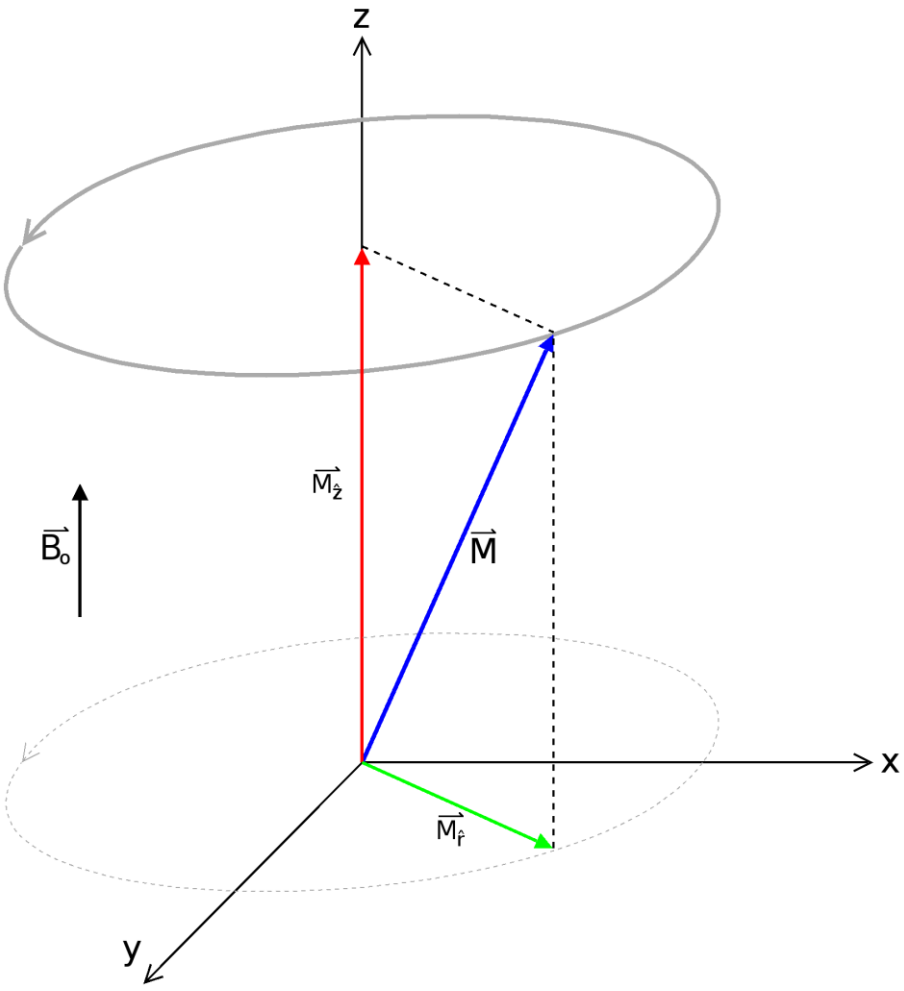

Figure 2.1: A classical representation of a magnetic moment, $\vec{M}$, that, in the presence of an applied external magnetic field $\vec{B}_0$, precesses around the z-axis. $\vec{M}$ is composed of a longitudinal component, $M_z\hat{z}$, and transverse component, $M_r\hat{r}$.

spins align themselves with the magnetic field in either a low or high energy state. The low energy state, often called parallel spin, is defined as having a net magnetization pointing in the same direction as $\vec{B}_0$. Conversely, the high energy state, often called anti-parallel spin, has a net longitudinal component pointing in the opposite direction to $\vec{B}_0$. If there is an uneven number of parallel and anti-parallel spins the overall effect causes a net longitudinal magnetization. This is illustrated in figure 2.2(a). A similar, but importantly distinct concept is transverse magnetization which occurs when the transverse component of spins rotate in phase. As spins naturally exhibit random phase, they produce an overall null transverse magnetization. This is illustrated in figure 2.2(b). Unlike in the longitudinal direction, $\vec{B}_0$ does not produce a net transverse magnetization since it does not affect spin phase. Common nuclides associated with MR images include ^{1}H, ^{13}C, ^{19}F, ^{23}Na and ^{31}P. Due to its abundance in the body and high sensitivity to magnetic resonance, the hydrogen nucleus (^{1}H) is most often used in medical imaging. Therefore, throughout this section, if not otherwise stated, the term spin will refer specifically to a ^{1}H nucleus.

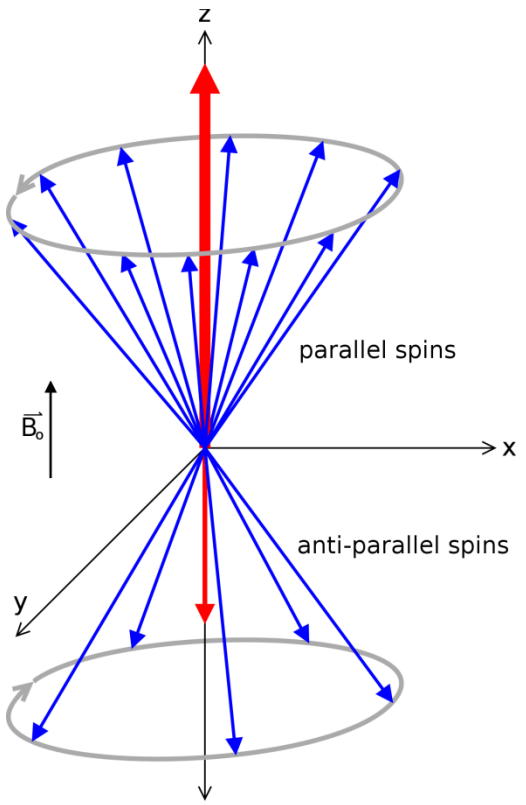

(a) Net Longitudinal Magnetization

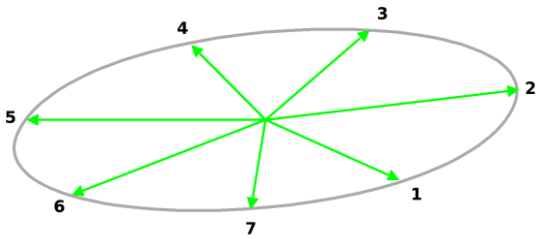

(b) Spin Phase

Figure 2.2: (a) A classical representation of net longitudinal magnetization. Each blue arrow is an individual spin precessing around the z-axis. Spins with a z-component in the same direction as the external field $\vec{B}_0$ are considered to have parallel spins while the anti-parallel spin states have z-components opposite of $\vec{B}_0$. The large, upward pointing red arrow represents the net longitudinal component of parallel spins and the smaller, downward pointing red arrow represents the net longitudinal component of anti-parallel spins. (b) The transverse components of multiple spins which are out of phase.

2.1.2 Excitation and Relaxation

The resonant frequency with which a magnetic moment precesses about the applied field axis is called the Larmor frequency, ω_o. The Larmor equation given in equation 2.1 shows that ω_o is directly proportional to the applied field:

$$\omega_o = \gamma B_0 \tag{2.1}$$

where γ is the gyromagnetic ratio, a constant unique to each nuclide. For example, the gyromagnetic ratio for ^{1}H is 42.58 MHz/Tesla.

By using an RF coil to apply an RF pulse, B_1, to spins in a magnetic field, but perpendicular to that field (in the radial direction), all molecules whose Larmor frequency match that of the applied RF pulse will experience magnetic resonance. Therefore, by applying an RF pulse at 42.58 MHz in a 1 Tesla magnetic field, the energetic interaction between the ^{1}H molecules and the pulse will resonate. When this occurs the resonant molecules absorb electromagnetic energy, a process known as excitation. Once B_1 is removed, spins will gradually return to their previous ground state by emission of electromagnetic energy, a process known as relaxation.

Depending on the duration of the applied RF pulse, both longitudinal and transverse magnetization is affected. In terms of quantum physics, B_1 excites the

proton of the hydrogen nucleus into a higher state, converting it from the lower energy parallel spin to the higher energy anti-parallel spin. The longer the pulse is applied, the more ^{1}H molecules are excited. In the classical model this appears as the net longitudinal magnetization decreasing as the number of parallel and anti-parallel spins reach equilibrium, then increasing in the opposite direction to the magnetic field as the number of anti-parallel spins grow more numerous than parallel spins. Figure 2.3 demonstrates how, in the classical model, the absorption of energy from the RF pulse "pushes" the spins into the transverse plane, effectively decreasing the longitudinal component and increasing the transverse component of the spin. The angle which defines how far spins are pushed into the transverse plane is defined as the flip angle, ϕ. The RF pulse also affects spin phase. As the net longitudinal magnetization decreases there is a phase coherence in spins which cause a net transverse magnetization. Figure 2.4 demonstrates how increasing energy from the RF pulse causes spin phase to align, thus creating a net transverse magnetization. A pulse that eliminates net longitudinal magnetization and maximizes net transverse magnetization has a 90° flip angle.

After the applied B_1 RF pulse is turned off, spins emit the electromagnetic energy they absorbed during excitation by returning to equilibrium (net longitudinal magnetization and no transverse magnetization due to spins dephase). This time-signal is known as Free Induction Decay (FID) and is the basis of MR imaging.

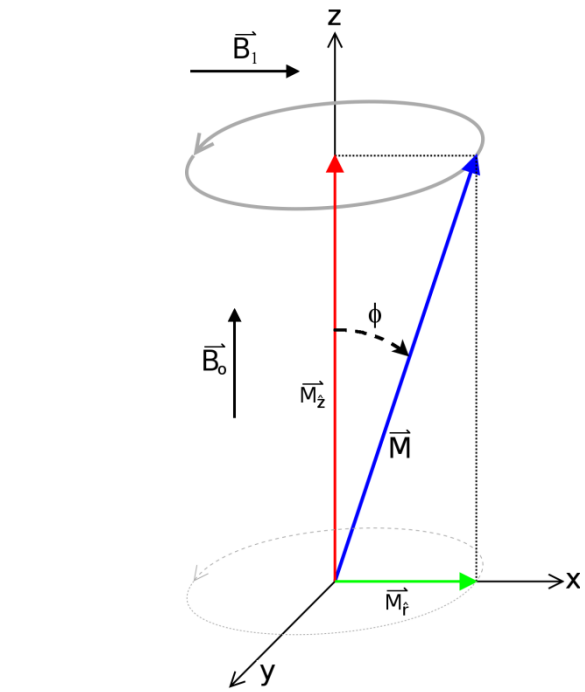

(a) Lower energy state

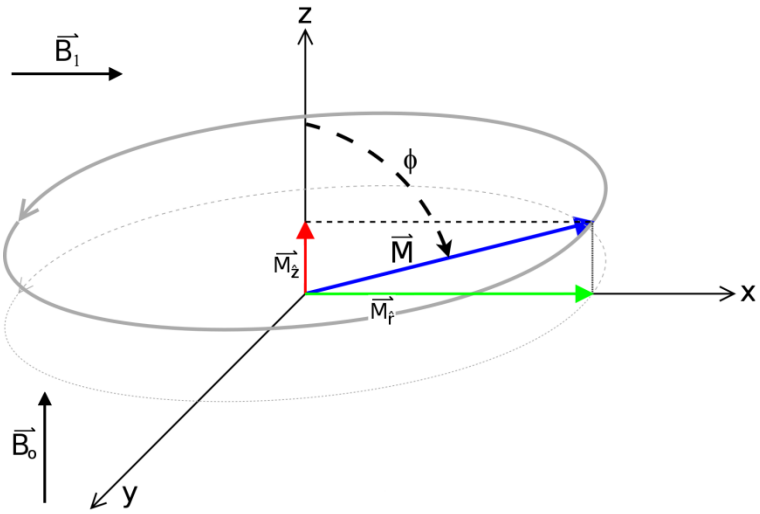

(b) Higher energy state

Figure 2.3: Increased energy states shorten the longitudinal magnetization (red arrow) and lengthen the transverse magnetization (green arrow). If $\vec{B}_1$ is applied long enough the net magnetization will only have a transverse component, or a 90° flip angle.

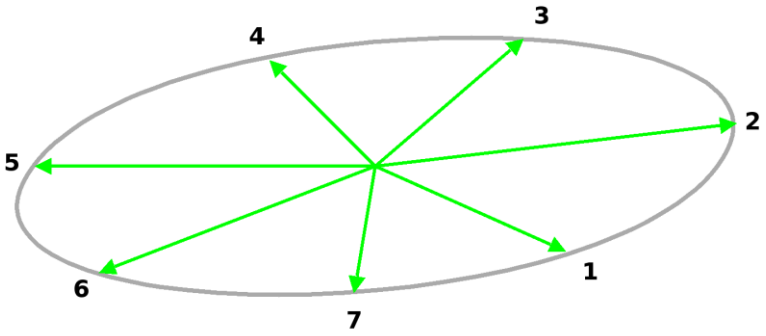

(a) Out of phase

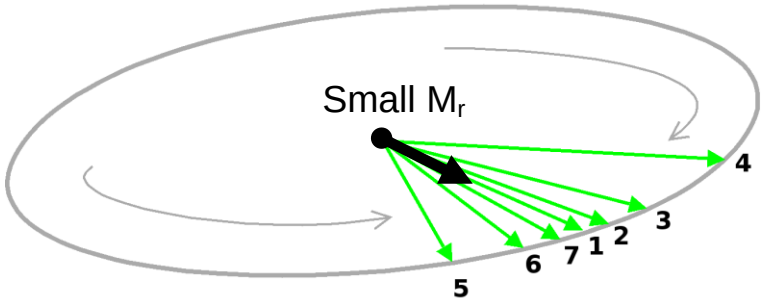

(b) Nearly in phase

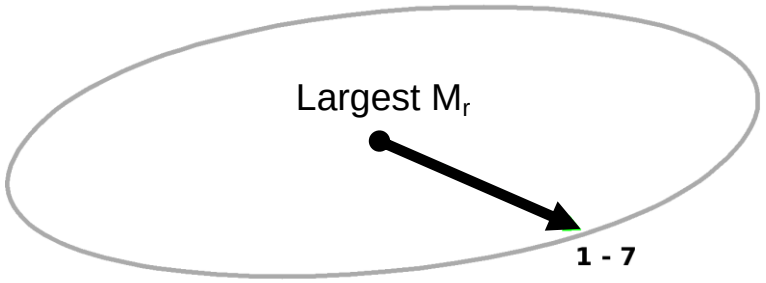

(c) In phase

Figure 2.4: As the individual spins become increasingly in phase the transverse magnetization, M_r, increases.

Faraday's Law of Induction states that an Electro-Magnetic Force (EMF) will occur in any coil when in a changing magnetic field:

$$V_{EMF} = -N\frac{d\Phi}{dt} \tag{2.2}$$

where N is the number of turns in a wire coil and Φ is magnetic flux. As spins relax by FID their net magnetization act as a changing magnetic field and in turn induce an EMF in the same coil that created the RF pulse, or any other coil within the main field. FID is characterized by two components, one from the longitudinal component and the other from the transverse component of the magnetic moment of spins. In the absence of B_1 spins gradually move from the higher energy, anti-parallel state to the lower energy, parallel state. As this change in energy states occurs, the overall net longitudinal magnetization is re-established at a rate described by the curve in figure 2.5(a). The rate at which M_z is re-established is dependent on the strength of Bo, tissue type and proton density.

By definition, the time required for M_z to return to 63% of maximum for a particular tissue is called the T_1 time. During relaxation the net transverse magnetization that was created by B_1 will decay as shown in figure 2.5(b). The rate at which this decay occurs also depends on the strength of Bo, tissue type and proton density. By definition, the time required for M_r to return to 37% of maximum for a particular tissue in a homogeneous magnetic field is called the T_2

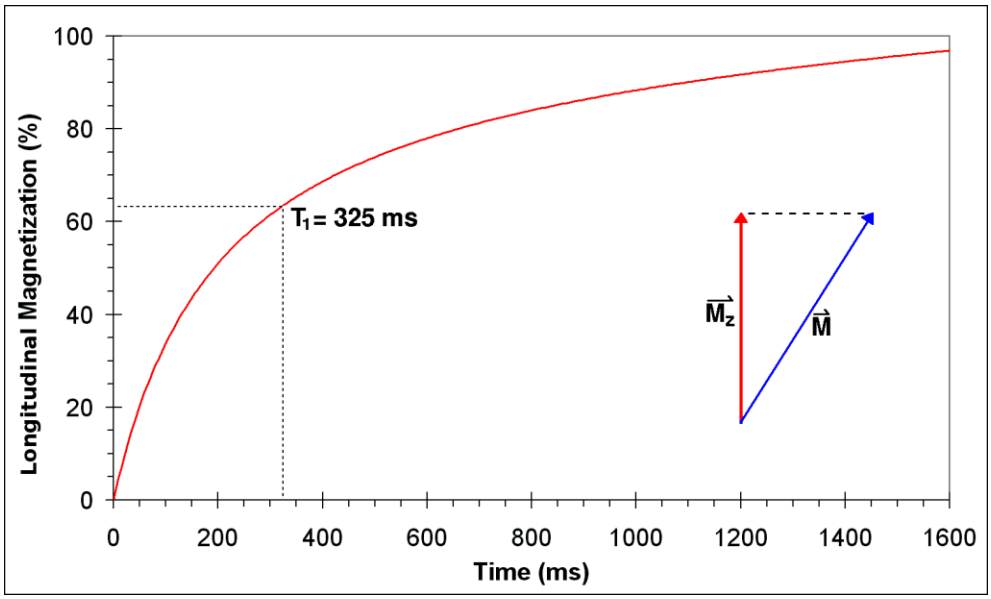

(a) Longitudinal Relaxation

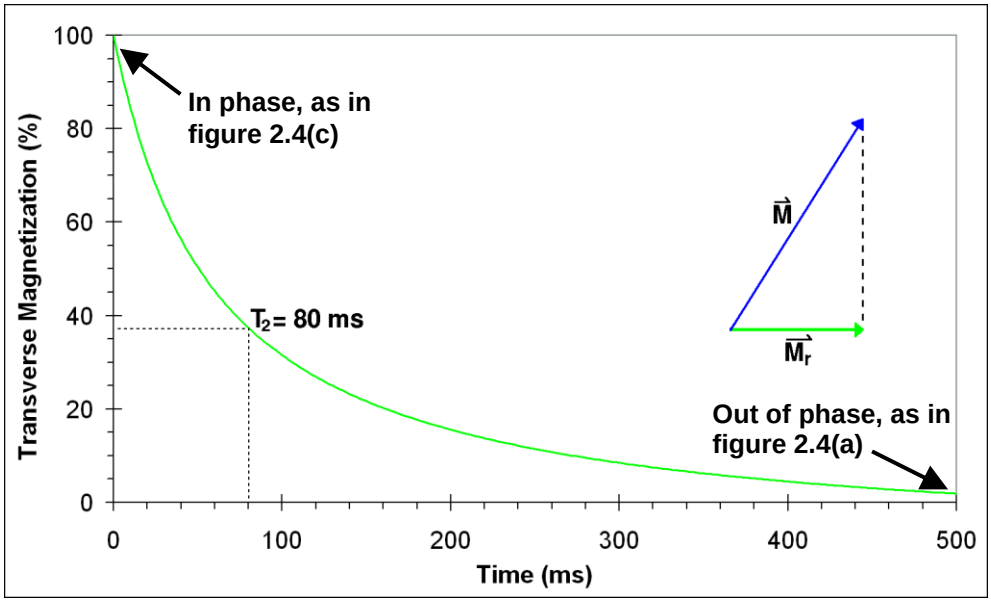

(b) Transverse Relaxation

Figure 2.5: Spin relaxation after an RF pulse broken down into (a) longitudinal and (b) transverse components for a hypothetical block of tissue with a T_1 of 325 ms and a T_2 of 80 ms.

time. In general, the decay of the transverse magnetization tends to be faster than the rate of return of the net longitudinal magnetization making T_2 shorter than T_1. In addition, the rate at which transverse magnetization is lost in inhomogeneous fields is greater than in homogeneous fields. This introduces another timing, T_2^*, which is similar to the T_2 time but includes the decay caused by field inhomogeneities. T_2^* is therefore always less than T_2.

2.1.3 Spatial Encoding

The processes of excitation and relaxation provide the basis for MR signal acquisition within a volume of interest containing non-zero spin nuclides. However, excitation at a given frequency matching the Larmor frequency of the nuclide of interest will generate signals at the same frequency. The result is a net FID (single) signal from the combined volume which bears no spatial information about the tissue type and distribution within the volume. In order to divide the MR signal into discrete locations it is necessary to introduce linear gradient magnetic fields that combine with the uniform main field in a controlled manner. The process of differentiating signal position is called spatial encoding.

There are three steps involved in spatial encoding, one for each dimension in the Cartesian coordinate system. The first step is slice selection, which excites spins within a specific slice or volume. The next two steps are phase encoding, which divides the spins in the selected slice into strips of different phases, and frequency

encoding, which divides the spins in the selected slice into perpendicular strips of different frequencies. The result of applying these three steps is to divide a volume into several slices where the combined FID signal of each slice is a combination of many phases and frequencies which can be converted into signals at particular positions using an inverse Fourier Transform.

With the first step in spatial encoding being slice selection, the goal is to measure the FID signal of all spins situated within a single slice of the volume of interest, as depicted in figure 2.6. By applying a linear gradient magnetic field, $\vec{G}(z)$, parallel to the main field the overall magnetic field becomes:

$$\vec{B} = \vec{B}_0 + \vec{G}(z) = [B_0 + G(z)]\hat{z} \tag{2.3}$$

where $\vec{G}(z) = zG_z\hat{z}$ varies along the slice selection axis, which for this example is $\hat{z}$. Replacing B_0 with $\vec{B}$ in the Larmor equation (2.1) results in an expression defining the frequency of spins as a function of slice position:

$$\omega(z) = \gamma[B_0 + G_z z] \tag{2.4}$$

Furthermore the frequency bandwidth for slice selection can be defined as:

$$\Delta\omega = \gamma G_z \Delta z \tag{2.5}$$

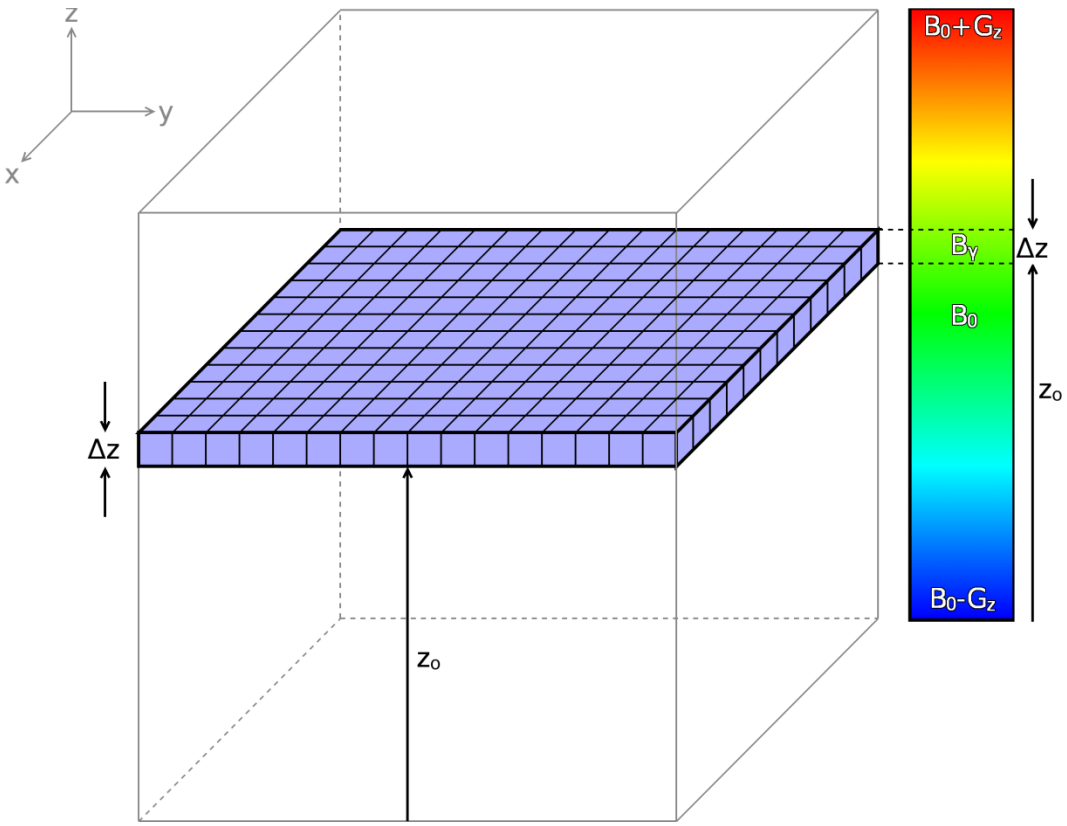

Figure 2.6: A slice with thickness Δz selected from a volume at position z_o. The linear gradient magnetic field has an intensity that ranges from $B_0 \pm G_z$ with a value of B_0 at the center of the field. The selected slice corresponds to the resonant magnetic field intensity, B_γ, that matches the Larmor frequency of the spins in the volume.

In practical terms, equations 2.4 and 2.5 mean that by applying an RF pulse at a defined frequency, $\omega(z_o)$, only the spins with frequency $\omega(z_o) \pm \Delta\omega/2$ will be excited, thereby selecting a slice centered around z_o with a thickness of Δz.

After slice selection, the next step in spatial encoding is phase encoding and is illustrated in figure 2.7(a). The purpose of phase encoding is to divide the selected slice into strips perpendicular to the slice selection axis. This division, based on phase, is illustrated in figure 2.7(a) and is achieved by applying another linear gradient field, $\vec{G}(y)$, perpendicular to the main field such that the overall magnetic field becomes:

$$\vec{B} = \vec{B}_0 + \vec{G}(y) = G(y)\hat{y} + B_0\hat{z} \tag{2.6}$$

In this equation $\vec{G}(y)$, which is equal to $yG_y\hat{y}$, varies along the phase encoding axis, which for this example is $\hat{y}$. By applying *G(y)* for a short period of time the frequency of spins along the phase encoding axis will change in proportion to the field:

$$\omega(y) = \gamma(B_0 + G_y y) \tag{2.7}$$

If, after time t_y, the gradient field is turned off, all spins within the selected slice will once again rotate at the same frequency, but their phases will be a function of position along the phase encoding direction:

$$\phi(y) = t_y \gamma G_y y \tag{2.8}$$

This procedure of applying $\vec{G}(y)$ is repeated once for each individual strip in the slice, where the applied gradient varies in steps from -G_y to +G_y to provide phase encoding.

Frequency encoding represents the last step for spatial encoding. As depicted in figure 2.7(b), encoding based on frequency divides the selected slice into strips perpendicular to the slice selection axis and phase encoding axis. Much like phase encoding, frequency encoding requires that another linear gradient field, $\vec{G}(x)$, is applied perpendicular to the main field:

$$\vec{B} = \vec{B}_0 + \vec{G}(x) = G(x)\hat{x} + B_0\hat{x} \tag{2.9}$$

In this equation $\vec{G}(x)$, which is equal to $xG_x\hat{x}$, varies along the frequency encoding axis, which for this example is $\hat{x}$. Unlike with phase encoding where the field is applied for a short time then turned off, the FID signal is measured while G_x remains on. For this reason the frequency encoding gradient field is often refered to as the readout field. The result of applying G_x during FID readout is to set the frequency of spins within the selected slice to be a function of the frequency encoding direction:

$$\omega(x) = \gamma(B_0 + G_x x) \tag{2.10}$$

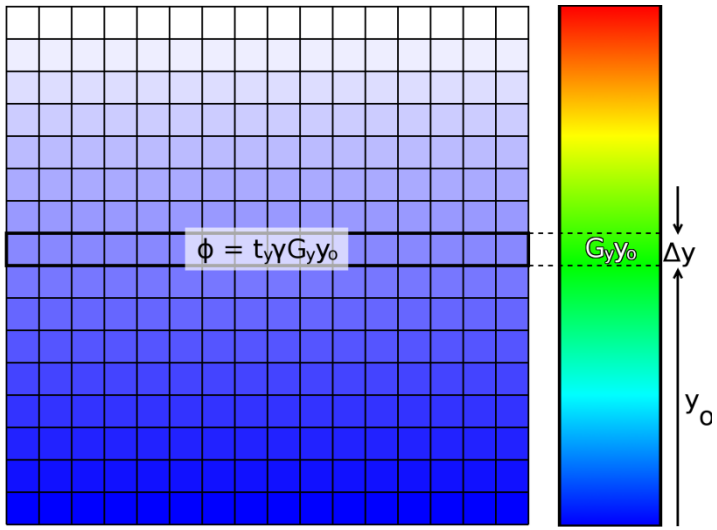

(a) Phase encoding

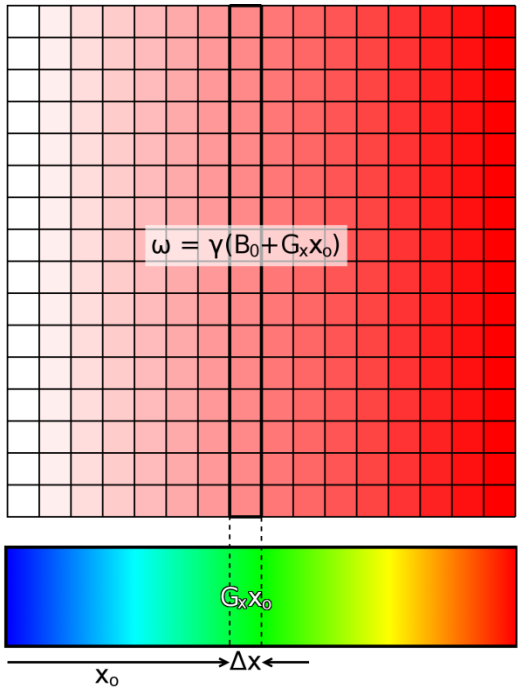

(b) Frequency encoding

Figure 2.7: For spatial encoding strips along the y-axis are encoded by phase and strips along the x-axis are encoded by frequency.

2.1.4 Image Reconstruction

Once all FID signals within the volume of interest have been encoded spatially, the recorded phase and frequency of the signals must be decoded in order to reconstruct an MR image. Mathematically, the signal comprising an MR image is recorded as discrete spatial frequencies in k-space. To produce a two dimensional (2D) or three dimensional (3D) image this discrete signal set must be converted from k-space to Euclidean r-space using an inverse Fourier Transform (FT). Since spatial encoding records FID signals in terms of spatial frequency it is useful to compare k-space and r-space during image acquisition. Let $f(\vec{r})$ be an integrable function defined in a finite 3D r-space. By applying a FT to this function we can define its analogue function in k-space:

$$F(\vec{k}) = F_{3D}[f(\vec{r})] = \int_r f(\vec{r}) e^{i2\pi(\vec{k}\cdot\vec{r})} d\vec{r} \tag{2.11}$$

where $\vec{k}$ is a 3D complex vector analogous to the $\vec{r}$ vector. To convert from k-space back to r-space a reverse FT is applied on $\vec{k}$:

$$F(\vec{r}) = \int_k e^{-i2\pi(\vec{k}\cdot\vec{r})} d\vec{k} \tag{2.12}$$

For the purposes of MR imaging, equations the integrals in equations 2.11 and 2.12 can be measured over the volume of interest and still hold true.

2.2 Imaging Sequences

2.2.1 Overview

During spatial encoding three magnetic gradients are activated in sequence to map the entire volume of interest in k-space. In addition, there are several different RF pulse sequences used to produce an image, each of which have their own advantages and disadvantages for producing images of varying contrasts between tissues. The most common pulse sequences are briefly described in the next few sections.

2.2.2 Spin Echo

One of the simplest and most common imaging sequence is spin-echo, the timing for which is illustrated in figure 2.8. As shown, each RF pulse is applied with specific timing and amplitude such that the signal from a single strip (row) of a single slice is recorded. The timing and application of the RF pulses for a spin echo sequence can be described in five steps. The corresponding position in k-space for each of the five steps of the sequence is displayed in figure 2.9.

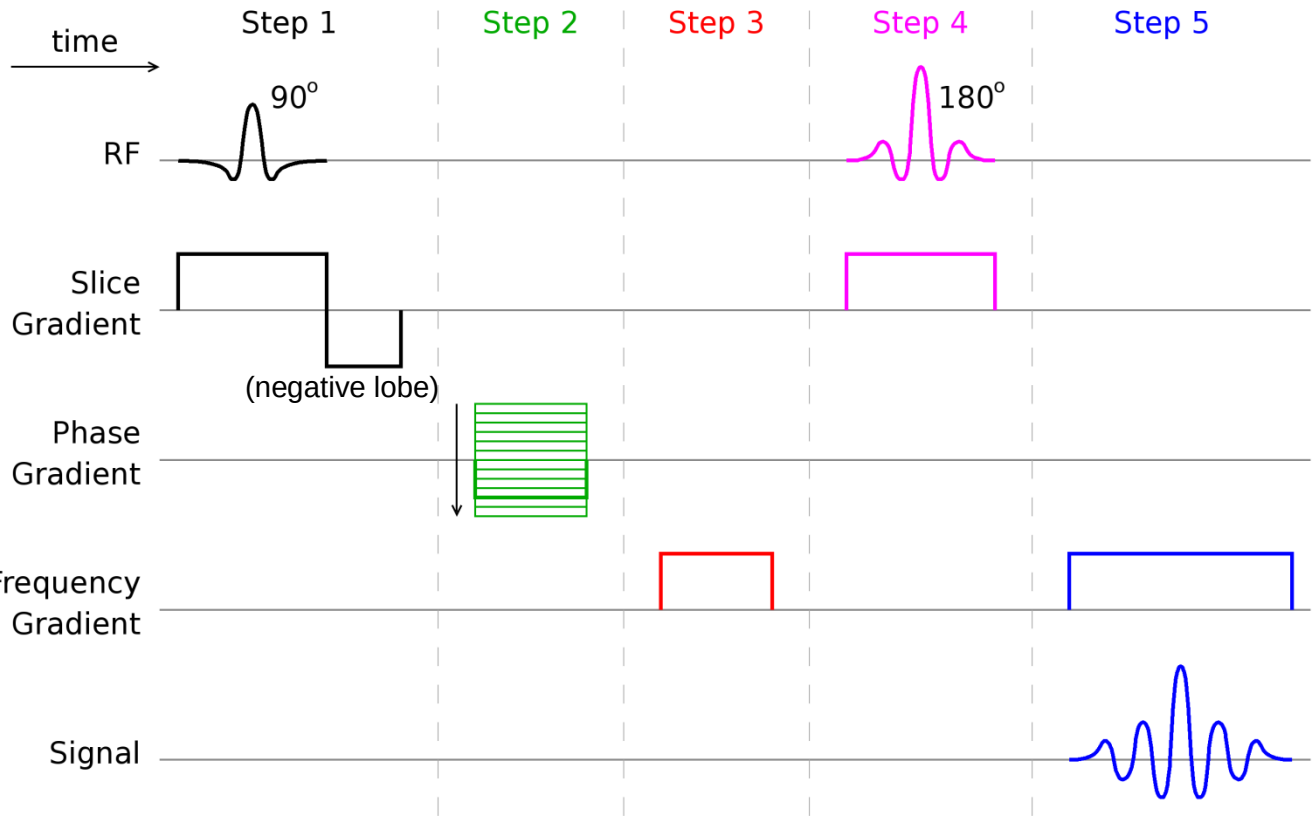

Figure 2.8: The gradient timing diagram of the spin-echo sequence. The signal line shows a single strip of a single slice being recorded in step 5. This sequence is repeated for every strip in a slice, where each of the paths in the phase gradient line corresponds to a different strip. 90° and 180° pulses are applied with specific timing to produce a signal for one row of k-space. The pulses are applied in relation to the slice selection, phase and frequency encoded gradients.

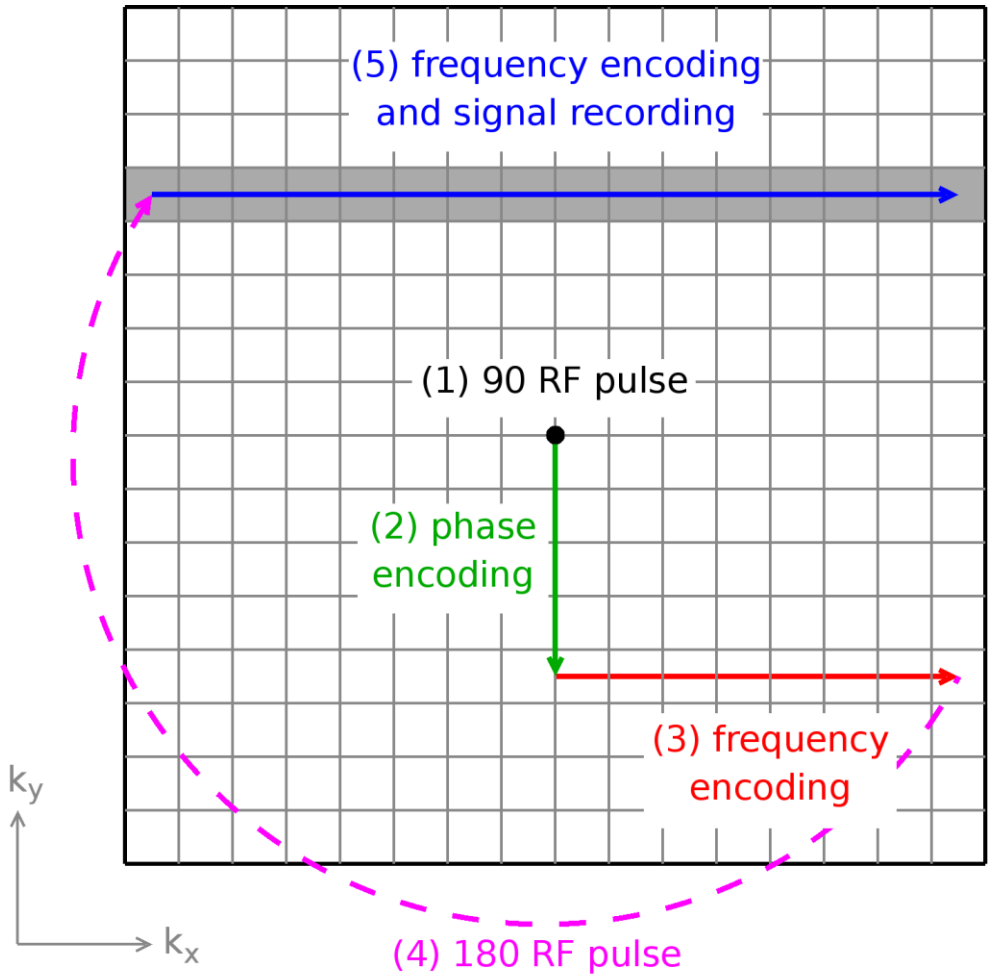

Figure 2.9: The position in k-space broken down into the 5 steps of a spin-echo sequence. This sequence is repeated once for every row until each row in the entire slice has been recorded.

The spin echo sequence is initiated with the application of a slice selection gradient and a 90° RF pulse. When slice selection occurs the slice gradient causes a linear phase-shift over the slice width. To counter this effect, a short reverse gradient (labeled in figure 2.8 as a negative lobe) is applied in the slice gradient canceling out the undesired phase-shift. Once the slice has been selected, step two is the application of a pulse from the phase gradient. The amplitude and length of this pulse will translate the system in k-space along the y-axis. Translation in the $\hat{k}_y$ direction is proportional to the amplitude and duration of the pulse. The bold green line on the phase gradient pulse of figure 2.8 demonstrates one repetition of the sequence, corresponding to the $\hat{k}_y$ translation shown in figure 2.9.

Step three is defined by a pulse from the frequency gradient. Much like a phase gradient, a frequency gradient pulse translates the system through k-space proportional to the amplitude and duration of the pulse, but in the $\hat{k}_x$ direction. The purpose of this third step is to translate the system to the end of the current row. It is important to note that although steps 2 and 3 were described separately, in practice they occur simultaneously. The fourth step is defined by another application of the slice selection gradient but this time with a 180° RF pulse. This 180° flip is the key feature in the spin-echo sequence which causes an echo signal from which the sequence gets its name. In terms of k-space, this pulse flips the position of the system to the conjugate location with respect to the center of the k-

space grid. This is denoted in figure 2.9 as a dotted line. Finally, the last step in the sequence includes a frequency gradient pulse twice as long as in the third step. This pulse translates the system across the selected row, during which the signal is recorded. The whole process is then repeated for the same selected slice, but with the next phase gradient amplitude such that the next row is recorded.

The execution of the spin echo sequence can be controlled using two times that define the sequence. These times are the echo time (TE) and repetition time (TR). TE is defined as the time between the beginning of a pulse and the signal reading (step one to step five). TR is defined as the time between successive signal readings (step five to step five of the next repetition). Therefore, the total time necessary to record an entire slice is the product of TR and total number of rows (phase encoding steps) per slice.

Once each position in k-space has been filled, the image can be reconstructed into Euclidean r-space. This reconstruction involves the application of the inverse FT, described by equation 2.12, which is used to convert the recorded signal from k-space to r-space. For the described spin-echo sequence the volume of interest is divided into 2D slices. Therefore, a 2D inverse FT of the signal over the imaging frequency space provides image intensity as a function of x and y:

$$I(x,y) = \int_{k_y\,\min}^{k_y\,\max} \int_{k_x\,\min}^{k_x\,\max} S(k_x,k_y) e^{-i2\pi(k_x x + k_y y)} dk_x dk_y \qquad (2.13)$$

where $S(k_x, k_y)$ is the recorded signal in k-space and $I(x,y)$ is the gray scale image.

2.2.3 Gradient Echo

The gradient echo (GE) pulse sequence, sometime refered to as gradient recalled echo, field echo or fast field echo, depending on the MRI manufacturer, is also a common MR sequence. It differs from the SE pulse sequence in two major ways. Unlike the SE sequence, a GE sequence begins with a shorter RF pulse that varies the flip angle from 10° to less than 90° and there is no 180° RF pulse to realign spins. The timing diagram and a corresponding k-space diagram for the GE sequence is shown in figures 2.10 and 2.11, respectively.

By allowing the initial flip angle to vary the GE sequence provides an additional parameter which may result in different signal intensities than the SE sequence. A smaller flip angle decreases the transverse magnetization which decreases the FID signal intensity. However, since this also decreases the amount of time necessary for the longitudinal magnetization to return to equilibrium, the net result is a decrease in the overall scanning time. In general, varying the flip angle can increase different tissue contrasts as compared to those found in SE sequences but will also increase image noise.

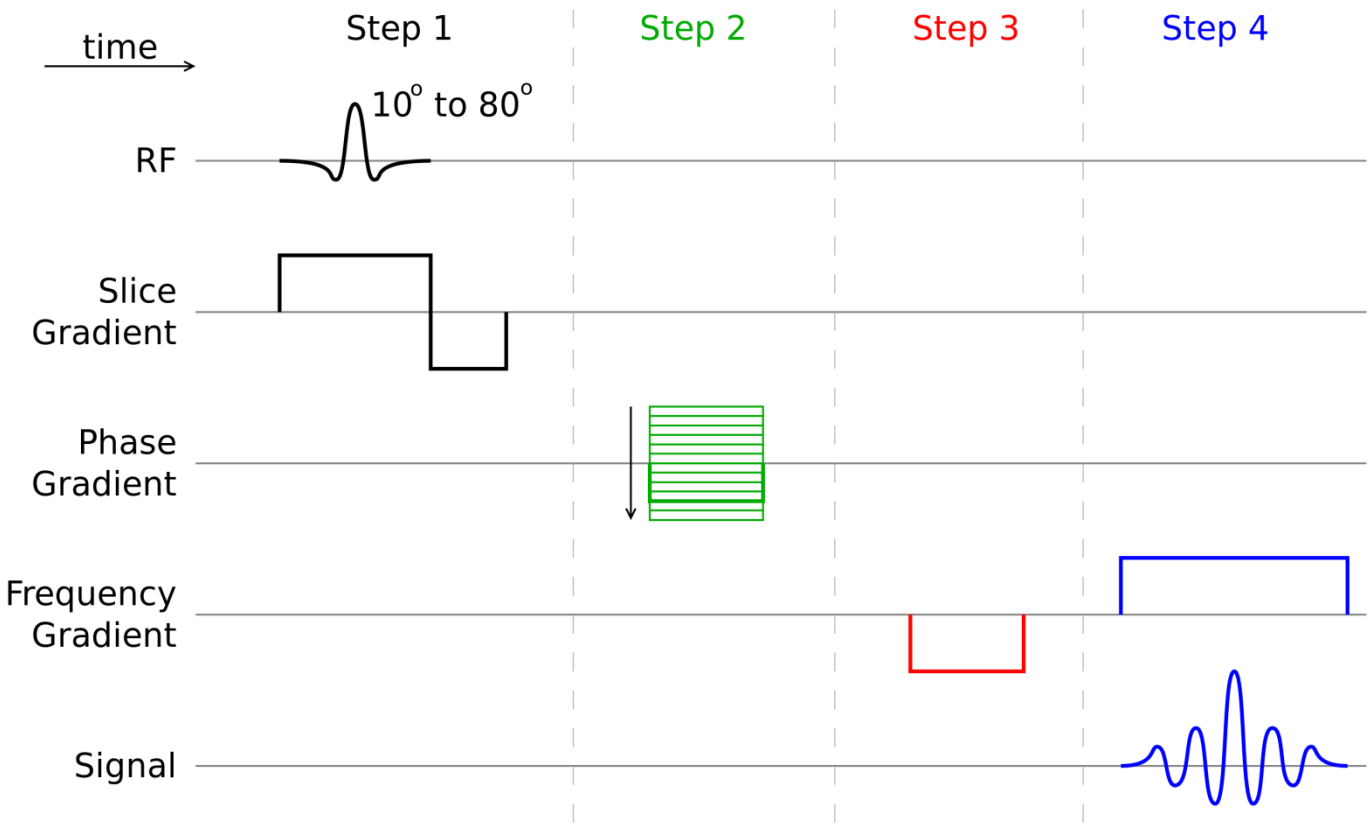

Figure 2.10: The gradient timing diagram showing the steps of a gradient-echo sequence. Note the differences between this gradient timing and the spin-echo sequence (figure 2.8): the initial pulse ranging from 10° to less than 90°, the frequency gradient pulse being negative instead of positive and the absence of a 180° RF re-aligning pulse.

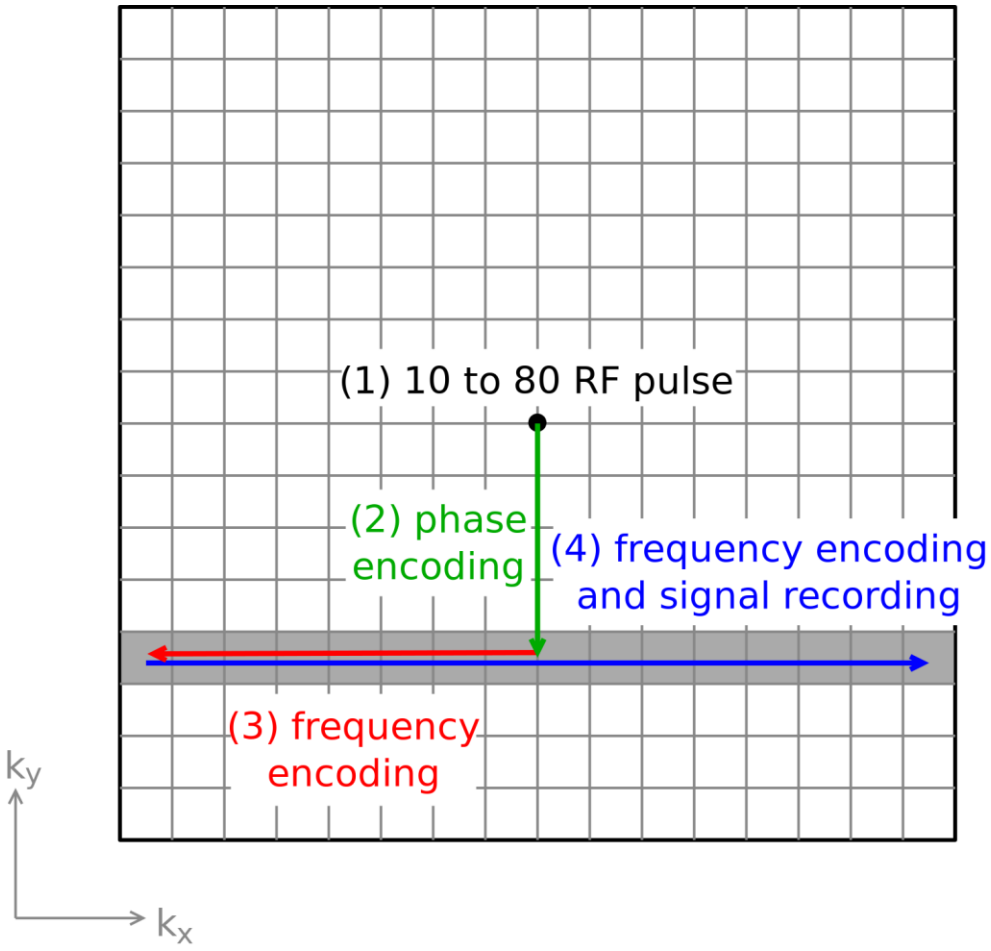

Figure 2.11: The order by which the 4 steps comprising a GE sequence fills k-space. Each execution of the sequence fills one row and so the sequence is repeated until all rows are filled. Note that unlike in figure 2.9 there is no 180° RF re-aligning pulse.

2.2.4 Other Sequences

There are a number of other common pulse sequences used for RA imaging. These sequences include Fast Spin Echo (FSE), Spoiled Gradient Echo (SGE), Inversion Recovery (IR) and Short TI Inversion Recovery (STIR). In essence, all of these sequences is a variation of the standard SE and GE sequences designed to accentuate tissue contrast while shortening imaging time. For example, FSE is a variation of the SE sequence. Its purpose is to reduce the overall scanning time by applying consecutive phase gradient, 180° RF and frequency gradient pulses (steps 2, 4 and 5, respectively, of figures 2.8 and 2.9) after each slice selection gradient and a 90° RF pulse. These consecutive pulses are sometimes refered to as as the echo train. The effect of the echo train is to multiply the number of strips of k-space which are read out in the same TR time as the SE sequence, dividing the overall scan time by the number of echos in the echo train. The SGE sequence is a variation of the GE sequence but with an additional pulse in the slice selection axis after the signal readout. This additional pulse is used to eliminate residual transverse magnetization from the previous signal readout. The IR sequence is derived from the SE sequence. It begins by inverting longitudinal magnetization by adding a 180° RF pulse before the standard 90° pulse. This makes the resulting signal strongly dependent on T1 times. The time between the 180° inversion pulse and the 90° pulse is called the inversion time (TI). The STIR

sequence is a variant of the IR sequence which uses a short TI time to suppress the signal of fat.

2.3 Determinants of Image Characteristics

The appearance of an MR image can vary greatly depending on the configuration of the scanners and pulse sequences used to form an image. The strength of the main field, bore size and whether the scanner has an open or closed magnet are all dependent on the scanner configuration and cannot be changed during imaging. However, sequence type, repetition time, echo time, inversion time, flip angle, slice thickness, slice gap, field of view, acquisition matrix and resolution are all modifiable factors that can be selected to obtain images that optimally show features of interest.

The signal to noise ratio (SNR) is an indication of image quality. For MR images, in general, changes in SNR are determined by the size of a voxel, the number of measurements and the bandwidth. Mathematically this is described by the following proportionality:

$$SNR \propto \Delta x \Delta y \Delta z \sqrt{\frac{NEX}{BW}} \tag{2.14}$$

where Δx, Δy and Δz are the dimensions of a voxel, NEX is the number of excitations and BW is the receiver bandwidth.

Changes to MR image quality and characterstics can be achieved with the use of contrast agents. In addition, image quality can also be negatively impacted by the appearance of various image artifacts. The use of contrast and the most common artifacts are briefly described in the next two sections.

2.3.1 Contrast Agents

A common method to modify the characteristics of an MR image to improve visualization of features of interest is the use of MR contrast agents. Contrast agents are artificial substances which are administered to a patient during an MR scan in order to alter some or all of the T1, T2 and T2* times of nearby hydrogen nuclei, thereby increasing the signal difference between two or more tissues. There are four classes of contrast agents based on their magnetic behaviour: diamagnetic, paramagnetic, super-paramagnetic and ferromagnetic. One of the most commonly used contrast agents is gadolinium, a paramagnetic.

2.3.2 Image Artifacts

There are several image artifacts that can adversely affect image quality. However, depending on the cause, image artifacts may be eliminated or minimized by various techniques. Those artifacts which may affect the appearance of bone erosions in the metacarpophalangeal joints are described in the next few paragraphs.

Aliasing artifacts are caused by scanning objects which are larger than the field of view (FOV). Features outside of the FOV are still encoded in k-space, so when a reverse Fourier transform is used to transform k-space into r-space these features appear to overlap features inside the FOV. This causes features which fall outside the FOV to appear on the opposite side of the image. This artifact is not usually a problem when imaging a hand so long as the hand is not near any other anatomy (i.e.: up against the body).

Motion artifacts are caused by subject movement during scanning. This artifact appears in an image as either blurred features or ghosting (duplicated features overlapping one another). Blurring is caused by random motion such as a patient voluntarily or involuntarily moving. Ghosting is caused by periodic motion such as respiratory or pulmonary movement. When imaging a hand, artifacts caused by random patient motion can be minimized by restricting the hand with foam padding or applying a brace. Ghosting is not a concern since lung and heart movement should not affect the extremities if properly positioned before scanning.

Chemical shift artifacts are inherent to the tissues being imaged and are caused by the difference in resonance frequency of various MR signal-exhibiting tissues, most commonly water and fat. The result of this chemical shift is a displacement of those tissues which have a lower resonant frequency (such as fat) in the

frequency encoding direction. This displacement usually appears as a black (low signal) band near the boundary between bone, fat and muscle. It is important to note that the chemical shift effect is directly proportional to the magnetic field strength of the scanner and is not usually of great concern for lower field scanners (≤1 Tesla).

Finally, partial volume averaging is considered an artifact which is caused when the signal from two or more materials contribute to the same voxel. The resulting voxel will appear to have a signal which is the mean of all signals included in its spatial volume. Effects of partial volume averaging are most visible at the boundary between tissues. Quite simply, the boundaries between distinct tissues appear blurred and difficult to differentiate and segment. The effects of partial volume averaging can be minimized by reducing slice thickness and increasing the image matrix size to improve spatial resolution.

2.4 Literature review of sequences used for RA imaging

A literature search was done using Ovid Medline®, including references published between 1998 and the present. Search criteria included “Rheumatoid Arthritis”, “MRI” and “hand or wrist”, with review articles and duplicate references using the same images omitted. A total of 40 relevant articles were found, listing 17 different scanners and a total of 184 imaging configurations. 32 of 40 of the studies used a contrast agent in at least one scan, 12 studies used low-field 0.2 or

0.23T scanners, 1 used a 0.6T scanner, 5 used a 1.0T scanner, 24 used a 1.5T scanner and 3 did not report the main field strength or scanner type that was used. The imaging parameters for all studies examined are listed in table 2.1 and 2.2 for all scanners with a main field strength of less than 1.5T and equal to 1.5T, respectively.

Out of 40 articles, 14 used Outcome Measures In Rheumatology Clinical Trials (OMERACT) guidelines for MR image acquisition. Of the remaining 26 articles, 10 used images coinciding with the OMERACT guidelines but did not specify them as such, 6 did not specify reasoning behind MR image acquisition parameters, 6 did not study bone erosions and 4 used sequences other than SE, GE or Short TI Inversion Recovery (TRIM). Ostergaard et al. (2003b) outline a core set of basic MR sequences recommended by the OMERACT group to be used for RAMRIS. These include T1-weighted images before and after gadolinium contrast, and a T2-weighted fat saturated image or TRIM image in its place. Additionally, gadolinium contrast agent is considered to be unnecessary if the purpose of the MR scan is to examine destructive changes to bone only. Nevertheless, for the accurate volumetric measurement of bone erosions, it is important to consider identification of bone edema. Bone edema often surrounds erosions and can cause erosion size to easily be misjudged. In a study comparing

Table 2.1: A survey of MR scanners and configurations used in RA studies of the hand and/or wrist where the main magnetic field strength is less than 1.5 Tesla. Bo is the main magnetic field strength in Tesla, FS is whether fat saturation was used, CA is whether a contrast agent was used, Seq. is the sequence type, TR is repetition time in ms, TE is echo time in ms, slice and gap are slice thickness and gap between slices in mm and Res. is image resolution in mm x mm. Configurations which were not reported are marked as NR.

Paper	Unit	Bo (T)	FS	CA	Seq.	Weight	TR/TE	Slice/Gap	Res.
Backhaus (1999)	Siemens Magnetom	0.2	-	-,+	SGE	T1	34/12	1.0/0.0	NR
Cimmino (2003)	Esaote Artoscan	0.2	-	-,+	SE		100/16	5.0/0.0	0.9 × 1.2
Dohn (2006)	Philips Panorama	0.6	-	-	GE	T1	20/8	0.4/0.0	0.4 × 0.4
Ejbjerg (2005)	Siemens Impact	1.0	-	-,+	SE	T1	600/15	3.0/0.0	0.6 × 0.6
			-	-	STIR		4500/30	3.0/0.0	0.6 × 0.6
			+	-	SE	T2	4500/96	3.0/0.0	0.6 × 0.6
	Esaote Artoscan	0.2	-	-,+	SE	T1	550/18	3.0/0.0	0.8 × 0.8
			-	-	GE	T1	30/12	1.0/0.0	0.7 × 0.9
			-	-	STIR		1100/24	3.0/0.3	1.0 × 1.3
Eshed (2006)	Esaote C-scan	0.2	-	-	STIR		700/16	3.0/0.3	0.7 × 0.9
			-	-	SE	T1	520/26	3.5/0.3	0.6 × 0.4
			-	-,+	GE	T1	35/16	0.9/0.0	0.8 × 0.6
Goupille (2001)	Siemens Magnetom	1.0	-	-,+	SE	T1	500/20	4.0/0.0	0.9 × 1.0
			-	-	GE	T2*	420/18	6.0/0.0	0.7 × 0.8

Paper	Unit	Bo (T)	FS	CA	Seq.	Weight	TR/TE	Slice/Gap	Res.
Hermann (2006)	NR	NR	-	-	SE	T1	401/21	NR	0.3 × 0.3
			+	-	SE	T1	622/21	NR	0.3 × 0.3
			+	-	SE	T1	726/21	NR	0.3 × 0.3
			-	-	STIR		5000/68	NR	0.7 × 0.6
			-	-	GE	T1	902/372	NR	0.4 × 0.4
Klarlund (1999)	Siemens Impact	1.0	-	-,+	SE	T1	600/15	3.0/0.0	0.5 × 0.5
Hoving (2004)	NR	NR	+	-	GE	T1	60/10	1.0/0.0	0.4 × 0.4
			+	-	FSE		4000/35	2.0/0.0	0.2 × 0.7
			-	+	SGE		NR	0.7/0.0	NR
Lindegaard (2001)	Esaote Artoscan	0.2	-	-	STIR	T1	500/18	3.0/0.3	0.8 × 1.3
			-	-,+	SE	T1	500/18	3.0/0.3	0.8 × 1.0
Ostergaard (2005)	Philips Panorama	0.2	-	-	GE	T1	NR	1.5/0.0	0.4 × 0.3
			-	-	STIR	T2	NR	3.5/0.0	0.8 × 0.7
			-	+	FSE	T1	NR	1.5/0.0	0.4 × 0.3
Ostergaard (2003)	NR	NR	-	-,+	SE	T1	480/15	3.0/0.0	NR
			-	-,+	SE	T1	600/17	3.0/0.0	NR
Ostergaard (2001)	Siemens Impact	1.0	-	-,+	SE	T1	600/15	3.0/0.0	0.7 × 0.5
Palosaari (2004)	Philips	0.2	-	-,+	GE		30/10	2.0/0.0	1.3 × 0.6
			-	-	STIR		1800/25	3.0/0.0	0.8 × 0.7
			-	-	FSE	T2	4000/100	3.0/0.5	0.8 × 0.6

Paper	Unit	Bo (T)	FS	CA	Seq.	Weight	TR/TE	Slice/Gap	Res.
Savnik (2001)	Esaote Artoscan	0.2	-	-	STIR		1450/28	2.5/0.3	0.6 × 0.8
			-	-,+	GE	T1	30/12	1.0/0.0	0.6 × 0.8
			-	-	STIR		2000/90	2.5/0.2	0.9 × 0.9
			-	-,+	GE	T1	25/4.6	1.0/0.0	0.9 × 0.9
Scheel (2006)	Esaote Artoscan	0.2	-	-	STIR		700/16	3.0/0.3	1.1 × 0.5
			-	-	SE	T1	520/26	3.5/0.3	0.6 × 0.6
			-	+	GE	T1	35/16	0.8/0.0	0.8 × 0.8
Taouli (2004)	Esaote Artoscan	0.2	-	-	GE	T1	30/12	3.0/0.0	0.8 × 0.8
			-	-	STIR		1000/16	3.5/0.0	0.9 × 0.9
Valeri (2001)	Siemens Magnetom	1.0	-	-	SE	T1	500/17	3.0/0.1	NR
			-	-	GE	T2*	400/18	3.0/0.1	NR
Yoshioka (2006)	Custom	0.2	-	-	SE	T1	160/16	4.0/0.0	0.8 × 1.6
			-	-	STIR		1400/50	NR	0.8 × 1.6

Table 2.2: A survey of MR scanners and configurations used in RA studies of the hand and/or wrist where the main magnetic field strength is equal to 1.5 Tesla. FS is whether fat saturation was used, CA is whether a contrast agent was used, Seq. is the sequence type, TR is repetition time in ms, TE is echo time in ms, slice and gap are slice thickness and gap between slices in mm and Res. is image resolution in mm x mm. Configurations which were not reported are marked as NR.

Paper	Unit	FS	CA	Seq.	Weight	TR/TE	Slice/Gap	Res.
Bird (2005)	GE Signa	-	-	NR	T1	480/18	3.0/0.3	0.5 × 0.5
	Siemens Magnetom	-	-	NR	T1	500/20	3.0/0.0	0.5 × 0.5
Boutry (2005)	Siemens Vision	-	-	STIR	T2	5216/60	4.0/0.0	0.8 × 0.4
		-	-,+	SE	T1	570/20	4.0/0.0	0.4 × 0.4
		-	+	SGE		36/9	1.5/0.0	0.7 × 0.4
Carano (2004)	GE Signa	-	-	SE	T1	600/9	3.0/0.0	0.2 × 0.6
		+	-	GE	T2	29.4/6.3	1.5/0.0	0.2 × 0.6
Conaghan (2003)	ACS Gyroscan	-,+	-,+	SE	T1	485/20	1.5/0.2	0.4 × 0.2
		+	-	FSE	T2	2000/100	2.0/0.2	0.4 × 0.4
Huang (2000)	GE Signa	+	-,+	SGE		150/9.1	3.0/2.0	0.5 × 0.5
Kirkhus (2006)	Siemens Magnetom	-	-	GE		25.4/9	1.5/0.0	0.8 × 0.6
		-	+	SGE	T1	8.5/4	5.0/0.0	1.3 × 1.3
McGonagle (1999)	Philips Gyroscan	-	-,+	SE	T1	500/20	2.0/0.2	0.6 × 0.6
		+	-	FSE	T2	2000/100	3.0/0.3	0.4 × 0.4

Paper	Unit	FS	CA	Seq.	Weight	TR/TE	Slice/Gap	Res.
Ostergaard (2001)	Philips Gyroscan	-	-,+	SE	T1	485/20	1.5/0.1	0.4 × 0.4
		+	-	FSE	T2	2000/100	2.0/0.2	0.5 × 0.4
		+	+	SPIR	T1	450/20	1.5/0.1	0.5 × 0.4
	GE Signa	-	-	SE	T1	600/9	3.0/0.0	0.6 × 0.2
		+	-	GE	T2*	29.4/6.3	1.5/0.0	0.6 × 0.2
Ostergaard (1999)	Siemens Magnetom	-	-,+	SE	T1	480/15	3.0/0.0	0.4 × 0.6
Ostendorf (2001)	Siemens Magnetom	-	-,+	FSE	T2	3500/100	3.0/0.0	0.3 × 0.8
		-	-,+	SE	T1	500/15	3.0/0.0	0.3 × 0.9
		-	+	SE	T1	600/15	3.0/0.0	0.3 × 1.1
		+	-	STIR		3975/20	3.0/0.0	0.3 × 1.0
Schirmer (2007)	Siemens Sonota	-	-	STIR		5000/65	3.0/0.3	0.7 × 0.7
		-	-,+	SE	T1	500/21	3.0/0.3	0.4 × 0.4
		-	-,+	GE	T1	8.8/3.5	1.0/0.0	0.5 × 0.5
Schoellnast (2006)	Siemens Magnetom	-	-	SE	T1	440/20	3.0/0.0	0.8 × 0.4
		-	-	SGE	T1	473/11	3.0/0.0	0.5 × 0.4
		+	+	SE	T1	540/23	3.0/0.0	0.7 × 0.4
		-	-	IR	T2	3000/127	4.0/0.0	0.6 × 0.4
Solau-Gervais (2006)	Siemens Vision	+	+	SE	T1	36/9	1.5/0.0	0.7 × 0.4
		-	+	SGE		36/9	1.5/0.0	0.7 × 0.4
Sugimoto (1998)	Toshiba MRT 200	-,+	+	NR	T1	380/20	4.0/1.0	0.8 × 0.9
Taouli (2004)	GE Signa	-	-	SE	T1	600/9	3.0/0.0	0.2 × 0.6
		+	-	GE	T2*	29.4/6.3	1.5/0.0	0.2 × 0.6

Paper	Unit	FS	CA	Seq.	Weight	TR/TE	Slice/Gap	Res.
Tehranzadeh (2004)	Picker Eclipse	-,+	-	SE	T1	400/10	3.0/0.5	0.5 × 0.4
		-,+	-,+	SE	T2	2500/80	3.0/0.5	0.5 × 0.4
Terslev (2003)	Philips Gyroscan	-	-,+	GE	T1	25/4.6	1.0/0.0	0.9 × 0.9
Yao (2006)	GE Signa	-	-,+	SE	T1	600/11	1.0/0.0	0.4 × 0.4
		+	-	FSE	T2	2500/68	3.0/1.0	0.4 × 0.4
Zikou (2006)	Philips Gyroscan	-	-	FSE	T2	4000/120	3.0/0.3	0.9 × 0.9
		+	-,+	SE	T1	590/15	3.0/0.3	0.9 × 0.9

Table 2.3: Mean, minimum and maximum TR and TE timings for all SE, FSE and GE sequences included in the literature review. N is the number of papers the sequence was used in.

Sequence	N	TR/TE Mean	TR/TE Min	TR/TE Max
T1 SE/FSE	35	536/17	160/9	855/26
T2 SE/FSE	9	3000/96	2000/68	4500/120
T1 GE	11	110/44	9/4	902/372
T2 GE	1	29/6	N/A	N/A

the effectiveness of T2-weighted fat saturated and T1-weighted contrast enhanced images, Yao et al. (2006) concluded the T2-weighted sequence to be indispensable in the absence of contrast enhancement. Therefore, in order to make accurate volumetric measurements of bone erosions non-invasively a combination of T1-weighted and T2-weighted, fat saturated images should be employed.

In general, bone features are best imaged with short TE and long TR times. This is reflected by the various TR and TE times reported in the RA literature. A list of mean, minimum and maximum reported timings is given in table 2.3 for all SE, FSE and GE sequences.

2.5 Choice of imaging parameters

Bone erosions in the metacarpophalangeal joins were imaged using a coronal 3D SGE sequence on a 1 Tesla peripheral scanner using a 100 mm diameter cylindrical transmit and receive coil (OrthOne, ONI Medical Systems, Inc., Wilmington, Massachusetts). Imaging parameters were chosen in order to acquire 3D scans with minimal slice thickness which maximized the contrast between bone erosion and surrounding tissues and with the smallest slice thickness. The imaging parameters are listed in table 2.4.

Table 2.4: Imaging parameters of the 3D SGE sequence chosen to image bone erosions in metacarpophalangeal joints. These parameters were chosen in order to maximize the contrast between bone erosion and surrounding tissues and with the smallest slice thickness.

Repetition Time (TR)	60.0 ms
Echo Time (TE)	7.6 ms (minimum)
Slice Thickness	1.0 mm
Imaging Matrix	256 × 512 re-sampled to 512 × 512
Field of View	140 × 140 mm
Voxel Dimensions	0.273 × 0.273 × 1.0 mm
Number of Averages	1
Imaging Coil	100 mm cylindrical
Flip Angle	60.0°
Bandwidth	50 kHz

2.6 Sample MR Images

Figure 2.12 displays MR images of two subjects with RA. Fat, including bone marrow, displays as the brightest signal (white or bright gray), muscle displays as the mid-level signals (dark gray) and bone, tendons and background (no tissue) appear black since they do not produce any signal. Sub-figure (a) shows the earlier stages of the disease which includes several small erosions denoted by small arrows. As the disease progresses without treatment the erosions may continue to grow until most or the entire joint has been damaged. Sub-figure (b) shows an example of the potential later stages of the disorder. The large arrows point to inflammed MCP joints which have been overwhelmed by erosions. At this late stage of RA the gross deformity caused by joint damage is irreversible. Both images were acquired using the protocol and imaging parameters listed in the previous section.

Changes in erosion size and volume are one of the most sensitive indicators of RA progression. This progression is best imaged with MRI. Determination of erosion size and volume requires the delineation of the boundary between the erosion and bone or soft tissue on each slice of the MR image containing an erosion. Automated delineation of this bondary is the purpose of this thesis. The challenges and approach adopted for the automation is the focus of the remaining chapters.

(a) Early RA

(b) Late RA

Figure 2.12: Sample coronal MR images of two subjects with RA. (a) Small arrows point to small erosions in the 3rd and 4th MCP joins, consistent with early RA. (b) Large arrows point to erosions which have completely collapsed several of the MCP joints where gross deformity has occurred as consistent with the late stages of RA.

Chapter 3

Image Segmentation

3.1 Overview

In order to make quantitative measurements from any medical image it is first necessary to distinguish Features of Interest (FOIs) from a variety of tissues. Te process of distinguishing FOIs is known as image segmentation and can be performed manually by tracing feature outlines or by computer automation or by some combination of the two. This section describes several well known segmentation algorithms along with their advantages and disadvantages when applied specifically to defining erosions in MR images. All segmentation techniques described in this chapter are listed in table 3.1 along with their mode of automation, number of dimensions and algorithm paradigm.

3.2 Manual Segmentation

Manual segmentation involves marking each pixel or voxel in the image as either belonging to or not belonging to a FOI. Often this is done by using mouse clicks to trace the outline of a FOI one slice at a time. Depending on the signal to noise ratio (SNR) and resolution of the image, a strictly manual approach typically has high accuracy, but is tedious and time consuming. When used to segment erosions, accurate delineation of true FOI boundaries requires a trained and highly skilled reader, such as a musculoskeletal radiologist.

Table 3.1: A list of segmentation techniques which are applicable to segmenting bone erosions. A number of features of each technique are listed including the degree of automation, the number of dimensions the algorithm is limited to and the paradigm describing whether the algorithm is region-based or boundary-based segmentation. Semi-automated segmentation uses a combination of manual and automated segmentation.

	Automation	**Dimensions**	**Algorithm Paradigm**
Manual Tracing	manual	2D	N/A
Naïve Thresholding	full	3D	region-based
Least-Cost Graphs	semi	2D	boundary-based
Watershed	full	3D	boundary-based
Region Growing	full	3D	region-based
Level-Set	full	3D	boundary-based

3.3 Automated Segmentation

Automatic segmentation is performed by a computer using an algorithm which is designed to automatically identify features in an image. In general, computerized algorithms can be grouped into region-based algorithms that use similarity properties to identify distinct regions and boundary-based algorithms that use discontinuity properties to identify feature boundaries.

3.3.1 Naïve Threshold Segmentation

The most basic automated image segmentation is naïve thresholding. It works on the principal that all voxels in an image or a defined region of interest are determined to be part of a FOI their values fall between predefined lower and upper thresholds. Upper and lower thresholds are often selected based on background signal intensities of the input image. Native thresholding is a simple function of position which marks every voxel as part of the segmentation if its scalar intensity is within the threshold range. The function, $S(\vec{r})$, determines whether the voxel pointed to by the vector $\vec{r}$ belongs to the segmentation:

$$S(r) = \begin{cases} 1 & \text{if } I(\vec{r}) \in [T_l, T_u] \\ 0 & \text{if } I(\vec{r}) \notin [T_l, T_u] \end{cases} \tag{3.1}$$

where $I(\vec{r})$ is the intensity of the voxel pointed to by the vector $\vec{r}$ and T_l and T_u are the lower and upper intensity thresholds. Though naïve thresholding can be

fast and easy to implement, it often fails to solve complex segmentation problems. For example, figure 3.1 shows the result of applying naïve thresholding to an MR image of a metacarpal head containing a typical erosion surrounded by several other tissues. Clearly this thresholding approach cannot correctly distinguish between different tissues in an image if they have similar signal characteristics, even if they are spatially separated. For example, there is no way to distinguish between bone marrow and soft tissue (since their signals are both within the threshold boundaries) or bone erosion and the synovium, cartilage or the background (since their signals are outside of the threshold boundaries).

Naïve thresholding approaches will also fail if the image has non-uniform or gradient background intensities. This non-uniform background is quite common in MR images due to tissue depth relative to the position of the RF coil. This non-uniformity may cause the threshold which differentiates a FOI from surrounding tissue to vary, making it impossible to select appropriate values for T_l and T_u.

3.3.2 Least Cost Graph Algorithms

There are a number of least-cost or shortest path graph search algorithms which can be used for image segmentation. These algorithms consider every pixel in a 2D image to be a vertex in a mathematical graph. Shortest path graph search algorithms find the shortest path between an initial vertex and all other vertices in the graph, weighted by edge costs. When applied to medical images, these least

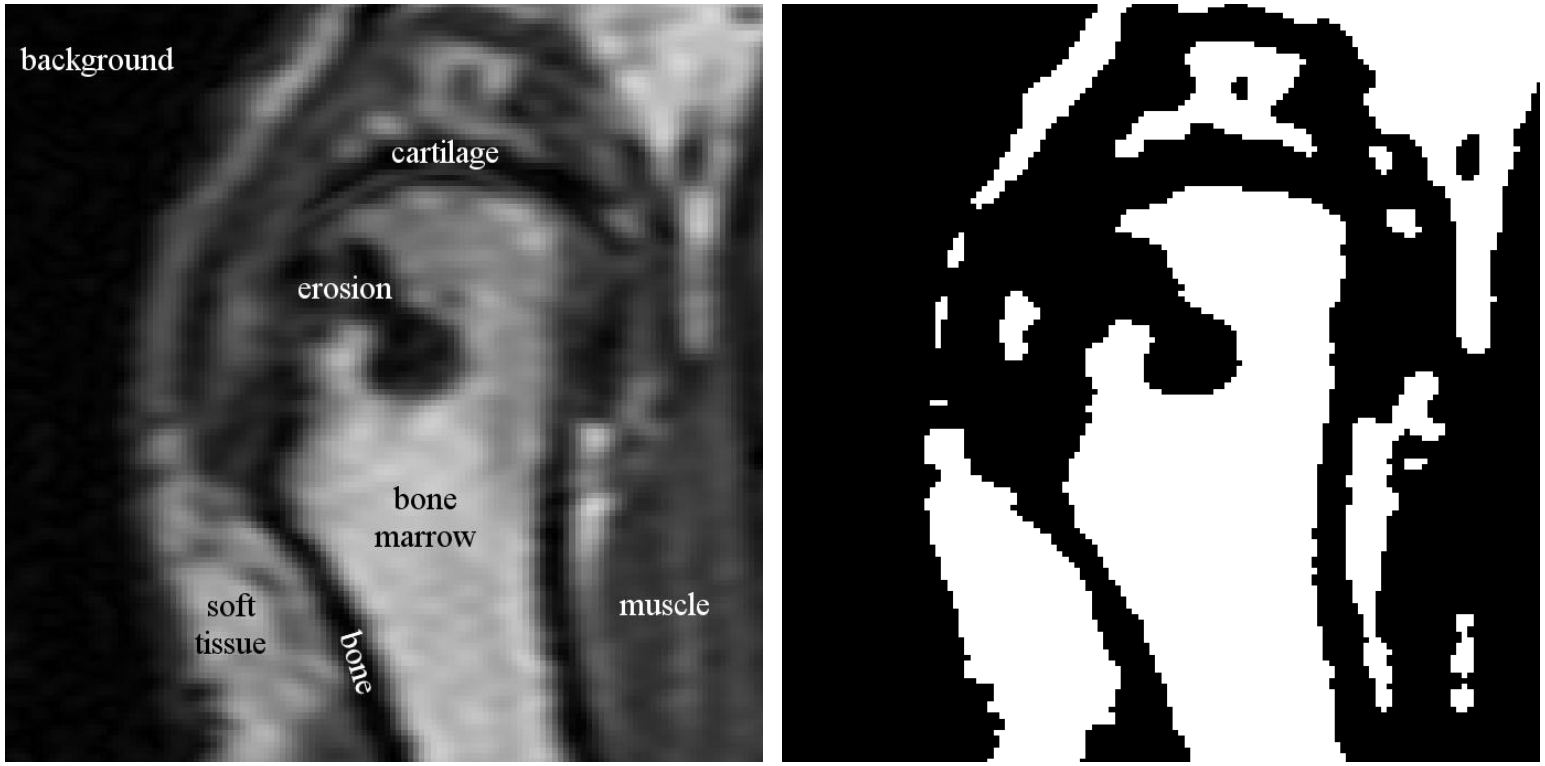

(a) Initial image (b) Naïve thresholding

Figure 3.1: An example of naïve thresholding applied to an MR image of an erosion in the 2nd metacarpal head. Note that there is no way to distinguish between bone marrow and soft tissue (since their signals are both within the threshold boundaries) or bone erosion and the synovium, cartilage or the background (since their signals are outside of the threshold boundaries).

cost graph algorithms are useful for guiding manual tracing and are therefore considered to be semi-automated. One of the most widely applied least cost algorithms is Dijkstra's algorithm (Dijkstra 1959). This algorithm has since been expanded upon by applying heuristics to decrease processing time (Hart et al 1968, Berliner 1979).

Implementation of Dijkstra's algorithm is shown in figure 3.2. Subfigure (a) shows a graph where vertices and edges represent pixels in an image and the traversal cost between vertices, respectfully. Vertex A is highlighted in green, denoting this as the initial vertex. Subfigure (b) shows the graph after the first pass through the while loop of the algorithm. In this diagram, vertex A is highlighted in blue to represent this vertex now belonging to a visited set, and its distance is set to 0 (since it is the initial vertex), as denoted by a subscript. Furthermore, A's neighbours, B, D and E are highlighted in green since they are now members of the working set, which will be processed in the next iteration of the algorithm. Subfigure (c) shows the second pass through the algorithm where vertex B is highlighted in blue as it had the lowest cost out of all vertices in the working set. Furthermore, B's neighbours which do not already belong to the visited set, C and F, have been highlighted in green as they are now members of the working set. Finally, (d) depicts the graph after the algorithm has completed and all vertices have been visited. The paths with the lowest costs are denoted by

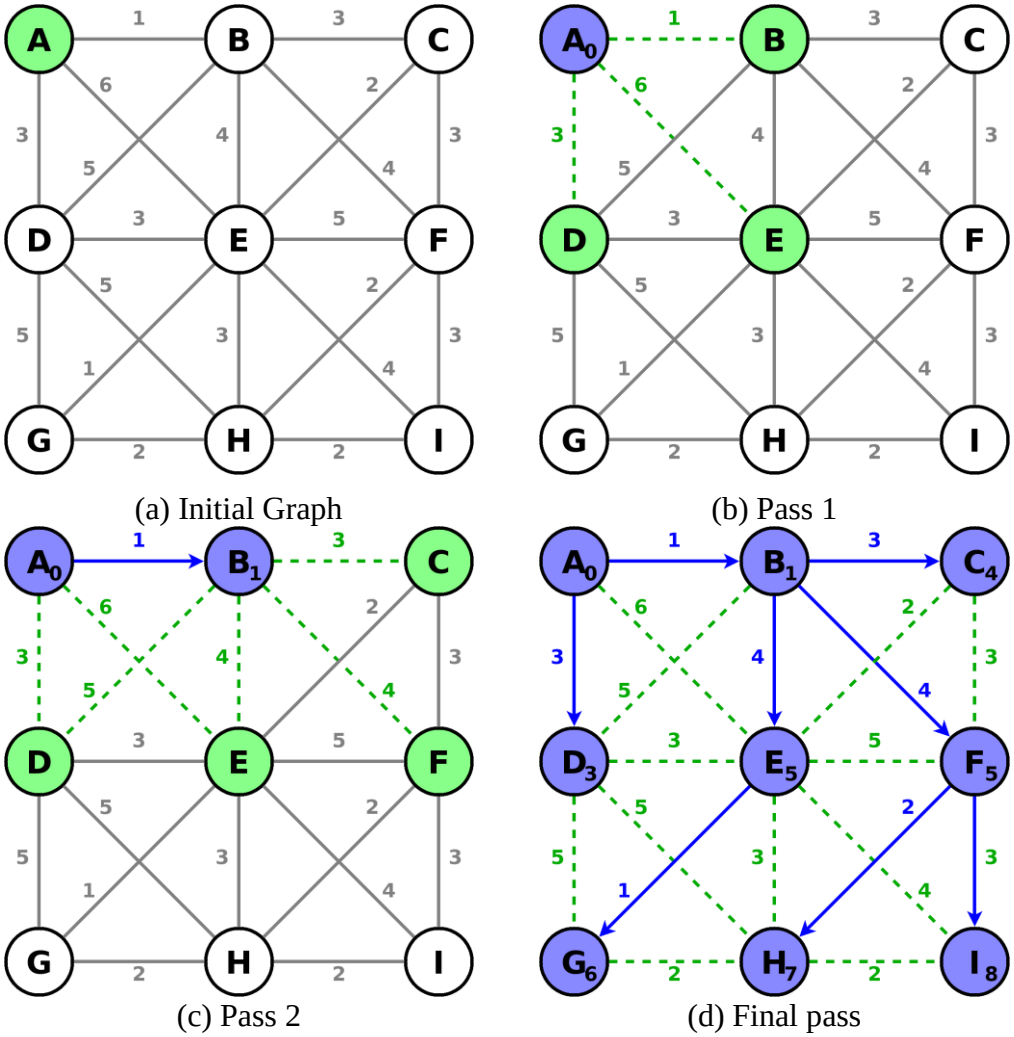

Figure 3.2: An example of Dijkstra's algorithm. It begins with an initial graph where vertices represent pixels and edges represent the traversal cost from one pixel to another. After one pass through the algorithm the cost of vertex A has been determined and added to the visited set and its neighbours, B, D and E are now members of the working set. After a second pass through the algorithm the cost of vertex B, 1, has been determined and added to the visited set and its neighbours, C and F are now members of the relaxed set. The algorithm finishes with a final pass by determining the shortest path from A to all other vertices, as denoted by the blue arrows.

blue arrows and the cost to each vertex is denoted by subscripts. See section A.1 in the appendix for sample pseudocode of Dijkstra's algorithm.

Dijkstra's algorithm can be used to semi-automate the manual tracing of features in medical images. For this purpose, pixel traversal cost (edges) is determined by features in the image:

$$cost(\vec{r}) = w_G G^{-1}(\vec{r}) + w_C C(\vec{r}) \tag{3.2}$$

where w_G and w_C are weighting constants applied to the gradient and curvature costs, respectively, and $G^{-1}(\vec{r})$ and $C(\vec{r})$ are the inverse gradient magnitude cost and curvature cost at position $\vec{r}$, respectively. The inverse gradient magnitude of the image is found in order to create a low cost near boundaries that have high gradients, and high cost elsewhere:

$$G^{-1}(\vec{r}) = 1 - \|\nabla I(\vec{r})\| \tag{3.3}$$

where the gradient magnitude, $\|\nabla I\|$, is normalized to the range [0, 1]. The curvature cost is used to smooth jagged paths and is calculated by the angle between two consecutive edges:

$$C(\vec{r}_2) = \frac{1}{2}\left[\frac{\vec{r}_2 - \vec{r}_1}{\|\vec{r}_2 - \vec{r}_1\|} \cdot \frac{\vec{r}_1 - \vec{r}_0}{\|\vec{r}_1 - \vec{r}_0\|}\right] \tag{3.4}$$

where $\vec{r}_0$, $\vec{r}_1$ and $\vec{r}_2$ are the positions of three consecutive vertices (pixels) in the path. Figure 3.3 shows an example of Dijkstra's algorithm used to guide the manual tracing of a typical bone erosion in an MR image. Each light blue circle represents a pixel on the boundary between bone marrow and bone erosion, manually chosen by an operator. The red lines represent the shortest path between these pixels as determined by the algorithm.

An advantage to using shortest path graph search algorithms is that the operator can carefully specify the boundary surrounding a FOI without having to specify every pixel along that boundary. Nevertheless, this process is still much more time consuming than fully automated techniques because several points along the boundary must still be identified by the user to ensure a successful segmentation. Furthermore, the algorithm is restricted to 2D images. Therefore, each image comprising a volume of interest must be processed one slice at a time.

3.3.3 Watershed Segmentation

Watershed segmentation makes use of the image as a topographical map, where image values are used to represent altitudes, the highest of which form water-sheds which represent the border between segmentations. Unlike most other segmentation algorithms, watershed segmentation works on the entire image at one time instead of a single area or feature.

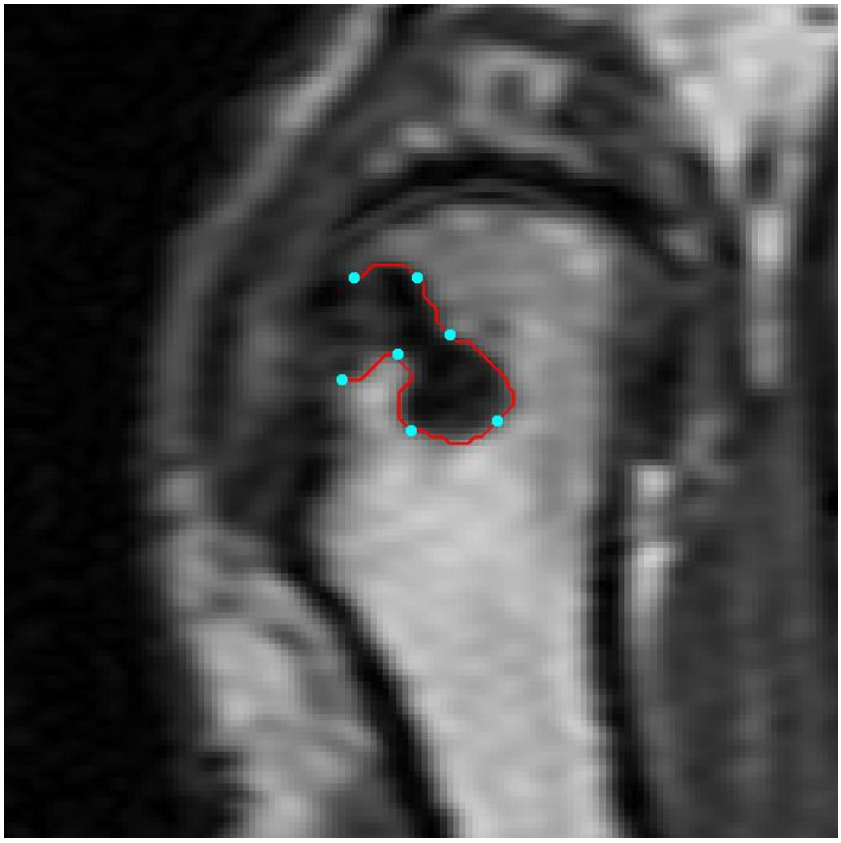

Figure 3.3: An example of Dijkstra's algorithm used to guide the manual tracing of a typical bone erosion in an MR image. The red line was determined by the algorithm and represents the shortest path between manually chosen pixels, which are denoted by light blue circles.

The algorithm requires a height map which is defined by the scalar intensities of an image. The result is a height value as a function of position:

$$H(\vec{r}) = h \tag{3.5}$$

where $\vec{r}$ is the position of any voxel in the image and *h* is the height defined by the image at that position. Figure 3.4 shows an example of *H* along one dimension. The algorithm also requires a controlling parameter known as level, or *L*. This parameter controls how sensitive the algorithm is to the boundaries which separate features in the image. A segmentation, $\Re$, is defined by a local minima at some voxel, $\vec{r}_o$, which includes all connected voxels in $\Re$ such that:

$$H(\vec{r}_i) \leq H(\vec{r}_o) + L : \forall \vec{r}_i \in \Re \tag{3.6}$$

The smaller the value of *L*, the more segmentations of a smaller size will be defined. If larger values of *L* are instead chosen, smaller segmentations combine into larger ones. The appropriate value for *L* depends on the image and the FOI. Figure 3.5 shows the watershed algorithm applied to a typical bone erosion, indicated by a black arrow, in an MR image. When applied to MR images, height maps are created by the gradient magnitude of the image. The initial and smoothed[1] gradient magnitude images are shown in figure 3.5(a) and (b),

[1] a low-pass filter is used to eliminate noise which can cause the algorithm to create too many segmentations

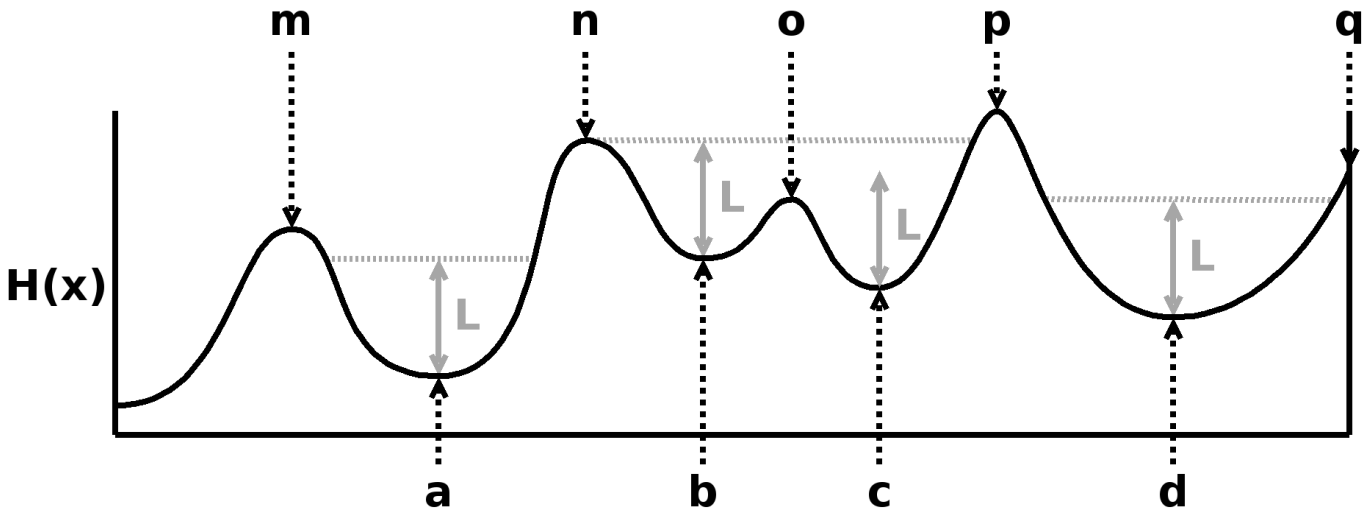

Figure 3.4: And example of watershed segmentation in one dimension. The height function, *H(x)*, define pools of water which fill up from local minima (*a*, *b*, *c* and *d*) and are bounded by local maxima (*m*, *n*, *o*, *p* and *q*) based on a filling level, *L*. Note that the watershed *o*, which separate minima *b* and *c*, is smaller than *L*, so these two pools merge into a single, larger pool.

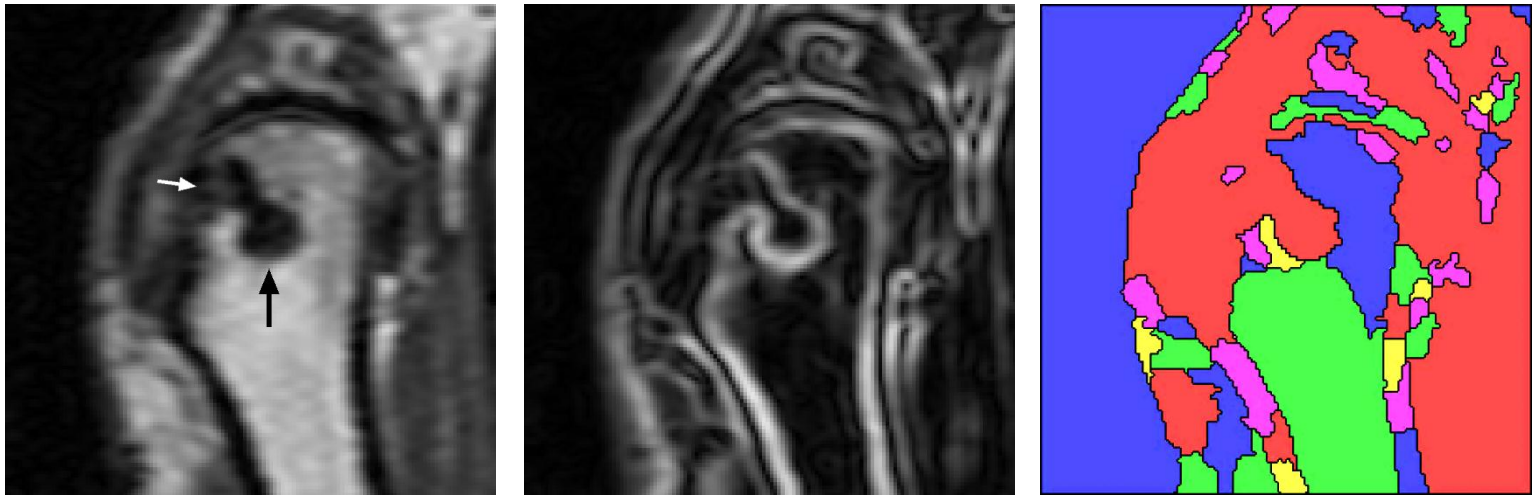

(a) Initial image (b) Gradient magnitude (height map) (c) Watershed segmentations

Figure 3.5: An example of watershed segmentation applied to a bone erosion, indicated by a black arrow, in the second metacarpal head. A magnification of an MR image is shown along with the combination of a low-pass and gradient magnitude filter (used as the height map by the watershed algorithm) and the segmentations resulting from applying the watershed algorithm, each outlined by a different colour. Note the missing boundary in the segmentation at the erosion's cortical bone interface, indicated by the small white arrow in the initial image.

respectively. Using the gradient magnitude image as the height map causes boundaries between features of different intensities in the initial image to act as high watersheds. The resulting segmentations are shown in figure 3.5(c) by different coloured outlines.

An advantage to watershed segmentation is that it can segment several features in an image simultaneously without requiring the placement of a seed point. However, a seed point must be used if the contour of a single, specific feature is desired and the extra processing time spent segmenting other features in an image is wasted. Furthermore, the algorithm is unable to correctly segment features that are not completely surrounded by watersheds (high gradients in MR images) or that have a range of signals, as is the case in some erosions.

3.3.4 Region Growing Segmentation

Region growing algorithms adopt a different approach to automated image segmentation. These algorithms require that one or more seed points be manually provided by an operator. The algorithm recursively expands from each seed point using controlling parameters to determine whether or not to expand the segmentation into neighbouring voxels. Depending on the type of controlling parameters used, region growing algorithms are useful for segmenting FOIs which are sharply bounded by distinguishing features.

The most basic type of region growing algorithm is known as connected thresholding. Given a set of seed points, each of their neighbouring 26-connected[2] voxels are examined. Each member of this set is included or excluded from the region, recursively, based on whether its intensity falls within lower and upper thresholds, T_l and T_u, respectively. A visual representation of the connected thresholding algorithm is shown in figure 3.6 and sample pseudocode is in the appendix section A.2.

Neighbourhood connection, confidence connection and isolated connection are variations of region growing. Neighbourhood connection extends the connected thresholding algorithm described above by only including voxels whose 26-connected neighbours all have intensities which fall between the thresholds, T_l and T_u. Confidence connection uses the connected threshold algorithm recursively, each time it determines the mean intensity of the segmentation and re-computes the algorithm using new thresholding boundaries defined by the expressions:

$$\begin{aligned} T_l &= \bar{I} - w\sigma \\ T_u &= \bar{I} + w\sigma \end{aligned} \tag{3.7}$$

[2] 26-connected voxels are defined as any two voxels which are directly or diagonally adjacent to each other in any Cartesian plane: $\pm\,\hat{x}, \pm\,\hat{y}, \pm\,\hat{z}, \pm\,\hat{x} \pm\,\hat{y}, \pm\,\hat{x} \pm\,\hat{z}, \pm\,\hat{y} \pm\,\hat{z}, \pm\,\hat{x} \pm\,\hat{y} \pm\,\hat{z}$

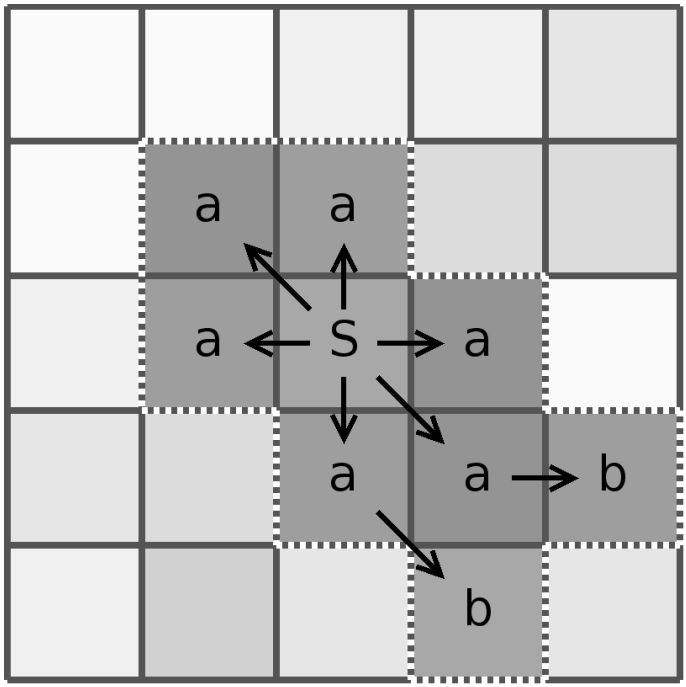

Figure 3.6: A 2D example of the connected threshold algorithm. Consider the pixel (square) marked “S” as a pixel identified as seed point. The algorithm checks each neighbor from this seed pixel, as denoted by black arrows, adding any pixels that are within the threshold (pixels marked “a”). The next iteration repeats the same process using each added pixel “a” as new seed points, thus adding the pixels marked “b”.

where $\bar{I}$ and σ are the mean intensity and standard deviation of voxels included in the segmentation determined from the last iteration of the algorithm, respectfully, and *w* is a user-defined weighting parameter.

Finally, isolated connection replaces one of the threshold values with an exclusion seed point. The algorithm determines the lower or upper threshold such that the exclusion seed point does not connect to any region grown from the regular seed point(s). Figure 3.7 shows the connected threshold algorithm applied to a typical bone erosion, indicated by a large white arrow, in an MR image. Since erosions in T_1-weighted images have a very low signal, the lower threshold is set to zero. Determining the upper threshold is less obvious. Sub-figures (b), (c) and (d) show the segmentation resulting from using upper thresholds of 16%, 31% and 47% of maximum intensity (100% or bright white), respectively.

An advantage of region growing algorithms is that they very clearly outline boundaries which have sharp gradients. Furthermore, these region based segmentations are not affected by the presence of other features with similar intensities if they are spacially well separated. A disadvantage to region growing algorithms is that they are unable to accurately distinguish features with small gradient intensities. In the case of MR images of erosions these small gradient intensities can arise at the boundary between bone erosions and soft tissue where cortical bone is absent.

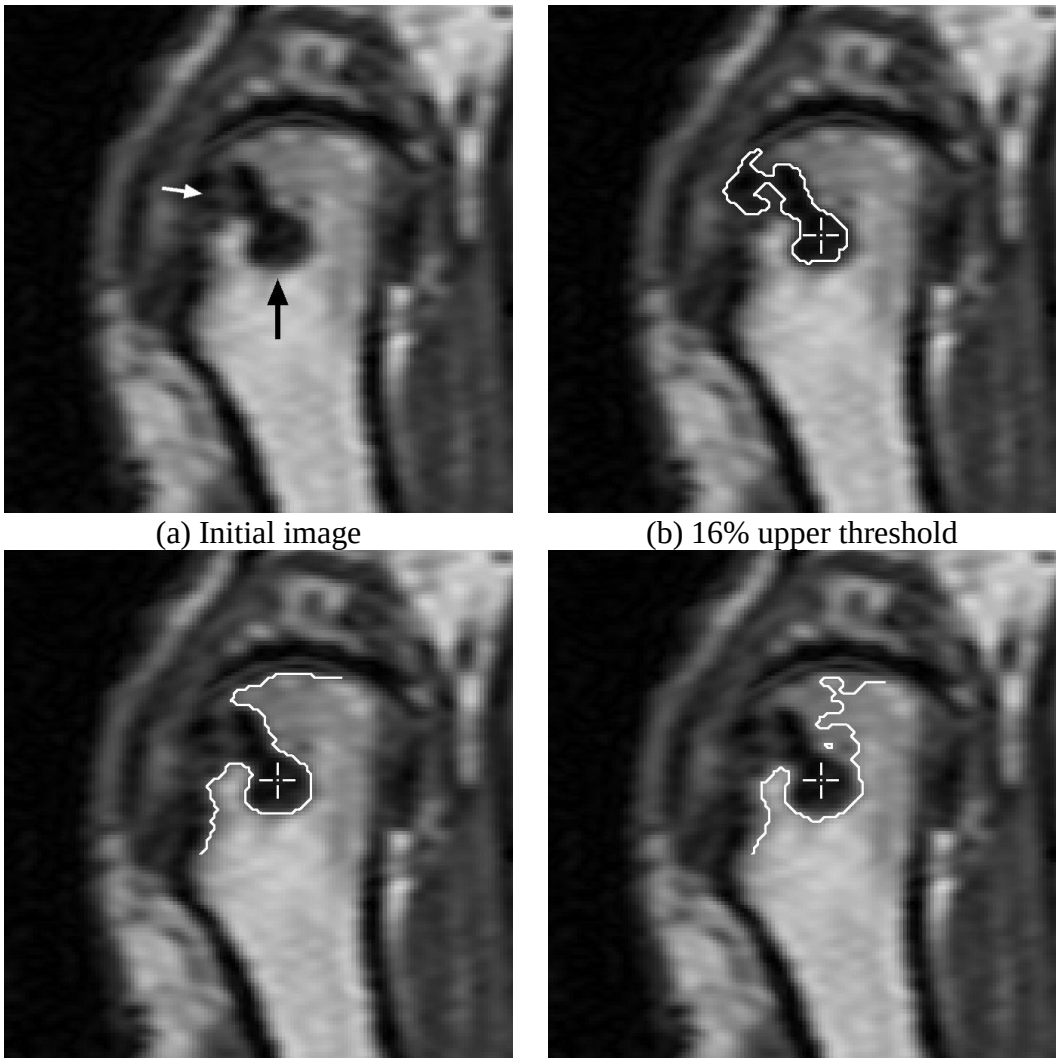

(a) Initial image (b) 16% upper threshold

(c) 31% upper threshold (d) 47% upper threshold

Figure 3.7: An example of connected thresholding segmentation applied to a bone erosion, indicated by a large black arrow, in the second metacarpal head in a Magnetic Resonance (MR) image. (a) shows a magnification of the 2nd metacarpal head, (b), (c) and (d) show the seed point and outline of the segmentation from connected thresholding using a lower threshold of 0 and upper threshold of 16%, 31% and 47% of the maximum image intensity, respectfully. Note the missing boundary in the segmentation at the erosion's cortical bone interface, indicated by the small white arrow

3.3.5 Level-Set Segmentation

Level-set (LS) segmentation delineates FOIs by tracking the evolution of a time-based level-set function, or propagating front, according to a differential equation. A segmentation is defined by the front at any discrete propagation time. This technique is useful for segmenting features which do not necessarily have distinct boundaries, particularly where the FOI is vaguely circular in 2D images or spherical in 3D images.

For any N-dimensional image, consider a level-set function which has the same dimension as the image plus time, or $\Psi(\vec{r}, t)$. The partial differential level-set equation controlling the propagation of Ψ is then:

$$\frac{d}{dt}\Psi = -w_\alpha \vec{A}(\vec{r}) \cdot \nabla\Psi - w_\beta P(\vec{r})\left|\nabla\Psi\right| + w_\gamma Z(\vec{r})\kappa\left|\nabla\Psi\right| \tag{3.8}$$

where $\vec{A}(\vec{r})$, $P(\vec{r})$ and $Z(\vec{r})$ are the advection, propagation and curvature terms, respectively, w_α, w_β, w_γ are their respective weights and κ is the mean curvature. A common implementation of LS segmentation is the fast marching level-set algorithm, described by Sethian (1999). Pseudocode for the fast marching level-set algorithm is given in appendix section A.3. This implementation simplifies equation 3.8 by removing the advection and curvature terms. The propagation term, $P(\vec{r})$, is provided by the sigmoid of the gradient magnitude of the image:

$$P(r) = S\left(\left|\nabla I(\vec{r})\right|\right) = \left[1 + \exp\left(-\frac{\left|\nabla I(\vec{r})\right| - \beta}{\alpha}\right)\right]^{-1} \tag{3.9}$$

where α and β are free parameters which define the width and intensity of the sigmoid function, respectively. Figure 3.8 demonstrates a propagation front at several successive time points as it travels through such a speed function. The numbers in the figure represent the cost of traversing the pixel (square) such that the total cost of traversing from the origin of the front (the pixel marked 0) to any pixel is the sum of all numbers along that path.

Figure 3.9 shows an example of the propagation term, known as a time map, determined from an MR image. The resulting time map in sub-figure (c) represents how quickly the propagation front can expand, where the brighter the pixel the faster the propagation. The choice to use the sigmoid of the gradient magnitude of the image allows the propagation front to expand very quickly near areas with low gradients and to slow down severely near areas of high gradients. Figure 3.10 shows several segmentations of a bone erosion in a metacarpal head resulting from the time map in sub-figure (c) and by varying the free parameters, α and β, in the sigmoid function from equation 3.9.

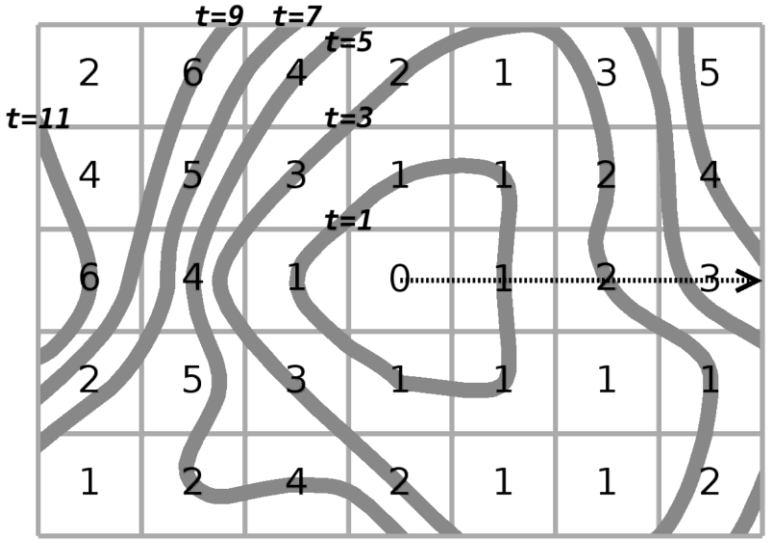

(a) 2D view

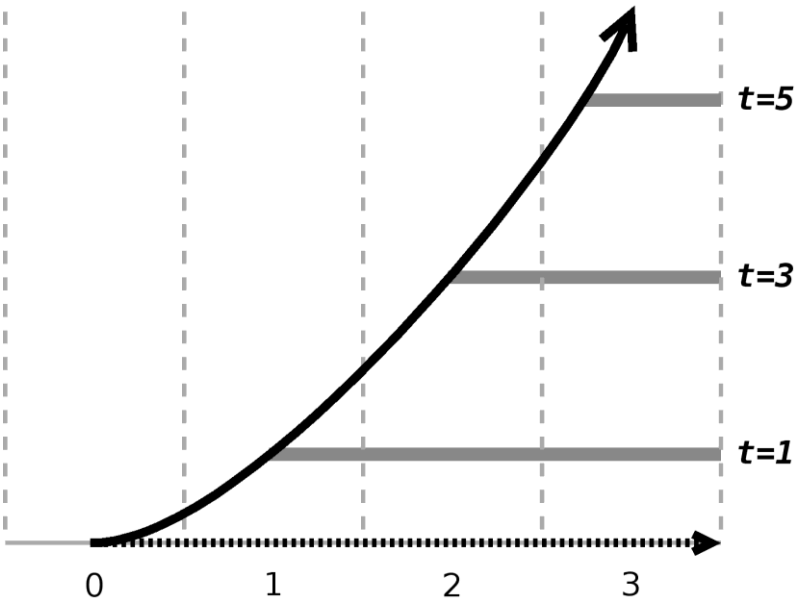

(b) 1D view

Figure 3.8: An example of the fast marching algorithm. (a) The numbers in each pixel (square) represents the speed function for traversing that pixel. The propagation front is displayed for six time points: t = 1, 3, 5, 7, 9 and 11. (b) The 1 dimensional propagation front for the dotted black line in (a).

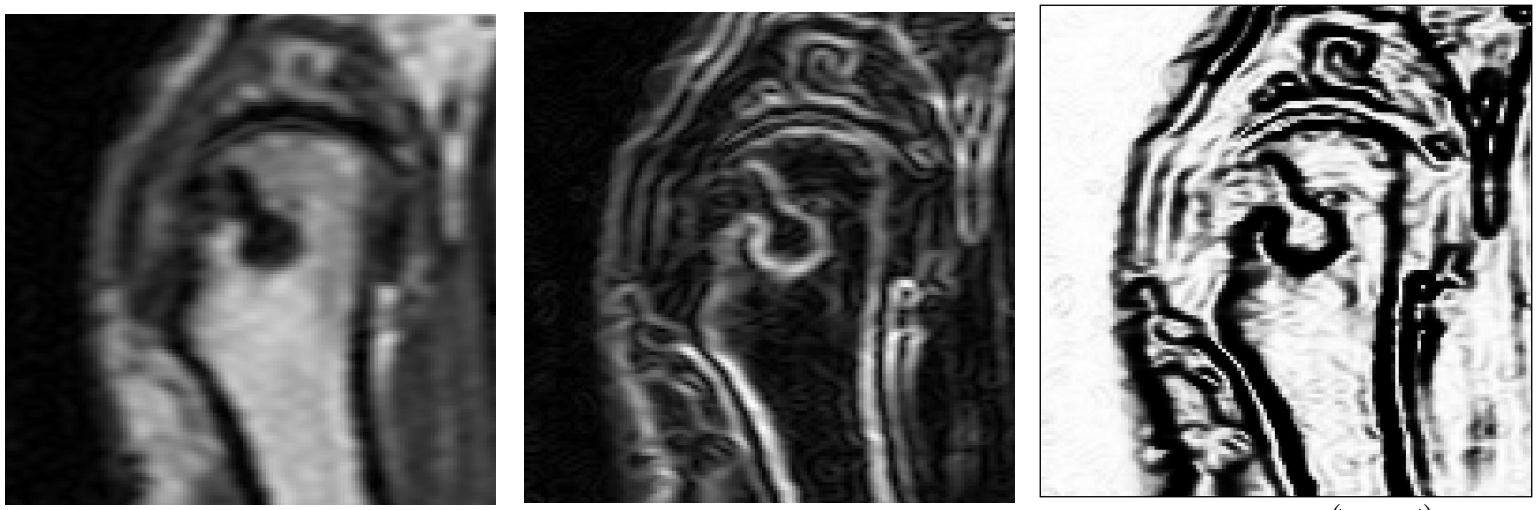

Initial image, $I(\vec{r})$ (b) Gradient magnitude, $|\nabla I(\vec{r})|$ (c) Sigmoid, $S(|\nabla I(\vec{r})|)$

Figure 3.9: An example of how the propagation term in equation 3.8, referred to as the time map in the fast marching level-set algorithm, created from an initial Magnetic Resonance (MR) image. (a) shows a magnification of the 2nd metacarpal head, (b) is the gradient magnitude of the image in (a) and (c) is the sigmoid of the gradient image in (b) with α set to -16% and β set to 35% of maximum image intensity.

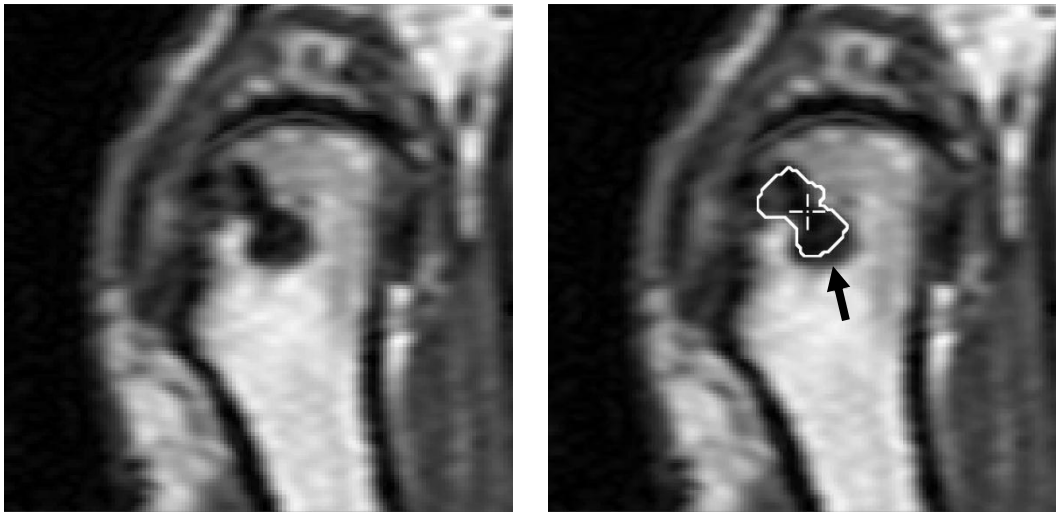

(a) Initial image

(b) α = -16%, β = 24%

(c) α = -16%, β = 35%

(d) α = -16%, β = 47%

Figure 3.10: An example of fast marching segmentation applied to a bone erosion in the second metacarpal head in a Magnetic Resonance (MR) image. (a) shows a magnification of the 2nd metacarpal head and (b), (c) and (d) show the seed point and outline of the fast marching segmentation using different parameters in the sigmoid function in equation 3.9. All three segmentations have α set to -16% and (b), (c) and (d) have β set to 24%, 35% and 47% of maximum image intensity, respectfully. Note the poor delineation between erosion and bone denoted by the black arrow in image (b) and the white arrow in image (c).

Other level-set algorithms include those that make use of the advection, $\vec{A}(\vec{r})$, and curvature, $Z(\vec{r})$, terms in equation 3.8. For example, Malladi et al. (1995) describe a so-called "shape modeling" level-set algorithm that includes the propagation and curvature terms. As well, Caselles et al. (1997) describe a "geodesic active contour" algorithm which is a level-set algorithm with all three terms.

An advantage to level-set algorithms is that FOIs do not need to be strictly surrounded by tissues or features with significantly different intensities. Unlike region growing algorithms, level-set algorithms do not require threshold values, allowing them to segment features with inhomogeneous intensities. A disadvantage to level-set algorithms is that they tend to poorly delineate the boundary between features as compared to region growing algorithms. Furthermore, small changes in the position of the seed point(s) change the segmentation, reducing their reproducibility.

3.4 Summary of Erosion Segmentation in MR Images

There are four distinct challenges when delineating multi-slice bone erosions in MR images: localization, multi-slice contouring, delineation of the boundary between bone erosion and bone marrow and the delineation of the boundary between bone erosion and non-marrow tissue including edema, cortical bone,

synovial fluid and cartilage. The first challenge in segmenting bone erosions in MR images is the ability to determine the boundaries of a single region of interest distinctly from other image features, or "localization". For example, as discussed in the previous sections, manual tracing, region growing, level-set and least-cost graphing algorithms are capable of contouring a single region of interest whereas naïve thresholding and watershed algorithms generate contours over an entire image without a means of differentiating between a region of interest and other image features. The second challenge in segmenting bone erosions in MR images is the ability to determine the boundaries of erosions which appear in multiple image slices. Naïve thresholding, watershed, region growing and level-set algorithms are able to define boundaries of features which span multiple image slices whereas manual tracing and least-cost graph algorithms require the boundaries of an erosion in each slice of an MR image to be considered individually without consideration of the erosion's boundaries on other slices. The third challenge in segmenting bone erosions in MR images is the ability to delineate the boundaries between the characteristic low signal of eroded bone and bright signal of non-eroded bone marrow. All of the segmenting techniques discussed in this section are capable of identifying bone erosion/marrow boundaries except for level-set algorithms. Finally, the fourth challenge in segmenting bone erosions in MR images is the ability to delineate the boundaries between the characteristic low signal of eroded bone and the low to mid-level

signals of other, non-marrow tissues surrounding the erosion such as edema, cortical bone, synovial fluid and cartilage. The level-set algorithm is able to identy all bone erosion/non-marrow boundaries whereas all other algorithms fail to identify some or all erosion/non-marrow boundaries.

Table 3.2 summarizes the segmentation techniques discussed in this chapter along with their effectiveness in overcoming the challenges associated with segmenting bone erosions in a contiguous stack of MR images. Since none of the techniques meet all four challenges associated with automatic erosion segmentation, a hybrid approach which combines the strengths of two or more of these techniques may be the most optimum approach to this segmentation problem. In chapter 4 the development and testing of a hybrid algorithm which forms the cornerstone of this thesis is described.

Table 3.2: A list of segmentation techniques discussed in this section that were candidates for erosion segmentation. The effectiveness of each for overcoming the challenges of segmenting bone erosions as they appear in MR images is given. These challenges include the segmentation of a single erosion of interest (localization), multi-slice contouring and the correct delineation of the erosion boundary with bone marrow and the synovium. Note that none of these techniques effectively overcome all four challenges.

	Localization	**Mutli-slice contouring**	**Delineation of erosion/marrow boundaries**	**Delineation of erosion/synovium boundaries**
Manual Tracing	yes	no	yes	no
Naïve Thresholding	no	yes	yes	no
Least-Cost Graphs	yes	no	yes	no
Watershed	no	yes	yes	no
Region Growing	yes	yes	yes	no
Level-Set	yes	yes	no	yes

Chapter 4

Bone Erosion Segmentation Algorithm

4.1 Introduction to Hybrid Algorithms

Automated image segmentation algorithms which combine two or more segmentation techniques are known as hybrid segmentation algorithms. These hybrid algorithms are usually designed by combining the strengths of multiple segmentation algorithms in order to solve a specific segmentation problem.

Although the use of hybrid segmentation approaches in medical imaging is relatively new, there are successful applications which have been reported for different imaging modalities and purposes. For example, Franaszek et al. (2006) describe using a combination of region growing, fuzzy connectedness (Udupa and Samarasekera 1996) and level-set algorithms to automatically detect polyps on CT colonography images. Gu et al. (2006) combined level-set and morphological reconstruction for general use in MR images of the brain, heart and kidneys. Hybrid algorithms are also used in 2D imaging modalities. Lee et al. (2007) describes using a combination of level-set and morphological scale-space analysis of fundus auto-fluorescence images to quantify macular degeneration and Ray et al. (2008) describe a hybrid algorithm used to examine oral sub-mucous fibrosis in light microscopic histopathological images.

Given the success with which hybrid algorithms performed in segmenting these varied features in CT, MR and light microscope images, their application to segmenting MR based erosions seemed worthwhile.

4.2 Development of a Hybrid Algorithm for Erosion Segmentation

A new hybrid algorithm was developed to automatically segment RA bone erosions from MR images. This algorithm combines Region Growing (RG) and LS algorithms using mathematical logic operators. The purpose of this new hybrid algorithm is to create a segmentation scheme which is sensitive to regions and boundaries by combining the region-based segmentation paradigm of RG algorithms with the boundary-based segmentation paradigm of LS algorithms.

An overview of the RG and LS algorithms is given in figure 4.1. It shows a flowchart describing the image filters used by the fast marching variant of the LS algorithm and the connected thresholding variant of the RG algorithm. Both segmentation algorithms are outlined by dotted lines. Internal filters used by the algorithms are depicted as boxes listing the filter's name and controlling parameters. The flow of the input image through the internal filters (also referred to as the pipeline) is represented by small black arrows.

The fast marching filter, shown as a pipeline on the left side of figure 4.1, has one input and one output image represented by a large white arrow at the top and

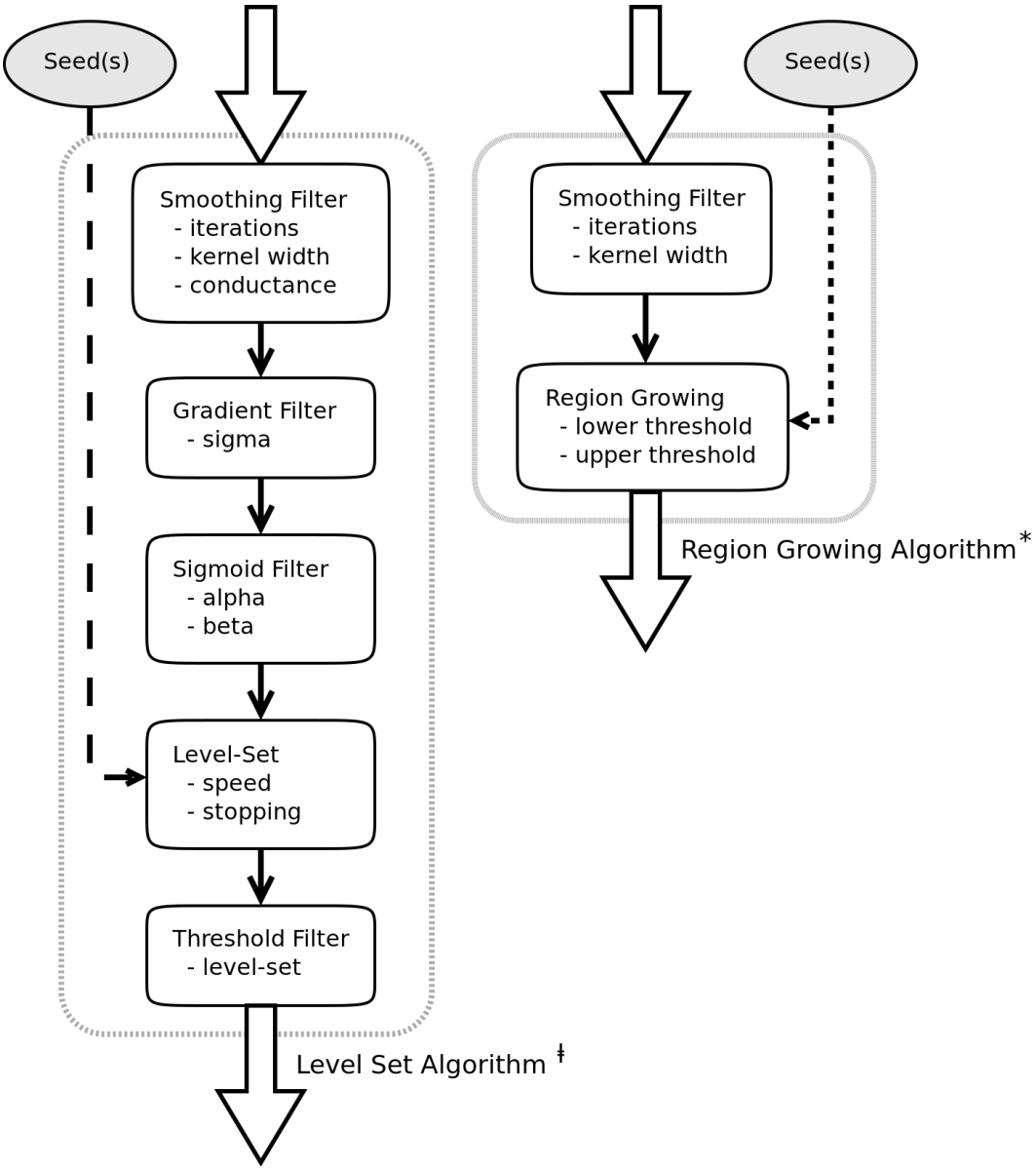

Figure 4.1: A flowchart describing the internal filters used by the level set and region growing algorithms on the left and right, respectively. Filters used internally by the segmentation algorithms are shown as a box listing their name and controlling parameters. Figure 4.2 depicts how these algorithms are combined into a single, hybrid algorithm.

bottom of the figure, respectively. The internal pipeline includes, in order, a smoothing, gradient, sigmoid, level-set and threshold filter. First, a curvature anisotropic diffusion filter is used as the smoothing filter. The filter is an edge-preserving smoothing filter which uses a modified curvature diffusion equation to perform anisotropic diffusion. Three controlling parameters are used by the filter, the number of iterations, kernel width and conductance. The number of iterations define how many times to recursively perform the smoothing filter, the kernel width (also known as the time step) defines the width of the smoothing neighbourhood and the conductance limits the smoothing around the edges of features in the image. Next, a gradient magnitude filter using a Gaussian-based smoothing kernel is used as the gradient filter on the output from the smoothing filter. This filter uses a single controlling parameter, sigma, which defines the standard deviation of the Gaussian smoothing kernel or neighbourhood. Figure 3.9(b) shows an example of this filter on an MR image. Then, the sigmoid filter uses two controlling parameters, α and β to perform a non-linear mapping on the output from the gradient filter. The α and β parameters (as defined in equation 3.9) control the width and intensity of the sigmoid function, respectively. Figure 3.9(c) shows an example of this filter on an MR image. Next, the fast marching level-set filter, as described in section 3.7.7, is performed on the output from the sigmoid filter. Finally, a binary threshold filter is used to convert the output from the level-set filter into an image mask that defines the output segmentation.

The connected thresholding filter, shown as a pipeline in the right column of figure 4.1, has one input and one output image represented by a large white arrow at the top and bottom of the figure, respectively. The internal pipeline includes, in order, a smoothing and region growing filter. First, a curvature flow filter is used as the smoothing filter. Two controlling parameters are used by the filter, the number of iterations and kernel width. As with the curvature anisotropic diffusion filter, the number of iterations define how many times to recursively perform the smoothing filter and the kernel width defines the width of the smoothing neighbourhood. Finally, a connected thresholding region growing filter, as described in section 3.3.4, is performed on the output from the smoothing filter. This filter creates an image mask that defines the output segmentation.

The hybrid segmentation algorithm is a 2D image filter which combines the output from the RG and LS filters described in figure 4.1, one slice at a time. Mathematically this algorithm is defined by the following equation:

$$H(S_{RG}, S_{LS}) = \left\{\left[\Delta_n(S_{RG}) \wedge \Delta_n(S_{LS})\right] \vee S_{RG}\right\} \wedge S_{LS} \tag{4.1}$$

where S_{RG} and S_{LS} are the RG and LS segmentations, respectively, and $\Delta(S)$ is a dilated border function. Figure 4.2 shows a flowchart of equation 4.1. Both filters are passed through a border and dilating filter before being combined together using logical AND ($\wedge$) and OR ($\vee$) filters. The dilated border function

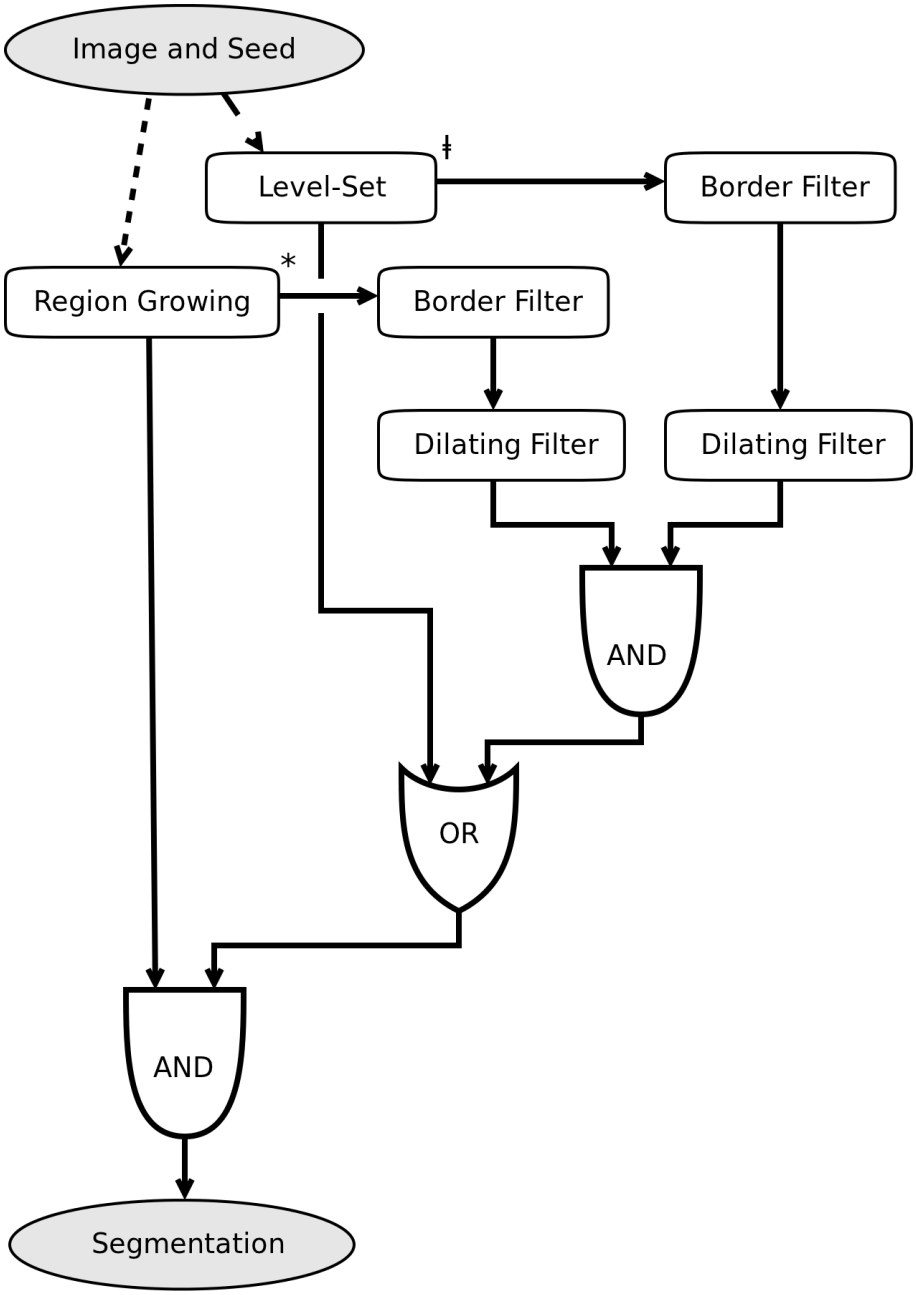

Figure 4.2: A flowchart describing the internal filters used in the hybrid segmentation filter. The image and seed(s) are input into the Region Growing (RG) and Level Set (LS) filters which are described in more detail in figure 4.1. The output of these filters are passed to border, dilation and logical AND ($\wedge$) and OR ($\vee$) filters, as shown by black arrows. The resulting segmentation is the output of the final AND filter at the bottom of the flowchart.

is a linear combination of border and dilation filters defined by the following equation:

$$\Delta_n(S) = D_n\left[\delta(S)\right] \tag{4.2}$$

where $\delta(S)$ is a border filter which transforms the image S by removing all pixels that are not directly adjacent to the border of the segmentation and $D_n(S)$ is a dilation filter which performs a binary dilation on the image S by n pixels.

Figure 4.3 shows an example of each step of equation 4.1 as image filters applied to a typical MR image. In is important to note that these steps are applied to each image slice, one at a time. The magnification of a typical slice of an MR image containing an erosion before segmentation is shown in subfigure (a). Sub-figure (b) show the outline, S_{RG}, and dilated border, $\Delta_r(S_{RG})$ of the RG segmentations as a thin white line and thick grey band, respectively. Subfigure (c) shows the same as (b), but for the LS segmentation. Next, the logical AND of the dilated borders of the RG and LS segmentations is shown in sub-figure (d), followed by the logical OR of the RG segmentation in (e) and the logical AND of the LS segmentation in (f).

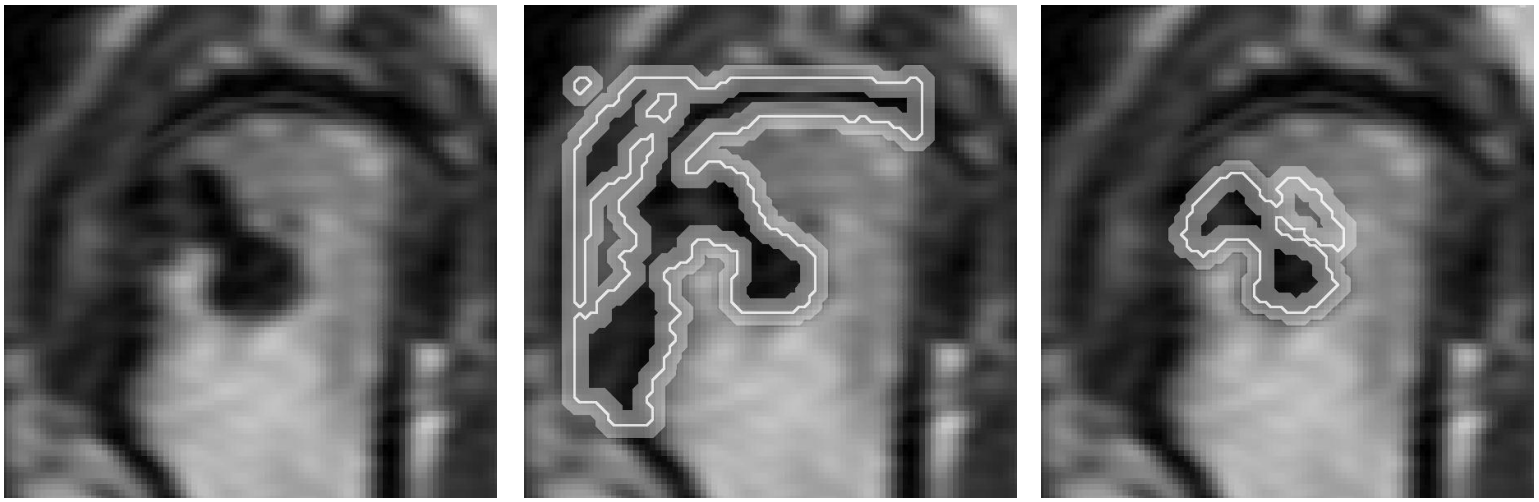

(a) Input image.

(b) The white border represents the border of the RG segmentation, S_{RG}, and the thick gray border represents the dilation of that border, $\Delta_5(S_{RG})$. These two steps are represented on figure 4.2 as A and B

(c) The white border represents the border of the RG segmentation, S_{LS}, and the thick gray border represents the dilation of that border, $\Delta_5(S_{LS})$. These two steps are represented in figure 4.2 as C and D

Figure 4.3: Magnification of a single slice of the erosion used to demonstrate the hybrid algorithm. These steps are described by equation 4.1 and the flowchart in figure 4.2.

(d) The logical AND operation between the dilated region growing segmentation border, $\Delta_5(S_{RG})$, and the dilated level-set segmentation border, $\Delta_5(S_{LS})$. This is represented in figure 4.2 as E

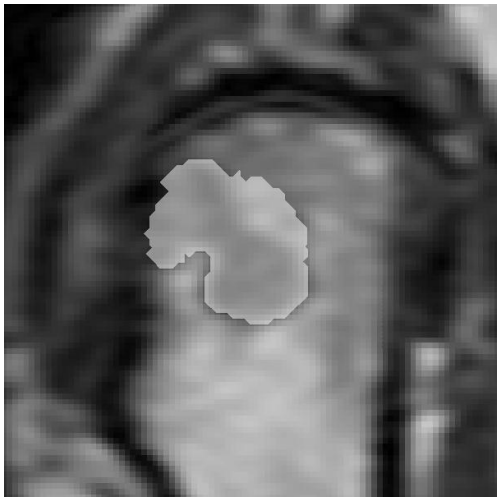

(e) The logical OR operation between the level-set segmentation, S_{LS}, and the previous image. This is represented in figure 4.2 as F.

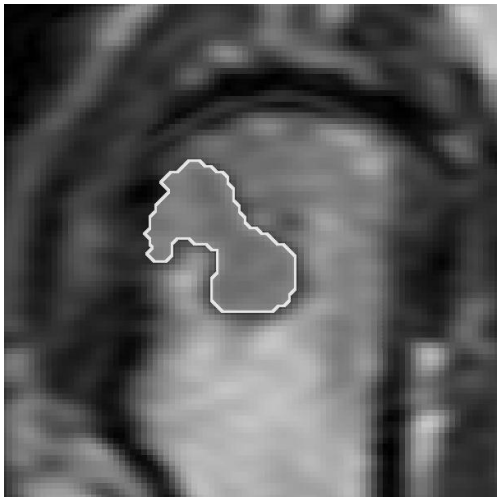

(f) The logical AND operation between the region growing algorithm, S_{RG}, and the previous image. This is represented in figure 4.2 as G.

Figure 4.3 (cont): Magnification of a single slice of the erosion used to demonstrate the hybrid algorithm. These steps are described by equation 4.1 and the flowchart in figure 4.2.

4.3 Controlling Parameters

There are a total of 15 controlling parameters used to optimize the hybrid segmentation algorithm: 9 for the LS algorithm, 4 for the RG algorithm and 2 for the hybrid algorithm which combines the LS and RG segmentations. Requiring a human operator to define a large number of parameters makes the algorithm more likely to succeed but increases the time needed to segment an image and may reduce the reproducibility of the segmentations. Furthermore, many of these parameters are not intuitive and require knowledge of the underlying algorithms in order to understand the effects they have on the final segmentation. This makes the algorithm difficult to use in a clinical setting.

In order to address these shortcomings each of the 15 controlling parameters were investigated independently using a test set of 8 erosions. The goal was to determine which parameters could be set to a constant value across a successful segmentation of all test erosions, thus reducing the need for a human operator to determine them manually. For those parameters which could not remain constant for all test erosions, a small finite set of values was determined which, when chosen from, would successfully segment all test erosions. Finally, the set of parameter values determined using the aforementioned procedure were compared with each other (comparing the values used for all 15 parameters as a group between each test erosion) to determine whether any two erosions used similar or

the same set of values. This resulted in reducing the tuning required by a human operator from choosing 15 scalar values down to choosing a single categorical value.

4.3.1 Constraining Parameter Values

To minimize the variability of erosion measurement and to reduce the number of user defined inputs required to initiate the segmentation, the parameters required by the RG, LS, and hybridization steps of the segmentation are subjected to minimal control by the user. As such, five sets of parameters were identified from a training data set of eight images. For each erosion in the test set, the four parameters required by the RG algorithm, the nine parameters required by the LS algorithm, and the two parameters required to combine the RG and LS segmentations were tuned individually until the segmentations most closely matched with those of the gold-standard (manually traced and radiologist-corrected) segmentations. Of the eight sets of parameters derived by this procedure, any sets which were identical or having near identical values for all 15 parameters were grouped together. Table 4.1 lists the resulting parameter values for all test images as determined by this procedure.

4.3.2 Parameter Sets

Of the 15 parameters required by the hybrid algorithm only 3 needed to be varied in order to segment all test erosions. Furthermore, 4 of 8 of the test erosions were segmented using the same values for all parameters. This resulted in a total of 5 sets of parameters in order to successfully segment all test erosions. These sets are listed in table 4.2. Therefore, human operators were presented with choosing one of the five parameter sets (labeled by letter: A, B, C, D, and E) instead of providing scalar values for 15 individual parameters. This greatly simplifies the choices necessary to segment erosions. However, since it is not guaranteed that this limited group of parameter-sets will be able to segment all possible erosions, the algorithm will be unable to segment some fraction of erosions it is presented with. Figures 4.4, 4.5 and 4.6 demonstrate various parameter-sets applied to a large (119.3 mm^3), medium (63.7 mm^3) and small (23.4 mm^3) erosion, respectfully. Each figure also includes 3D renderings of the successful, multi-slice segmentation.

4.4 Seed Re-Positioning

The location of the seed point placed by the rater can affect the borders of the erosion outlined by the RG and LS algorithms and the final hybrid boundary. Therefore, to increase the precision of the final segmentation, the algorithm was automatically re-run with a seed point corresponding to the center of mass of the

initial segmented area of the slice where the user- selected seed was positioned. The segmentation steps were repeated and the seed point was automatically re-positioned at the new center of mass. This procedure continued until two

Table 4.1: A list of all controlling parameters used in the hybrid algorithm and their values for the 8 test erosions determined by the procedure described in section 4.3.1. Note that 12 of the 15 parameters (values in grey) have the same value for all test erosions.

	#1	**#2**	**#3**	**#4**	**#5**	**#6**	**#7**	**#8**
Level Set Parameters								
Smoothing iterations	4	4	4	4	4	4	4	4
Smoothing time step	0.01	0.01	0.01	0.01	0.01	0.01	0.01	0.01
Smoothing conductance (mm)	0.547	0.547	0.547	0.547	0.547	0.547	0.547	0.547
Gradient *s*	0.05	0.05	0.05	0.05	0.05	0.05	0.05	0.05
Sigmoid α (% intensity)	-3.9	-2.0	-3.9	-1.2	-3.9	-11.8	-19.6	-3.9
Sigmoid β (% intensity)	15.7	23.5	15.7	31.4	15.7	11.8	0.8	15.7
Fast-marching stopping (% intensity)	11	11	11	11	11	11	11	11
Lower threshold (% intensity)	0	0	0	0	0	0	0	0
Upper threshold (% intensity)	15.7	15.7	15.7	15.7	15.7	15.7	15.7	15.7
Region Growing Parameters								
Smoothing iterations	4	4	4	4	4	4	4	4
Smoothing time step	0.01	0.01	0.01	0.01	0.01	0.01	0.01	0.01
Lower threshold (% intensity)	0	0	0	0	0	0	0	0
Upper threshold (% intensity)	27.5	39.2	27.5	27.5	27.5	47.1	31.4	27.5
Hybrid Parameters								
Dilating (mm)	1.367	1.367	1.367	1.367	1.367	1.367	1.367	1.367
Island threshold (mm^2)	0.748	0.748	0.748	0.748	0.748	0.748	0.748	0.748

Table 4.2: A list of all parameter-sets determined by grouping parameters found in table 4.1. Note that parameters which are not listed in this table are constant and listed in table 4.1.

Set	Level Set Sigmoid α (% intensity)	Level Set Sigmoid β (% intensity)	Region Growing Upper Threshold (% intensity)
A	-3.9	15.7	27.5
B	-1.2	31.4	27.5
C	-2.0	23.5	39.2
D	-19.6	8.0	31.4
E	-11.8	11.8	47.1

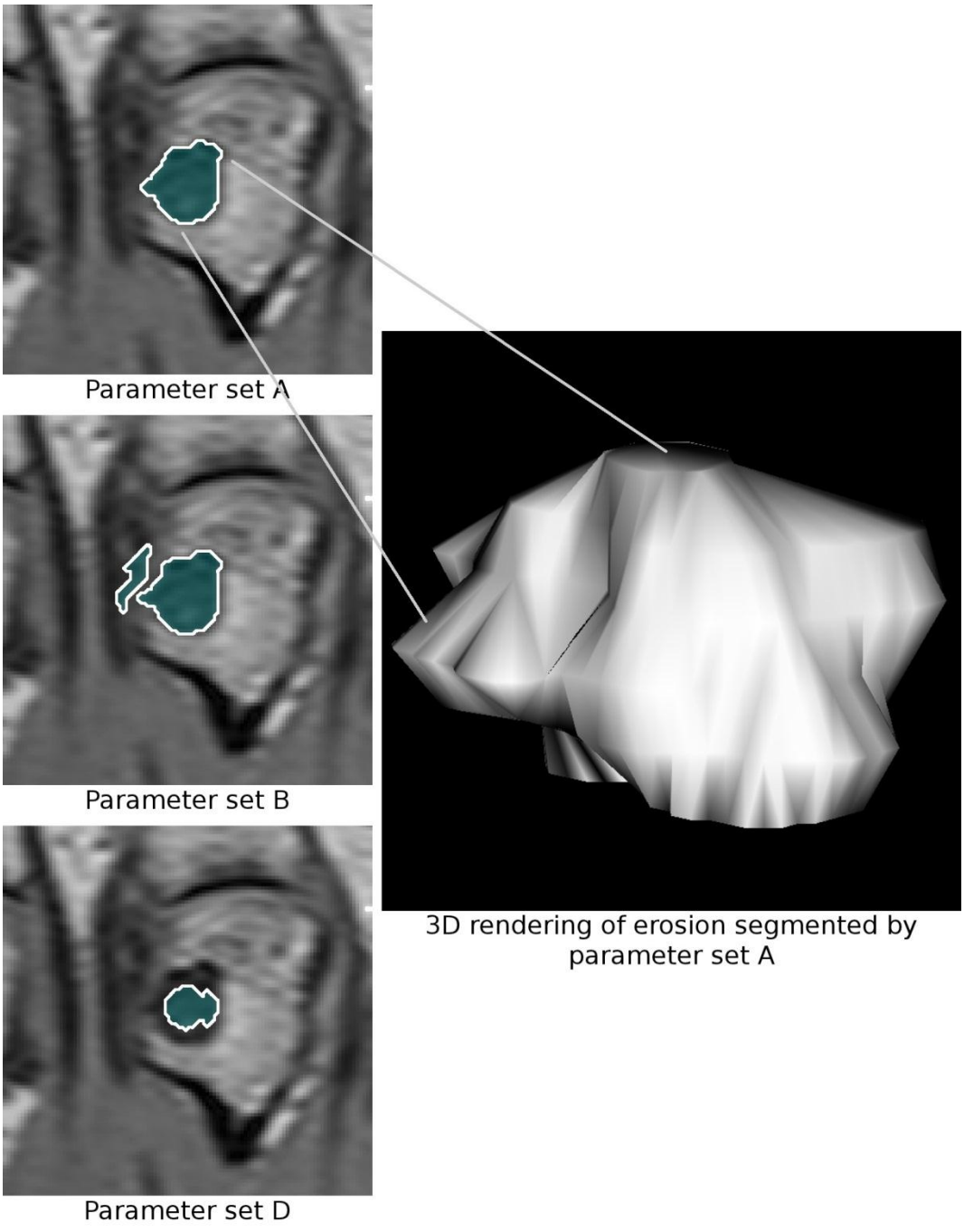

Figure 4.4: A large erosion (119.3 mm^3) successfully segmented by parameter set A.

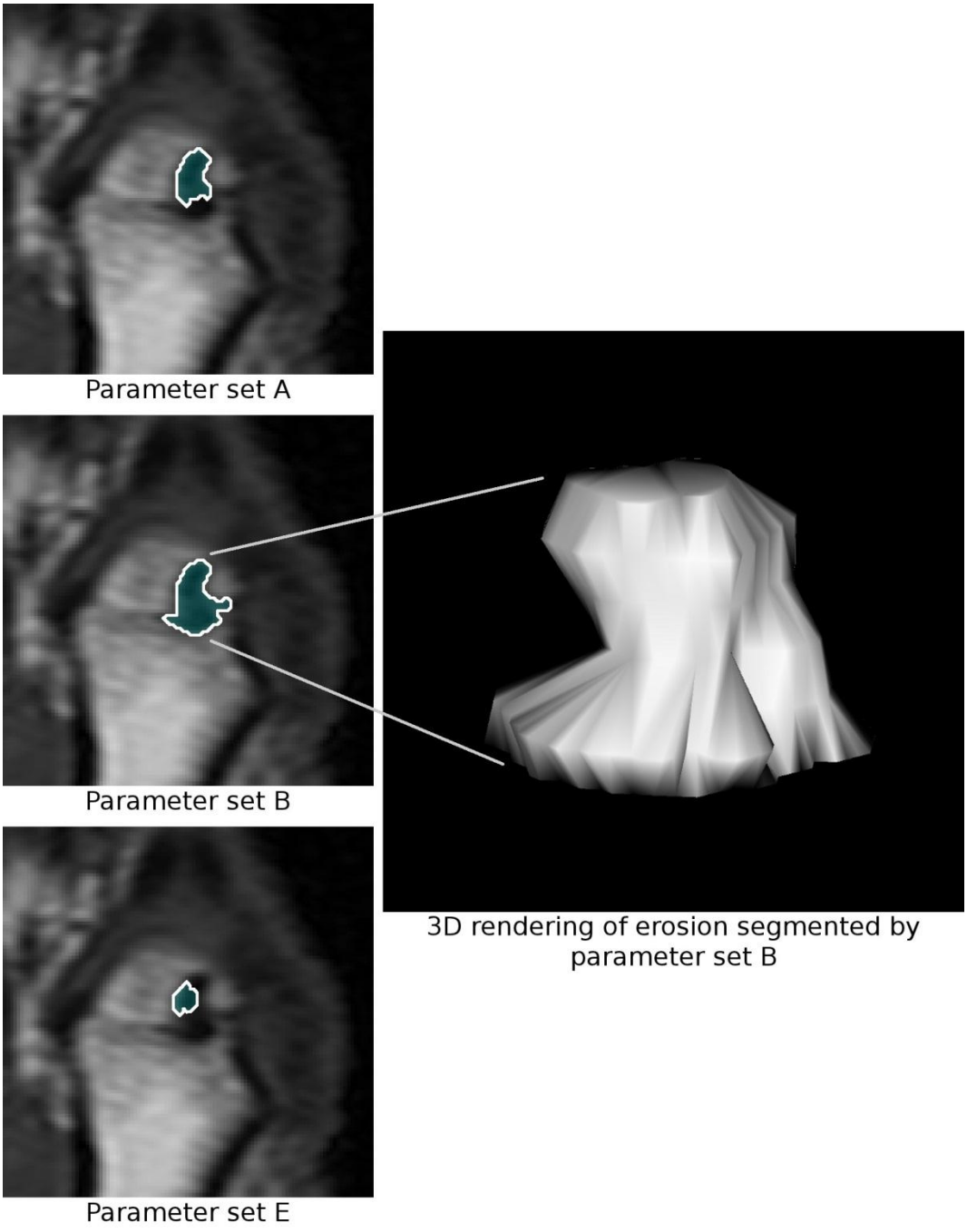

Figure 4.5: A medium erosion (63.7 mm^3) successfully segmented by parameter set B.

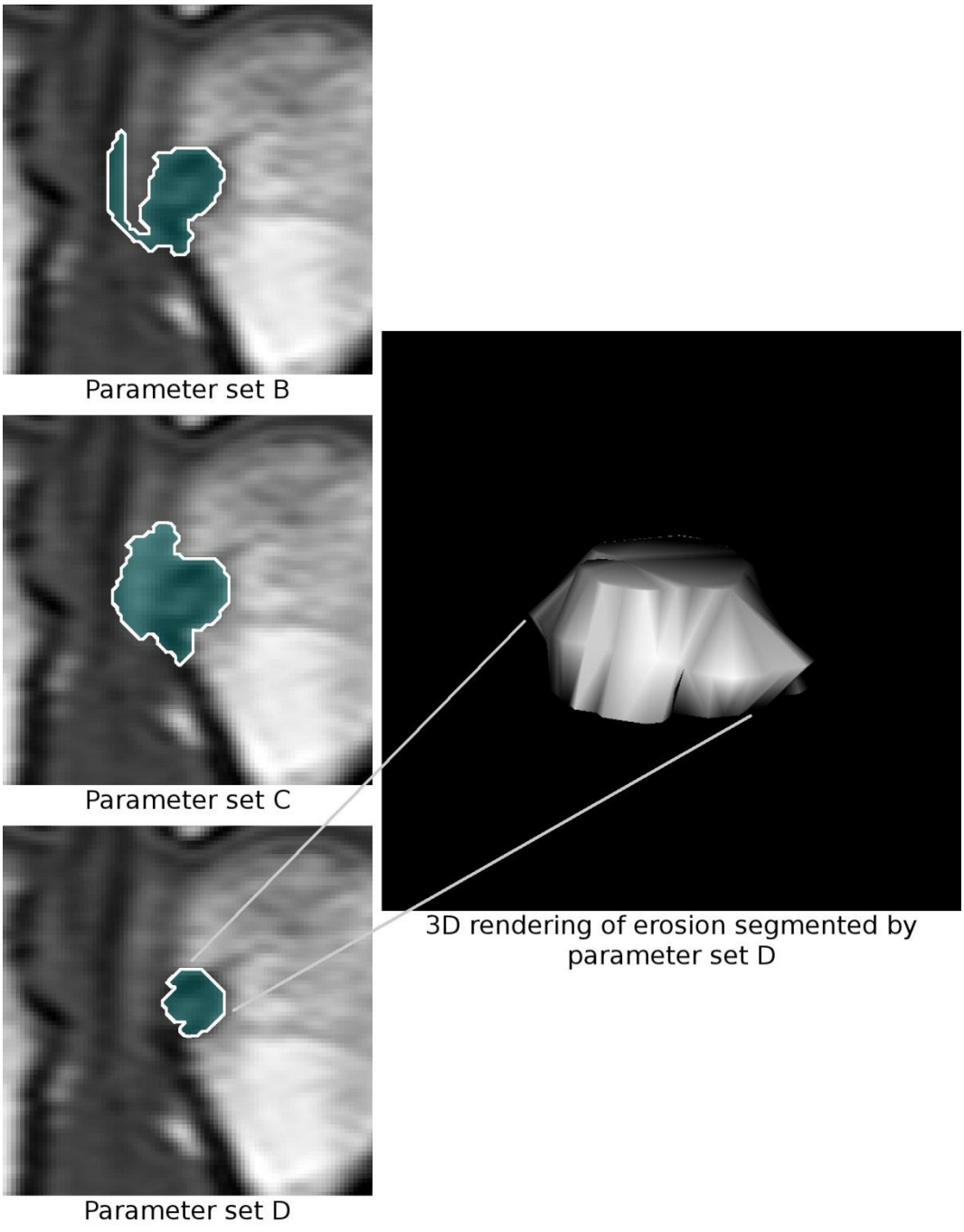

Figure 4.6: A small erosion (23.4 mm^3) successfully segmented by parameter set D.

consecutive seed positions were the same, thereby denoting a stable segmentation of the erosion volume. However, if after several iterations the seed point did not stabilize, the rater instead placed the seed point as close to the center of the erosion as possible without automatic re-positioning. Placement instability occurred when most of the cortical bone surrounding the erosion was destroyed, causing the center of mass of the segmentation to always be further from the bone than the seed point.

4.5 Measuring Volume

4.5.1 Reconstruction of 2D Segmentations into a 3D Volume

Once the erosion has been segmented its volume must be determined. Since erosions are contained in a series of 2D images their volume can only be determined from segmentations made up of 2D contours by reconstructing the contours into a 3D shape that represents the whole erosion. The volume of the erosion can be determined using blocked and connected construction methods. A visual representation of a cross section through the volume rendered by both methods is compared in figure 4.7.

Blocked construction is equivalent to counting the total number of voxels which contain the erosion and multiplying by the volume of a voxel. This method of

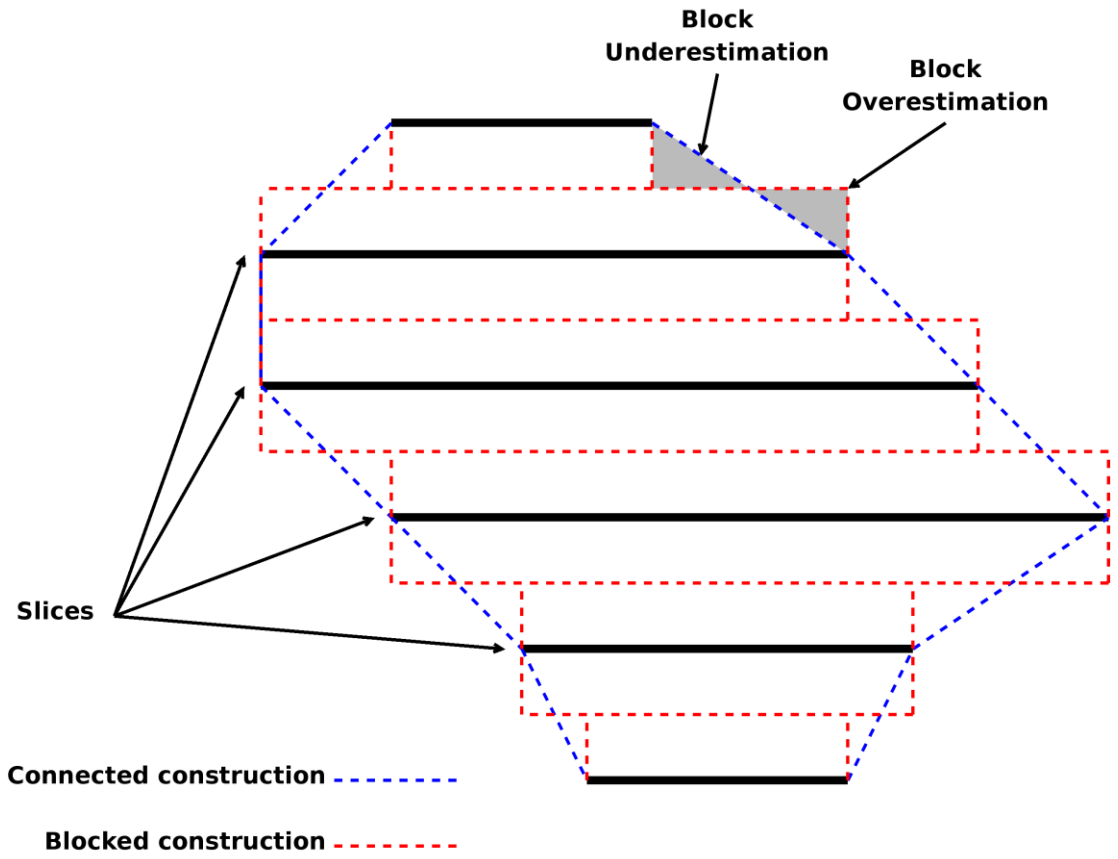

Figure 4.7: A cross-section of a reconstruction of an arbitrary shape based on 2D contours in a series of slices. Thick black lines represent the shape contours and the dotted red and blue lines represent the blocked and connected constructions, respectively. Note how the two methods result in similar volumes because of the cancellation of over- and under-estimation caused by the blocked construction.

reconstruction is determined by multiplying the cross-sectional area contained within each contour by the slice thickness:

$$V = t\left[\frac{A_1}{2} + \sum_{s=2}^{n-1} A_s + \frac{A_n}{2}\right] \tag{4.3}$$

where t is the slice thickness, A_i is the area enclosed by the contour in the i^{th} slice of the segmentation and n is the total number of slices in the segmentation. The first and last slices in the segmentation are multiplied by half the slice thickness to account for partial volume averaging. The result is represented by red dotted lines in figure 4.7.

Connected construction produces a smoother, less block-like reconstruction of erosions by drawing direct lines from the edges of adjacent contours. An approximation of this method is represented by the blue dotted lines in figure 4.7. Though this method might better approximate the actual volume of erosions, it has its disadvantages. Specifically, an algorithm must be used to connect consecutive contours using polygons. Such algorithms are only accurate for simple shapes without many complex curves or splits (erosions with two contours on a single slice). Since erosions may not always have simple shapes this is an undesirable technique. However, the two methods result in similar volume measurements because the block-like reconstruction tends to cancel out the effect of "extra" volume and "missed" volume as shown in figure 4.7 by gray triangles.

4.5.2 Estimating Error

Assuming that erosions are relatively spherical in shape we can determine the theoretical uncertainty associated with determining erosion volume by blocked reconstruction. Since spheres are the closest simple geometric shape approximating erosions, the uncertainty of voxelization of spheres can be determined as an estimate of the uncertainty associated with voxelization of erosions. The uncertainty associated with the voxelization of any object depends on the tessellation of the Euclidean plane containing that object. In many medical images, Euclidean space is tessellated into a regular grid. Specifically, all space is filled by rectilinear parallelepipeds, called voxels, where the width, breadth and height of each voxel is identical to all other voxels as depicted in figure 4.8. If Δx, Δy and Δz are defined as the width, breadth and height of all voxels, respectively, then the volume of a voxel is:

$$v = \Delta x \Delta y \Delta z \tag{4.4}$$

then voxelization of any object is a process wherein all voxels are determined to either be inside or outside the object defined by an inclusion function $\zeta(\vec{m})$, where $\vec{m}$ is a vector pointing from the image origin to the center of the voxel being tested for inclusion. In the case of a sphere, the inclusion function can be defined by finding the distance from the center of the voxel to the center of the

sphere. If that distance is less than or equal to the radius of the sphere, *r*, then the voxel is inside the sphere, otherwise it is outside. This can be expressed mathematically by the equation:

$$\zeta(\vec{m}) = \begin{cases} 1 & \text{if } |\vec{m} - \vec{c}| \leq r \\ 0 & \text{if } |\vec{m} - \vec{c}| > r \end{cases} \tag{4.5}$$

where $\vec{c}$ is a vector pointing from the image origin to the center of the sphere. A 2D representation of this concept is shown in figure 4.9 using the simplified case of a pixelized circle, which is the two dimensional equivalent to a voxelized sphere. If the pixels in figure 4.9 have a height and width of 1 mm, then the pixelized area would be 12 mm^2. The circle in figure 4.9 has a radius of 1.75 mm, making its true area 9.62 mm^2, a difference of 2.38 mm^2.

In 3D, the volume of a voxelized sphere is the sum of voxels included "inside" the sphere, as defined by the inclusion function, multiplied by the volume of a voxel:

$$V_{voxelized} = v \sum_i \zeta(\vec{r}_i) \tag{4.6}$$

The error caused by the voxelization of the sphere is given by:

$$\varepsilon = \frac{V_{voxelized} - V_{true}}{V_{true}} \tag{4.7}$$

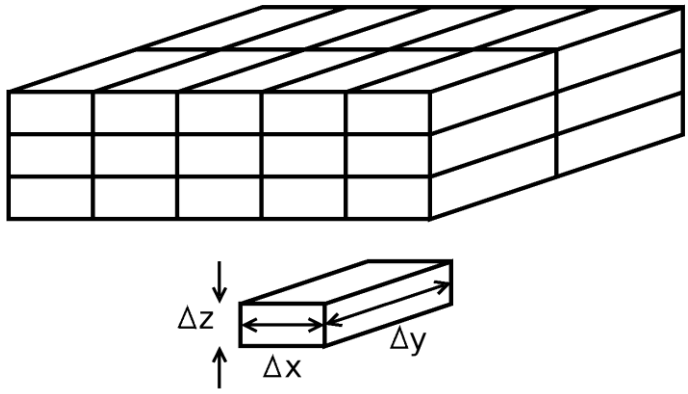

Figure 4.8: A regular grid: a tessellation of the Euclidean plane by rectilinear parallelepipeds which fill all space. In imaging each parallelepiped is called a voxel.

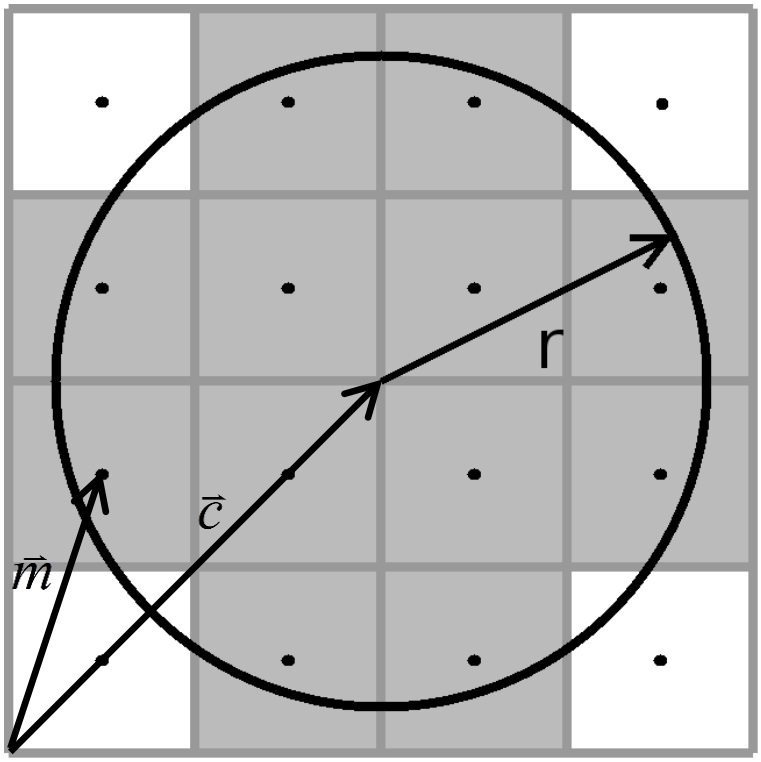

Figure 4.9: A pixelized circle showing the center of each pixel in relation to the circle's diameter. All pixels within the circle are marked gray.

$$\varepsilon = \frac{\Delta x \Delta y \Delta z \sum \zeta(\vec{v}_i)}{4/3\,\pi r^3} - 1 \tag{4.8}$$

If the voxels correspond to an image where the in-plane resolution is isometric and the out-of-plane resolution is *t* times larger than the in-plane resolution[3], then Δx and Δy can be represented by the width *w*, and Δz can be represented by *tw*, simplifying the equation to:

$$\varepsilon = \frac{tw^3 \sum \zeta(\vec{v}_i)}{4/3\,\pi r^3} - 1 \tag{4.9}$$

Since voxel width and the size of the sphere are arbitrary, we can simplify further to the following equation:

$$\varepsilon = \frac{3t}{4\pi\sigma^3} \sum \zeta(\vec{v}_i) - 1 \tag{4.10}$$

where σ is the ratio of sphere radius, *r*, to voxel width, *w*:

$$\sigma = \frac{r}{w} \tag{4.11}$$

The numerical solution to equation 4.10 with respect to σ is plotted in figure 4.10 for t = 3.5. The relationship between ε and σ is not straight forward. The

[3] Most clinical MR images have slice thicknesses 4 to 20 times the width of an in-plane voxel.

maximum error is periodic, so to approximate the uncertainty as a function of σ an exponential trend line has been determined using least squares fitting on the maximum error points. The resulting exponential trend line is:

$$\varepsilon = 2.10\sigma^{-1.74} \tag{4.12}$$

where the four maximum data points used to determine the trend line are indicated by small circles.

An important feature to draw from the uncertainties approximated in figure 4.10 is that for near-spherical erosions, the uncertainty caused by voxelization quickly grows beyond 10% if the erosion is smaller than 12 voxels wide. This theoretical limit is independent of the SNR and depends only on voxel size which is determined by the field of view, imaging matrix and slice thickness.

4.5.3 Voxel Dimensions

For MR imaging of RA, out-of-plane resolution slice thickness is usually substantially lower than in-plane resolution. For example, nearly all of the protocols in the survey of MR scanners and configurations used in RA studies listed in tables 2.1 and 2.2 have a slice thickness several times larger than in-plane pixel dimensions. Typically slice thicknesses range from 1.0 to 5.0 mm whereas pixel dimensions are usually less than 1.0 mm. The resulting non-isotropic voxels are elongated, sometimes 5 to 10 times longer in the out-of-plane than in-plane

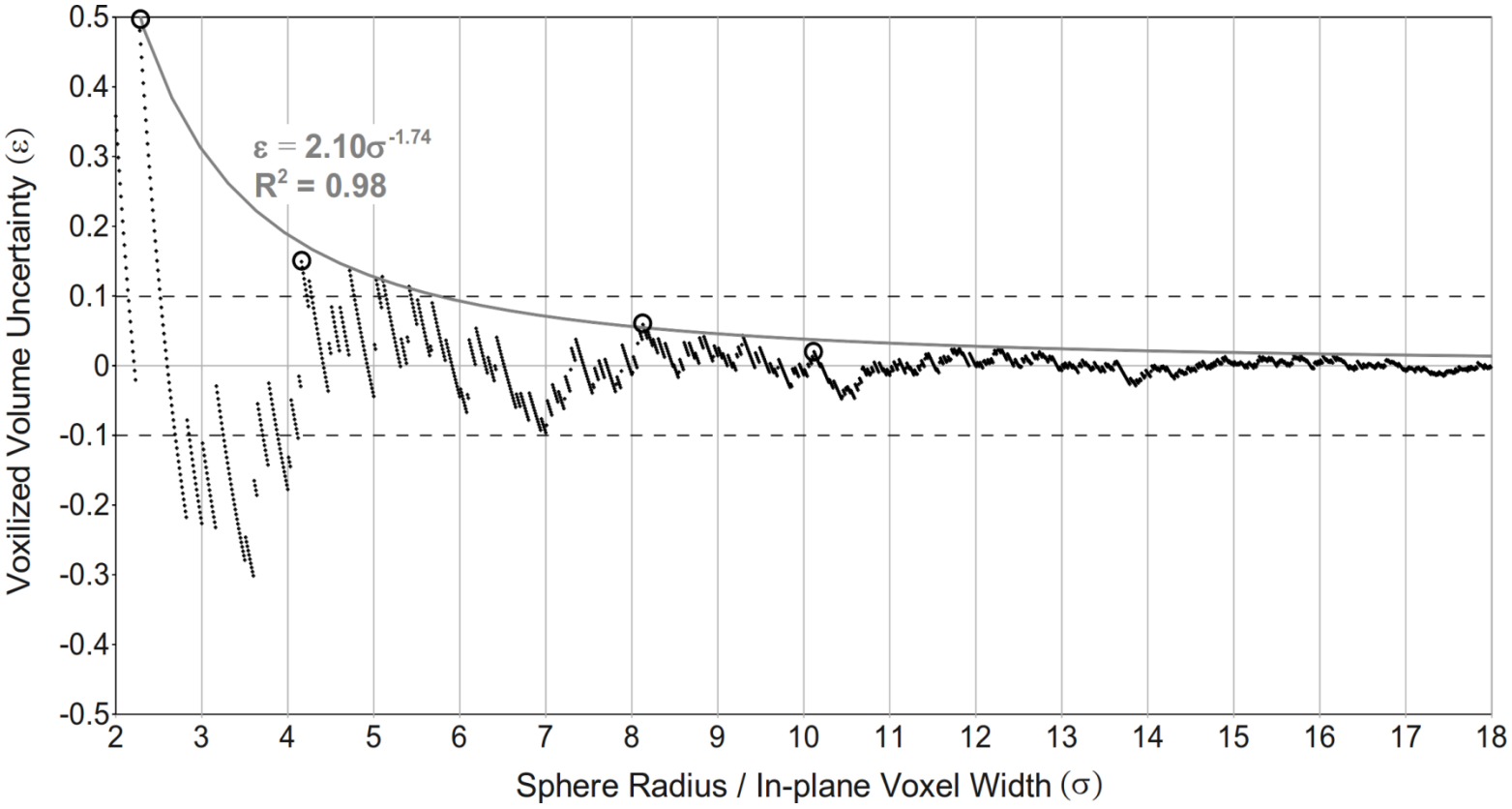

Figure 4.10: A plot of how the ratio of sphere diameter to voxel width affects the voxelized volume measurement error for t = 3.5. A trend line has been fit to the points with greatest uncertainty. The trend was fit using four points indicated by circles.

direction. The cost of thinner MR slices is decreased SNR. There is a direct proportionality between voxel size and SNR, therefore reducing slice thickness without increasing in-plane resolution comes at the cost of lower SNR, which can be offset by increasing imaging time.

In an attempt to overcome this restriction a method was developed to decrease slice thickness (and voxel size) without decreasing SNR at the cost of increased scan time. By scanning a volume twice but offsetting the two scans by half of the slice thickness it is possible to reconstruct the two scans into a single image with half the slice thickness by interlacing the two images. This concept is illustrated in figure 4.11.

The two images are combined by interlacing slices and redefining their slice thicknesses to half their original value. For example, take two image sets, *A* and *B,* each with slice thicknesses *t* where image set *B* is offset by *t/2* from image set *A* in the out-of-plane direction (the in-plane positioning of *A* and *B* are identical). If slices in image set *A* are represented by A_1, A_2, etc, and slices in image set *B* are similarly represented by B_2, B_2, etc, then a third image set, *C*, can be reconstructed with twice as many slices each with a thickness of *t/2* by interlacing image sets *A* and *B* such that the slices in image set *C* are A_1, B_1, A_2, B_2, A_3, B_3, etc.

An example of this technique is shown in figure 4.12. The interlaced image displayed in (b) is clearly smoother than the non-interlaced image in (a), but the

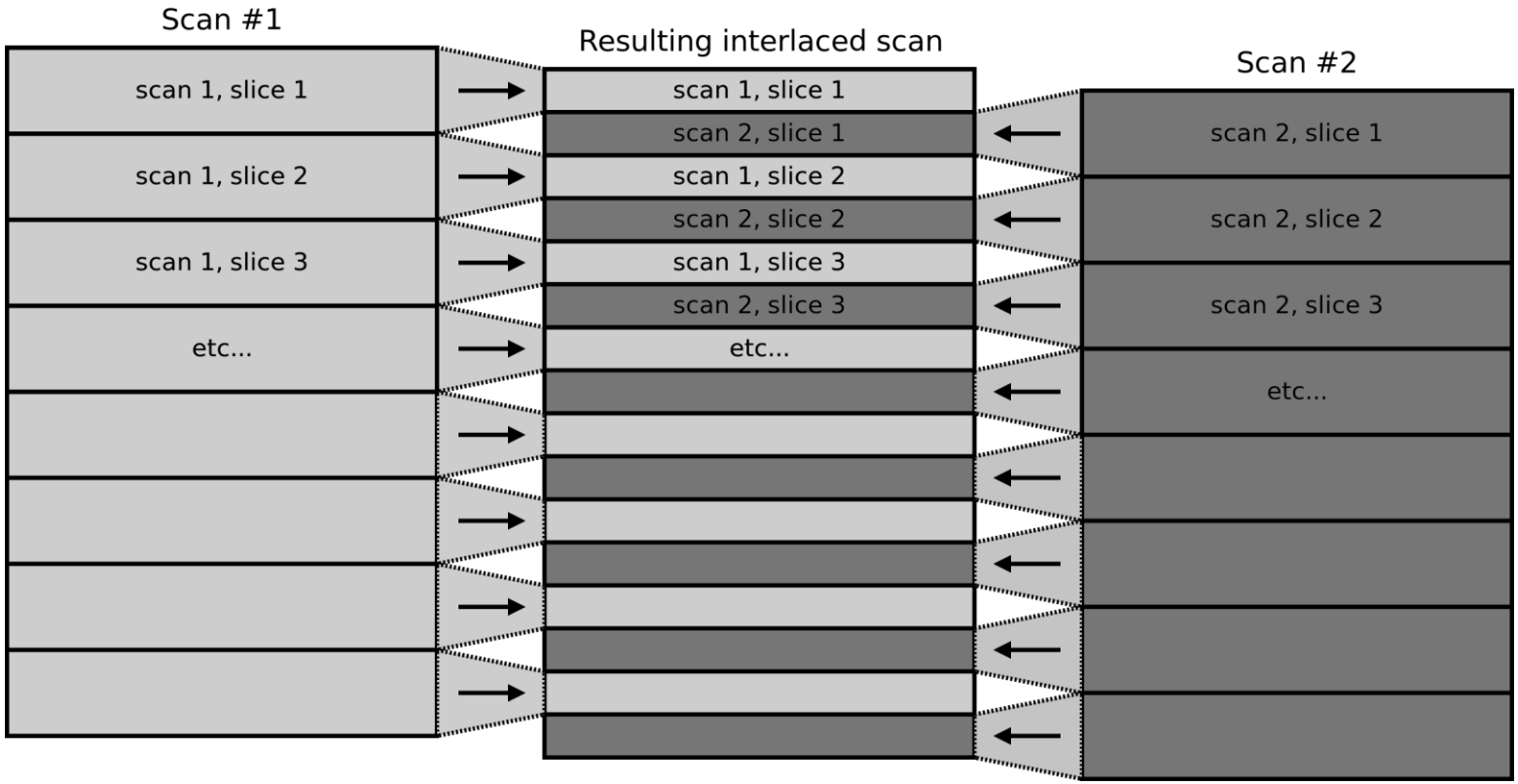

Figure 4.11: A schematic illustrating how interleaving the slices of two images offset by half the slice thickness can be used to create a third image with half the slice thickness.

SNR in both images is equivalent. A major limitation of this technique is participant motion. Because the two regular images used to create the interlaced image are taken consecutively and the scan time is double that of a single scan the technique is highly sensitive to movement. Figure 4.13(a) shows an example of an interlaced image constructed by two images which were taken consecutively where the participant moved slightly between acquisitions. The two un-interlaced images do not appear to have any movement artifact but when combined there is an obvious misalignment. Furthermore, scanning was performed with the use of an orthopedic brace in order to reduce patricipant motion. The brace, depicted in figure 4.14, was made of soft nylon and straps which holds in place rigid plastic along the anterior and posterior hand and wrist in order to restrict movement in the radiocarpal and metacarpophalangeal joints. Figure 4.13(b) shows the interlaced image resulting from scans acquired with the brace. Linear image registration was performed on both sets of images.

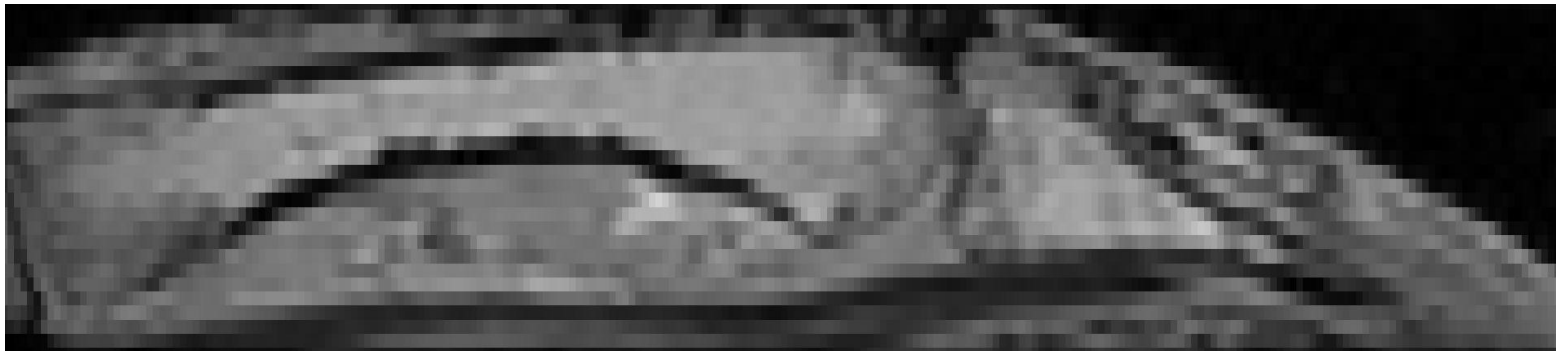

(a) Regular, non-interlaced image

(b) Interlaced image

Figure 4.12: Two axial slices of a stack of coronal images of a cadavaric hand. The top image is a non-interlaced, regular scan with a slice thickness of 1.0 mm. The bottom image is an interlaced scan produced using two images with a slice thickness of 1.0 mm each, artificially producing a slice thickness of 0.5 mm.

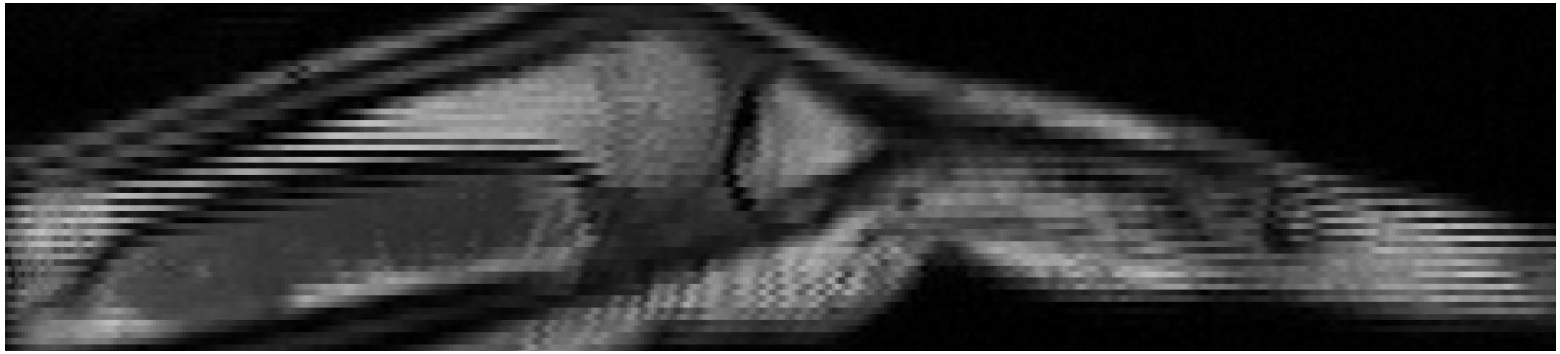

(a) Interlaced image without a brace

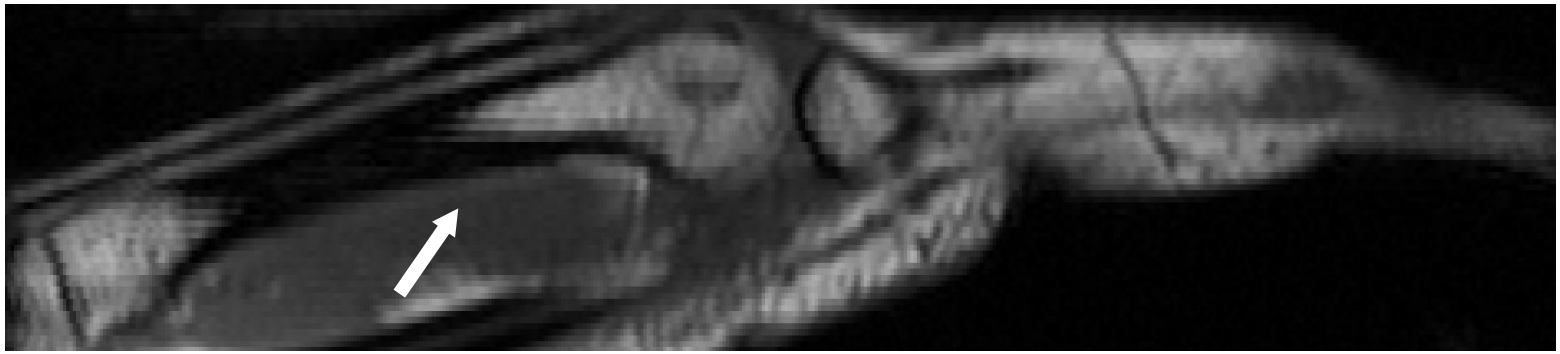

(b) Interlaced image with a brace

Figure 4.13: Two axial slices of a stack of interlaced coronal images of a participant's hand. The top image, which was scanned without the use of a hand/wrist brace, shows a striping effect caused by misalignment between the two images. The bottom image, which was scanned with the participant's hand in an orthopedic brace, shows substantially less misalignment than the top image, but striping is still evident (see the bands pointed to by the white arrow).

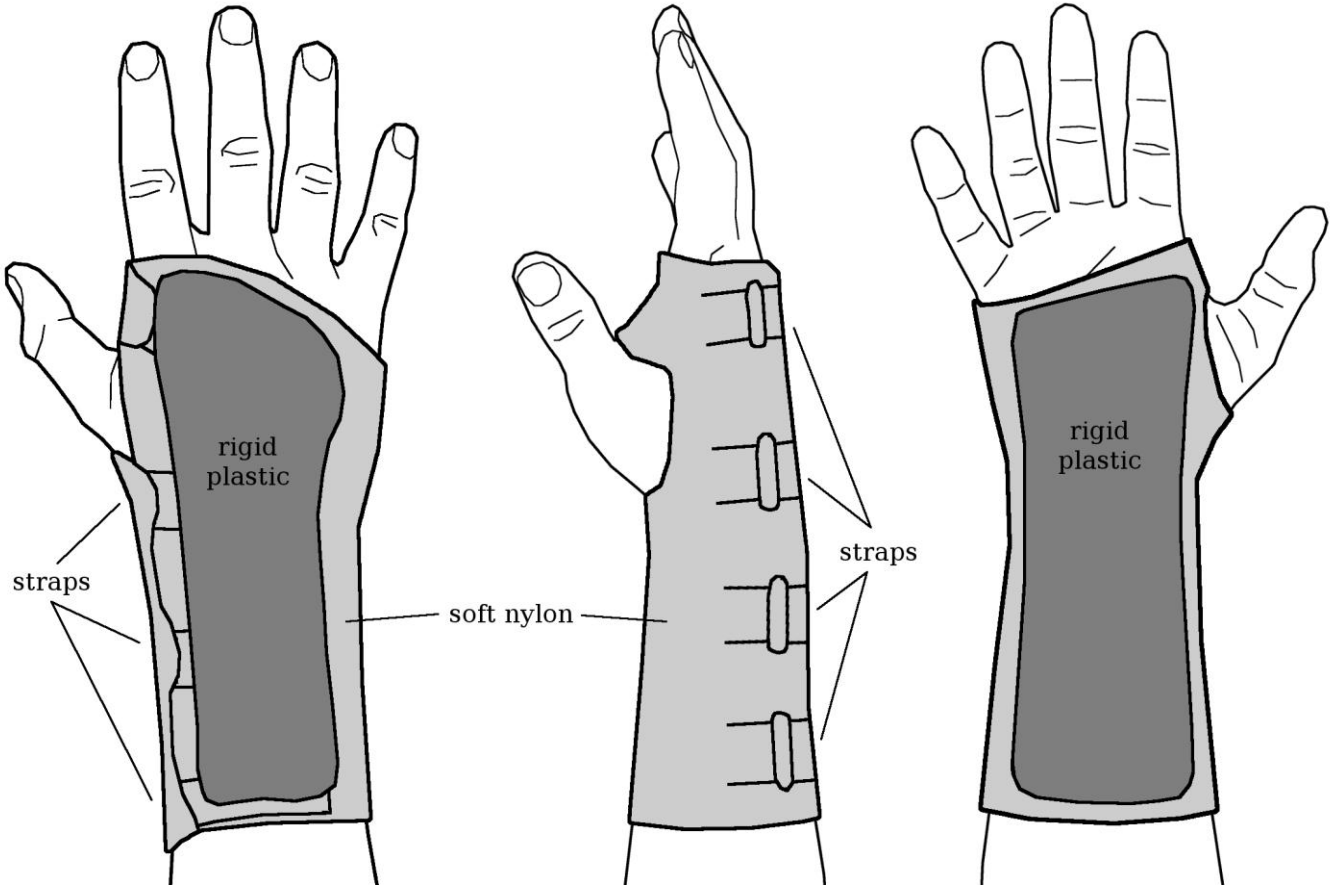

Figure 4.14: A depiction of the brace used to reduce the movement-like artifact when interlacing two consecutive images. The brace is made of soft nylon and straps which holds in place rigid plastic along the anterior and posterior hand and wrist in order to restrict movement in the radiocarpal and metacarpophalangeal joints.

Chapter 5

Clinical Validation

5.1 Participants

All use of human participants was approved by the McMaster University Ethics Board and informed consent was obtained from all participants prior to recruitment. Contraindication to MR imaging was assessed by a standard questionnaire. Over the course of 14 months a total of 234 participants from 5 rheumatology clinics were imaged. All participants were identified as having RA according to the American Rheumatism Association 1987 revised criteria for the classification of rheumatoid arthritis (Arnett et al., 1988). A subset of images containing at least one erosion appropriate for volume measurement was identified by visually inspecting the initial 234 participant scans. Erosions were considered to be candidates for bone erosion measurement if they were located in the 2nd to 5th metacarpal heads, visible on at least three consecutive 1 mm thick slices and occupied less than half the size of the metacarpal head. Erosions larger than this are not usually associated with early active disease and are of less clinical interest since substantial irreversible damage has already occurred. This resulted in a total of 34 erosions which were identified in 32 participants (two participants had two distinct erosions in the same MR image). The age of these participants ranged from 35 to 81 years old, with 23 female and 9 male participants.

5.2 Statistics

Statistical analysis was performed using Statistical Package for the Social Sciences for Windows, version 14.0 (SPSS, Chicago, IL, USA). Intra-rater and inter-rater reproducibility was calculated as the Intraclass Correlation Coefficient (ICC) using a two-way mixed effects model with absolute agreement followed by the 95% confidence intervals in brackets. A Bland-Altman difference plot (Bland and Altman 1986) was performed to compare the manual and automated volume measurements.

5.3 Reproducibility

Using the same test-cohort of 8 participants used to constrain parameter values described in section 4.3.1 (distinct from the analysis cohort described in the previous section), three raters were trained to segment erosions manually and by using the automated algorithm. Rater 1 was trained by a musculoskeletal (MSK) radiologist to segment erosions in MR images, while raters 2 and 3 were not. Manual segmentation of erosions required each rater to trace the boundaries between the erosion and surrounding tissue using a computer mouse in every slice that the erosion occupied. Three tests of the hybrid segmentation algorithm were performed.

The first test determined whether the inter- and intra-rater reproducibility of volume measurement using the automated algorithm was at least as good as that obtained by manual measurement. To assess inter-rater reproducibility, all erosion volumes were measured by all three raters using the automated and manual techniques. To assess intra-rater reproducibility, all measurements were repeated twice by a single rater, at least 72 hours apart.

The second test determined the accuracy of the automated segmentation measurements. To determine the accuracy, the manual tracings performed by rater 1 were checked and, if necessary, corrected by a MSK radiologist and used as a gold-standard. The use of manual tracing by a radiologist as a gold-standard for the purpose of validating segmentation algorithms is used routinely. For example, algorithms for the measurement of joint space in the hand (Duryea et al 2000a), knee (Duryea et al 200b) and hip (Gordon et al 2001) were developed and validated using hand-drawn joint margins.

Finally, the third test determined whether there was any significant difference between the time needed to measure the volume of an erosion using the automated and manual techniques. For this purpose, each of the three raters recorded the time required to segment each erosion using both the manual and automated measurement techniques. Figure 5.1 summarizes the reproducibility of the

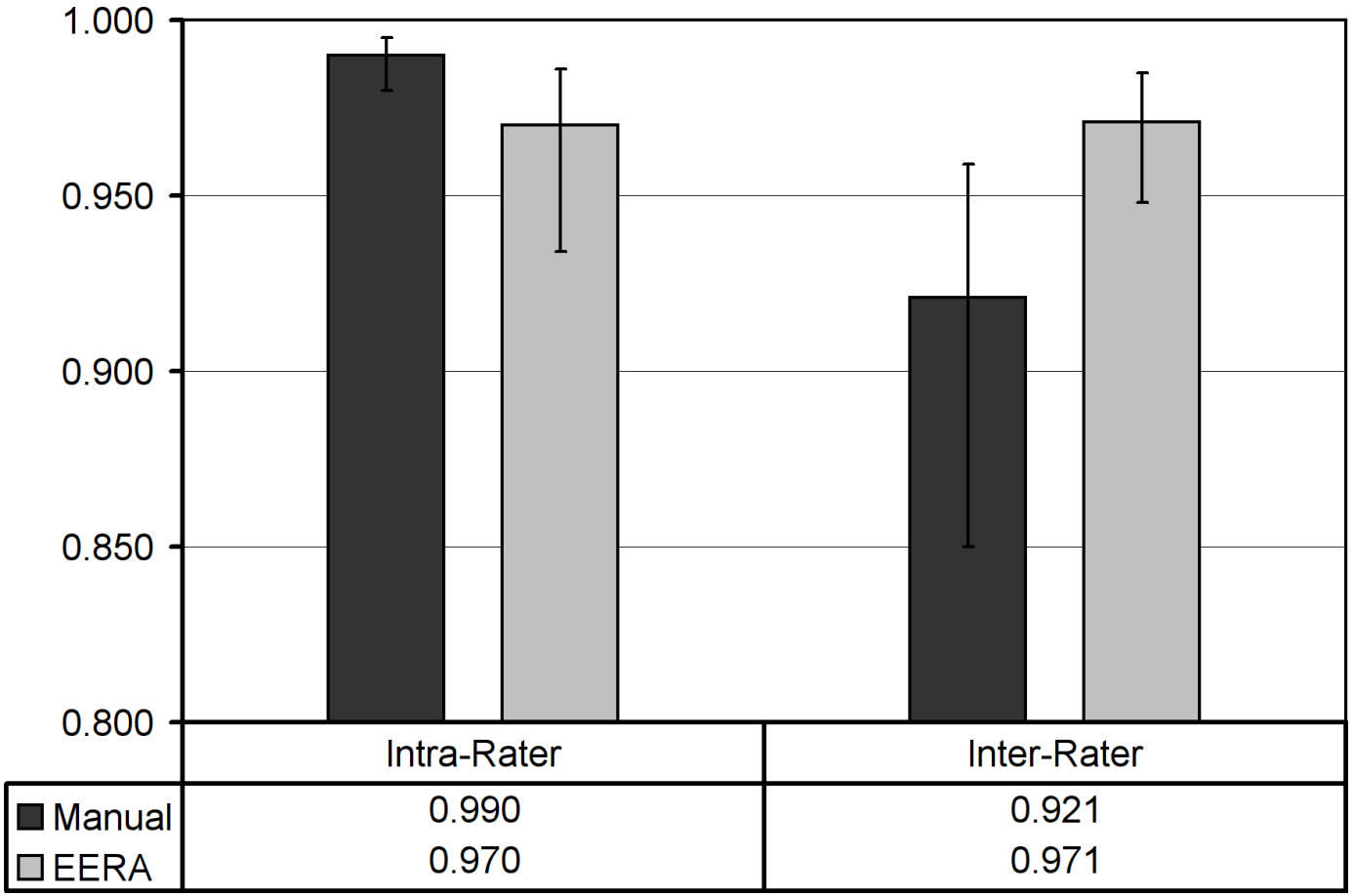

Figure 5.1: The reproducibility of manual and automated methods for measurement of bone erosion volume expressed as Intraclass Correlation Coefficients (ICCs). The error bars represent 95% confidence intervals.

manual and automated volume measurements. The ICCs for manual and automated measurements showed very high precision (> 0.9) with no significant difference between the two techniques for both intra- or inter-rater reproducibility. However, it is notable that though there is a significant difference between the intra- and inter-rater reproducibility of the manual technique, there is no such difference in the automated technique.

5.4 Accuracy

The binary volume overlap between manual and automated segmentation was measured by dividing the total number of voxels in the intersection of both segmentations by the total number of voxels in the manual segmentation:

$$\gamma = \frac{\sum_{voxels} S_a \cap S_m}{\sum_{voxels} S_m} \tag{5.1}$$

where S_a is the automated segmentation and S_m is the manual segmentation. The mean value for γ was 0.79 ± 0.12. A plot of automated versus manual volume measurement is provided in figure 5.2 along with the least squares fit through the data. The accuracies of all manually defined contours were confirmed by a MSK radiologist. The plot shows high agreement between the automated and manual measurement with an R^2 value of 0.923. The slope of the fitted line is 1.030 with an x-intercept of 1.385 mm^3, indicating that the automated volume measurement

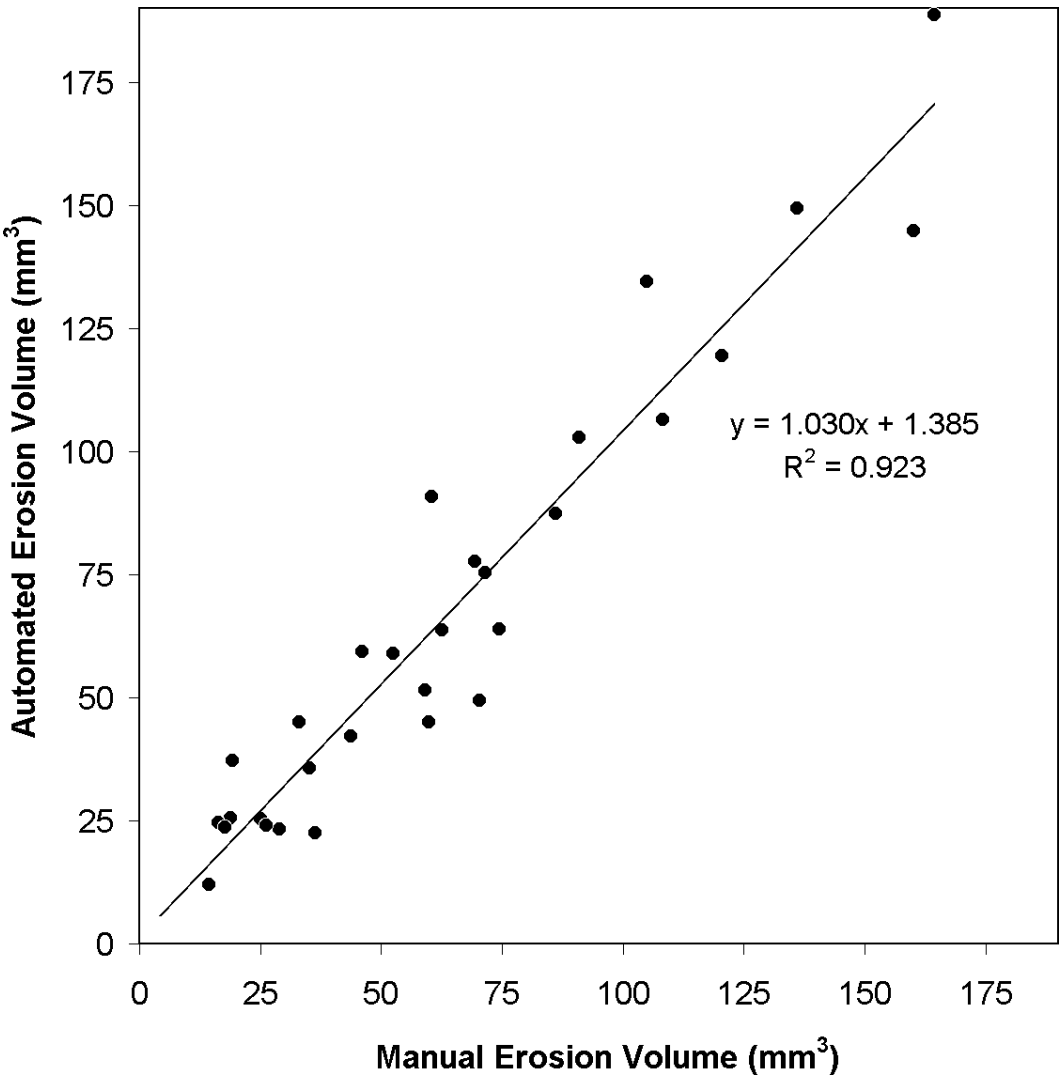

Figure 5.2: A plot of the automated versus gold-standard manual erosion volume measurements along with the least squares fit.

agreed with manual tracing over a large range of erosion sizes. The mean and standard deviation of the absolute difference between the automated and manual volume measurements were 12.25 mm^3 and 13.90 mm^3, which is depicted graphically in the Bland-Altman difference plot of figure 5.3. There are an equal number of points above and below the x-axis, suggesting that the automated measurements did not over- or underestimate the gold-standard segmentations.

5.5 Parameter Sets

Table 5.1 outlines the frequency with which each of the five controlling parameters resulted in a successful segmentation of the erosions. As listed, in roughly 45% of the cases, the default controlling parameter successfully defined the boundaries of the erosions. For those segmentations that failed using the default parameters (A), an additional 25 to 40% of the cases could be correctly segmented if the rater proceeded to re-segment with parameters controlled by choices B or C.

5.6 Segmentation Time

Table 5.2 compares the average time taken to measure an erosion between the automated and manual procedures. The averages are also listed for erosions above and below a volume of 100 mm^3 since manual tracings are influenced by erosion size. In each erosion size category the automated measurements took

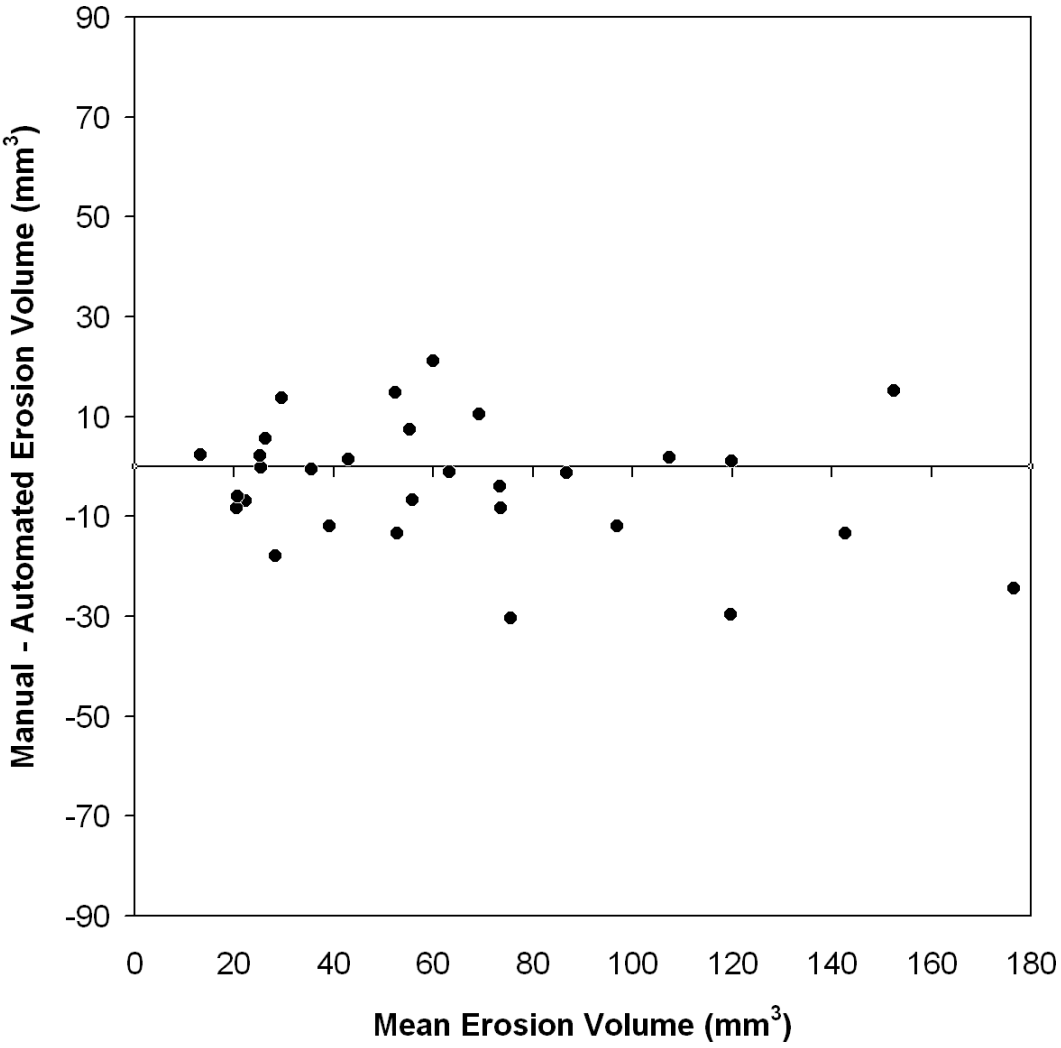

Figure 5.3: A Bland-Altman difference plot comparing the automated and gold-standard manual erosion volume measurements. Note that there is an even number of points above and below the x-axis.

Table 5.1: The frequency with which the parameters were used by the three raters. Note that the first parameter, A, successfully segmented the erosion without rater intervention in 45.5% of erosions measured.

	A	**B**	**C**	**D**	**E**
Rater 1	13 (43.8%)	8 (26.7%)	4 (13.3%)	1 (3.3%)	4 (13.3%)
Rater 2	14 (46.7%)	5 (16.7%)	4 (13.3%)	1 (3.3%)	6 (20.0%)
Rater 3	14 (46.7%)	5 (16.7%)	3 (10.0%)	1 (3.3%)	7 (23.3%)

Table 5.2: The average (standard deviation) time taken to score a single erosion in minutes.

Volumes (mm^3)	**Manual Tracing**	**Hybrid Algorithm**	**P-value**
All	7.8 (4.5)	2.6 (1.7)	< 0.0005
< 100	5.1 (2.6)	2.2 (1.4)	< 0.0005
> 100	12.6 (2.9)	3.3 (1.8)	< 0.0005

significantly less time ($p < 0.0005$) than the corresponding manual tracing which took an average of 2 to 4 times longer.

5.7 Algorihtm failure rate

The hybrid algorithm failed to segment the same 4 of 34 erosions for each of the three raters. Two examples of erosions which the algorithm failed to segment are shown in figure 5.4. Small changes to the position of the seed point caused substantial variability in the final volume measurement. To minimize the variability of the erosion volumes determined with the algorithm, users were restricted to placing a single seed point in the central image slice of each erosion. Restriction to one seed point can result in algorithm failures for very large erosions. This was the case for two of the four failed measurements. These erosions occupied a large portion of the metacarpal head as they appeared to be made up of two or more smaller erosions that had grown large enough to combine into one erosion (as is the case with the erosion in figure 5.4(a) pointed to by the white arrow).

The remaining two failed measurements highlighted an additional limitation of the hybrid segmentation algorithm. The algorithm failed to segment erosions which had large openings in the cortical bone (as is the case with the erosion in figure 5.4(b) pointed to by the gray arrow). One of the advantages of using a boundary-based algorithm, such as LS, as part of the hybrid algorithm is that it is

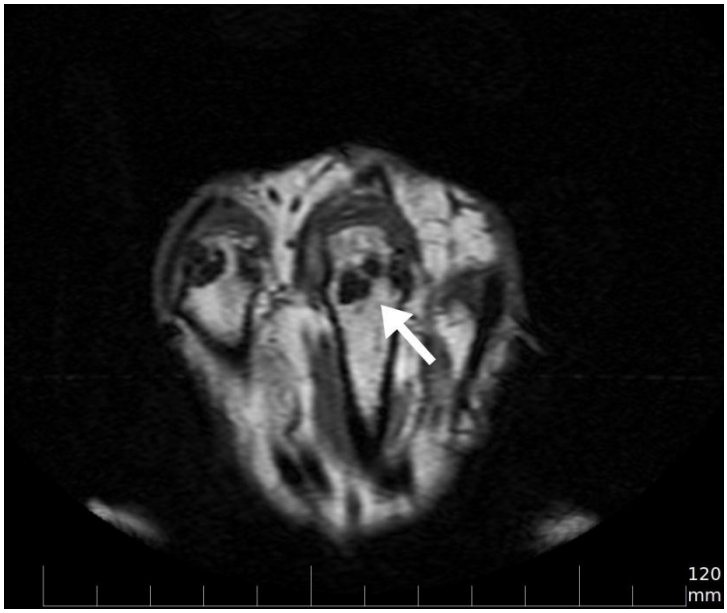

(a) A larger erosion formed by two smaller erosions joining together

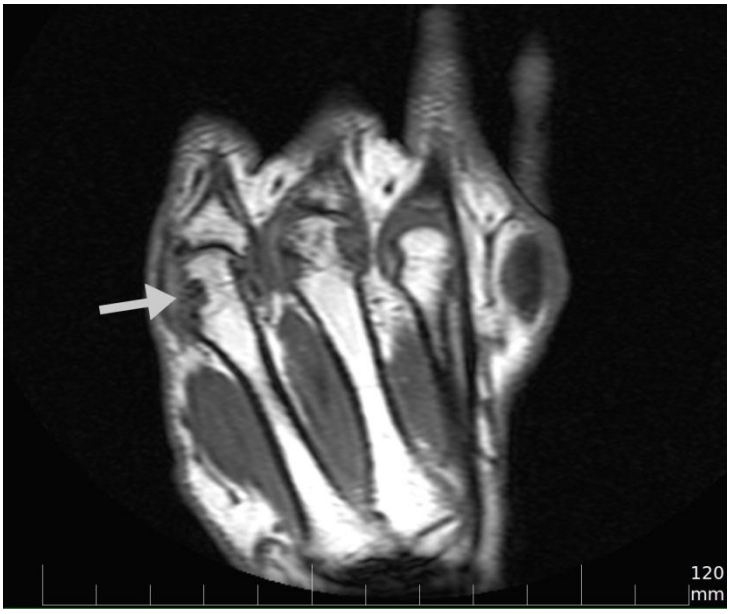

(b) An erosion with a large portion of eroded cortical bone

Figure 5.4: Two examples of erosions that the hybrid segmentation algorithm failed to segment. In this context a failed segmentation is defined as a failure of all five parameter sets to satisfactorily contour the erosion in each of the slices in which it appears.

able to detect boundaries even if they are fuzzy or not fully visible. For example, the LS algorithm was able to accurately contour erosions even when they had small openings in the cortical bone. Large openings pose a much more challenging segmentation problem as there is little to no boundary between the erosion within the bone and the synovium outside the bone. This type of change to the bone due to RA is more indicative of advanced disease, and thereby less clinically relevant for treatment interventions.

Chapter 6

Follow-up Data

6.1 Participants

Of the 32 participants of the main cohort described in section 4.5, 14 participants were scanned a second time approximately 9 months after their baseline scan. Two of the 14 participants had two erosions and the remaining had one for a total of 16 erosions included in the study. Participant ages ranged from 35 to 81 years old, with 13 female and 3 male participants. All but two participants were prescribed the disease modifying antirheumatic drug methotrexate, five of which were also treated with a biologic.

6.2 Methods

All follow-up subject images were visually inspected for scan quality and compared with baseline images to verify that the scan coverage matched that from baseline. All follow-up images passed this quality assurance check. The manual and automated segmentations were then performed by an untrained reader. This reader was one of the two that analyzed the baseline images (section 5.3). The manual tracings were performed with the baseline manual tracings displayed side-by-side for reference. One week after the follow-up images were manually traced the erosions were segmented using the automated algorithm. The automated segmentations were also performed with results of the baseline automated segmentations also displayed side-by-side for reference. It is important to note that the baseline automated segmentations were not displayed while performing

the manual segmentations, nor were the baseline manual segmentations displayed while performing the automated segmentations.

6.3 Minimal Detectable Change

To estimate the minimal detectable change of erosion volume from serial images, the theoretical error caused by partial volume measurement, as described in chapter 4, is considered. Given that the voxel size in this study was $0.27\times0.27\times1.0$ mm^3 (out-of-plane voxel size is 3.7 times larger than in-plane voxel width) and assuming that erosions are approximately spherical in shape, the uncertainty of an erosion due to partial volume effect as a function of erosion size can be estimated using equation 4.13. Table 6.1 lists the volume, diameter and error determined from partial volume measurement of large, medium and small erosions ranging from 150 to 15 mm^3. Figures 4.4, 4.5 and 4.6 depict 3D renderings of these erosion sizes, respectively. The minimum detectable change may be estimated to be at least the size of the largest error (in volume) for the full range of measurable erosion sizes. This results in a minimum detectable change to be approximately 4.1 mm^3.

6.4 Results

The hybrid algorithm successfully segmented all 16 follow-up erosions resulting in a 0% failure rate. A summary of the age, treatment and volumes of erosions at

Table 6.1: The volume, diameter and estimated uncertainty due to partial volume effect of a small, medium and large erosion (relative to the range of erosion sizes measured in chapter 5). The estimated error was determined using equation 4.13.

	Volume (mm^3)	**Diameter (mm)**	**Partial Volume Error (%)**	**Partial Volume Error (mm^3)**
Small	15	3.06	10.3	1.5
Medium	80	5.35	3.9	3.1
Large	150	6.59	2.7	4.1

baseline and follow-up as measured by manual and automated segmentation is provided in table 6.2. A plot of the difference between baseline and follow-up volumes as determined by automated and manual measurement is provided in figure 6.1 along with the least squares fit through the data. The plot shows high agreement between the automated and manual measurement differences with an R^2 value of 0.931. The slope of the fitted line is 0.931 with an x-intercept of -1.820 mm^3, indicating that the automated volume measurement agreed with manual tracing over all ranges of erosion volume change between baseline and follow-up scans.

A Bland-Altman plot of the manual vs. automated erosion volume differences is shown in figure 6.2. There are 6 points below and 10 above the x-axis, suggesting that automatic segmentation may underestimate the change in erosion size when compared to manual tracing. However, the differences between manual and automatic segmentation determined volume change were all very small; falling between -12 mm^3 and 15 mm^3. The baseline and follow-up MR images of participants #12 and #4 are shown in figures 6.3 and 6.4, respectively. Each figure shows the automated segmentation as a thick white line on a single MR slice for both baseline and follow-up.

Table 6.2: A summary of the age, treatment and volumes of erosions at baseline and follow-up as measured by manual and automated segmentation. All participants except for numbers 3 and 4 were being treated with methotrexate along with the additional treatment listed in the third column (if any).

Participant (gender)	Age	Additional Treatment	Basline Volume (mm^3) manual/auto	Follow-Up Volume (mm^3) manual/auto	Change in Volume (mm^3) manual/auto
1 (F)	64	Folic acid	18.8 / 25.6	25.5 / 20.8	6.7 / -4.8
2 (M)	46	Leflunomide	120.4 / 119.3	142.3 / 145.9	21.9 / 26.6
			25.1 / 25.4	35.3 / 36.4	10.2 / 11.0
3 (M)	79	None	52.4 / 59.0	27.7 / 20.2	-24.8 / -38.8
4 (M)	72	None	29.0 / 23.4	30.7 / 25.8	1.7 / 2.4
			13.5 / 16.5	74.6 / 74.5	61.1 / 58.0
5 (F)	65	None	16.3 / 24.6	58.0 / 57.1	41.7 / 32.5
6 (F)	54	Etanercept	26.3 / 24.1	19.1 / 16.3	-7.2 / -7.8
7 (F)	48	Etanercept	43.7 / 42.2	61.9 / 58.9	18.2 / 16.8
8 (F)	41	Leflunomide	149.9 / 145.1	90.1 / 97.4	-59.8 / -47.7
9 (F)	34	Abatacept	21.1 / 28.9	27.7 / 29.2	6.6 / 0.3
10 (F)	61	Folic acid	30.6 / 36.5	37.1 / 38.2	6.5 / 1.8
11 (F)	64	Folic acid	25.12 / 18.5	27.6 / 28.9	2.5 / 10.3
12 (F)	55	Adalimumab	33.9 / 31.9	35.4 / 31.0	1.6 / -0.8
13 (F)	63	Etanercept	35.8 / 36.9	50.7 / 53.2	14.9 / 16.3
14 (F)	51	Leflunomide	37.9 / 38.5	35.5 / 26.1	-2.4 / -12.4

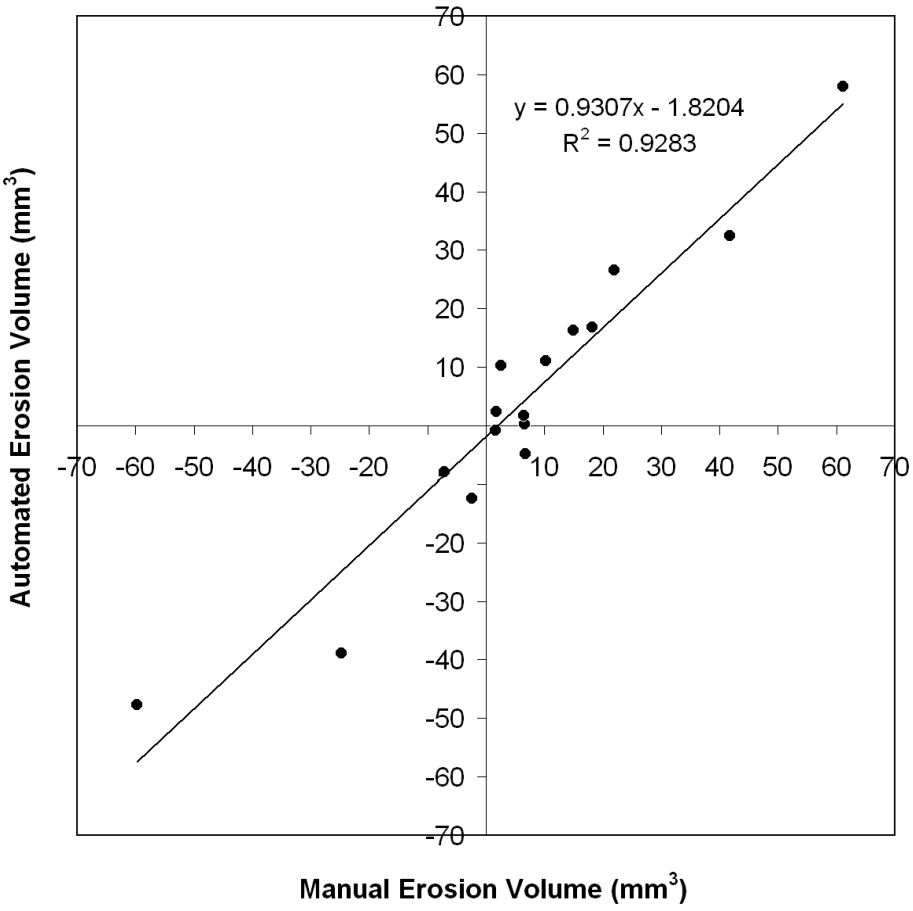

Figure 6.1: A plot of the difference between follow-up and baseline volumes as measured by the automated versus gold-standard manual measurements along with a least squares fit through the data.

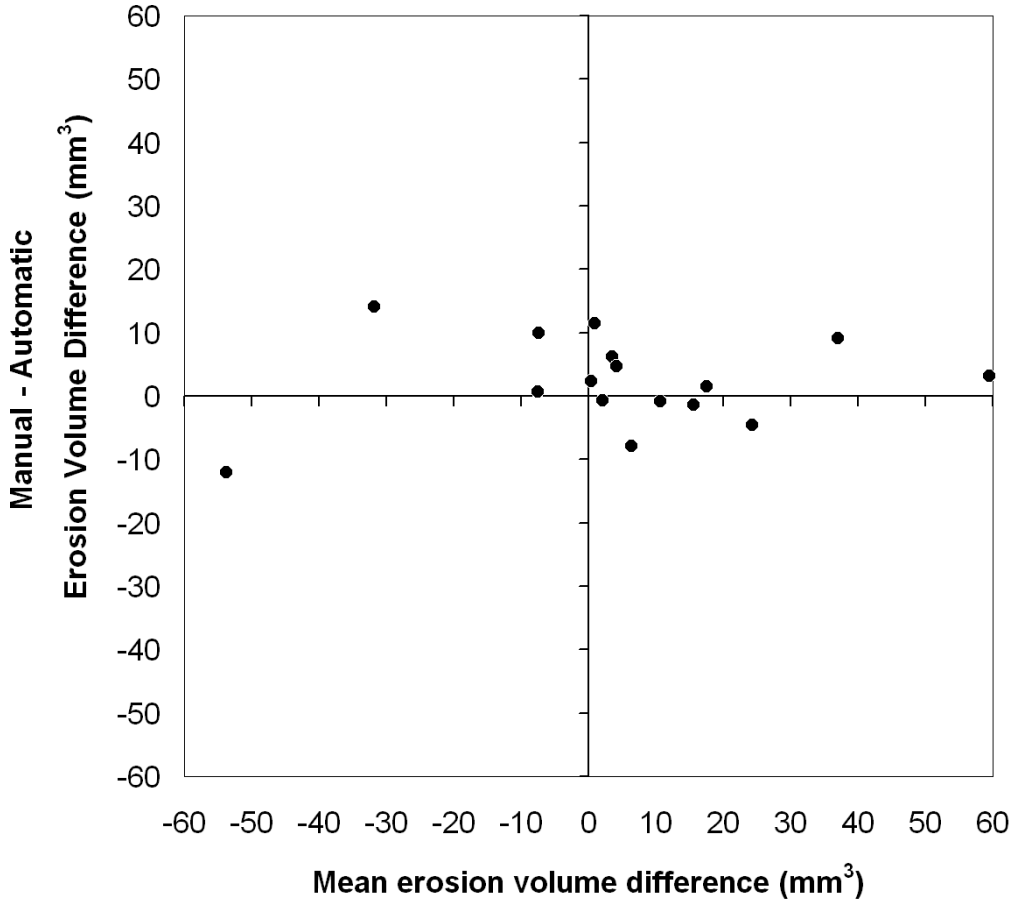

Figure 6.2: A Bland-Altman difference plot comparing the difference between baseline and follow-up volumes determined using the automated and gold-standard manual erosion volume measurements. Note that there are more points above the x-axis than below, suggesting a trend for the automated method to underestimate changes in erosion volume.

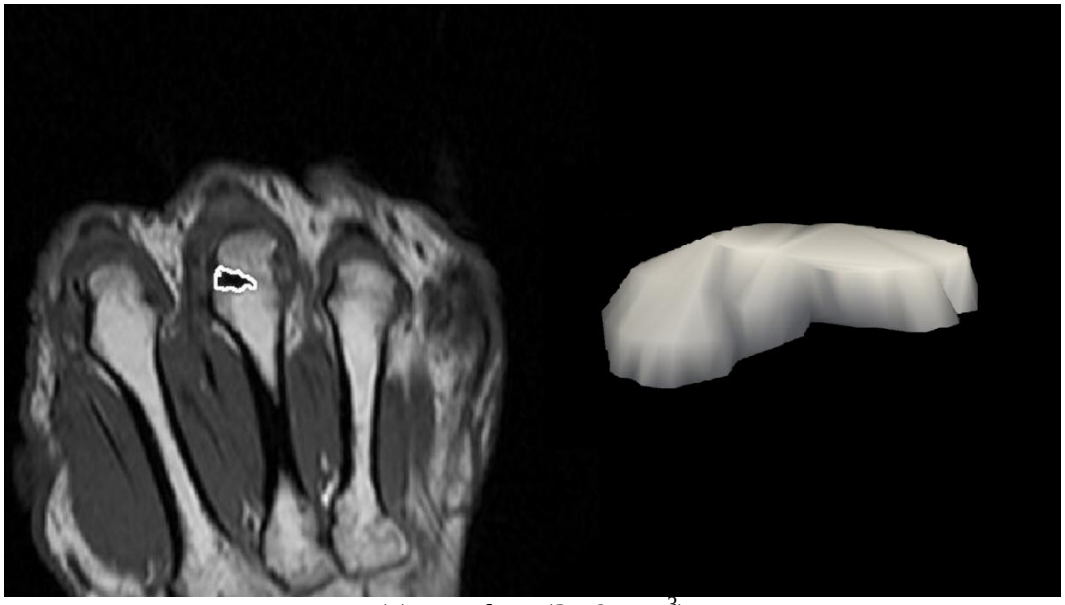

(a) Baseline (31.9 mm^3)

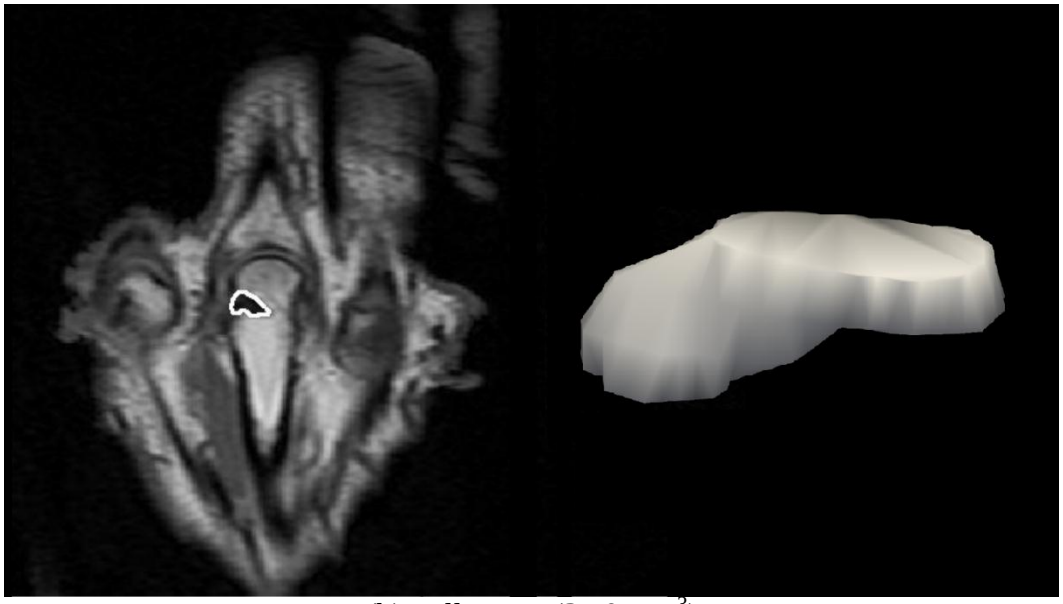

(b) Follow-up (31.0 mm^3)

Figure 6.3: Single MR slices (left) and 3D renderings of erosions (right) of baseline and follow-up images for participant #12. The automated segmentation of the erosion found in the second metacarpal is shown as a thick white line. The erosion volume did not significantly change (decrease of 2.7%).

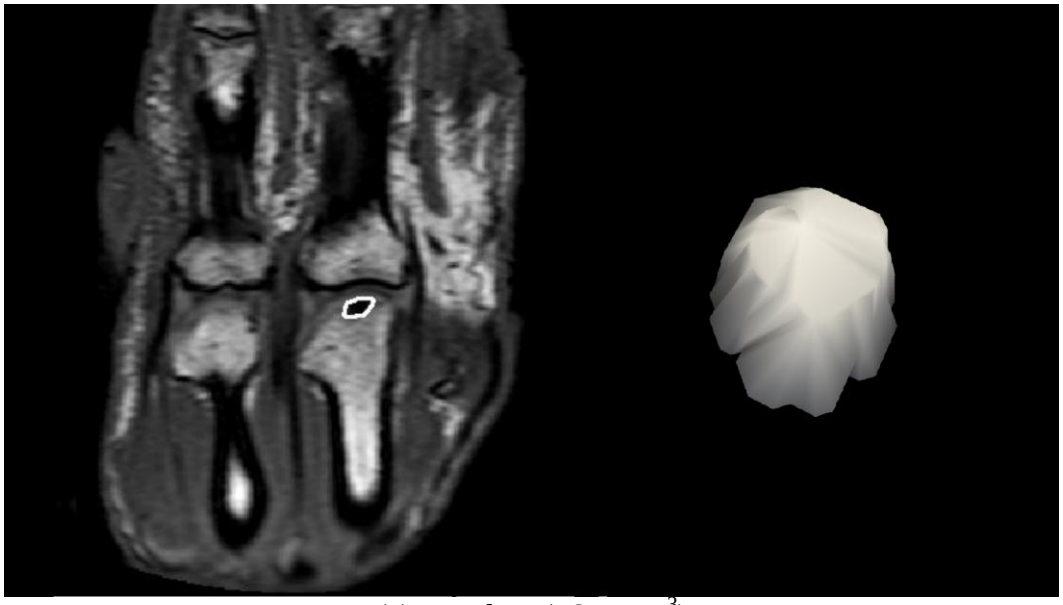

(a) Baseline (16.5 mm^3)

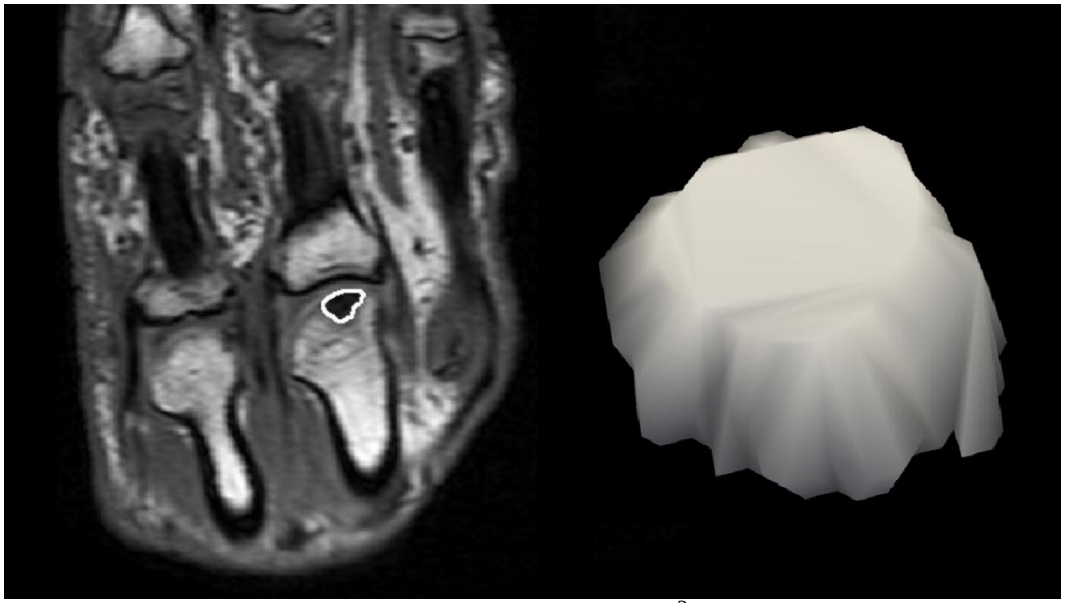

(b) Follow-up (74.5 mm^3)

Figure 6.4: Single MR slices (left) and 3D renderings of erosions (right) of baseline and follow-up images for participant #4. The automated segmentation of the erosion found in the second metacarpal is shown as a thick white line (second erosion). The erosion volume significantly changed (increase of 127.5%).

6.5 Discussion

Of the 16 erosions measured at follow-up, the volumes (as measured by the automated technique) of 10 were smaller than 50 mm^3, 5 between 50 and 100 mm^3 and 1 greater than 100 mm^3 (see table 6.2). This does not evenly represent the range of erosion sizes of baseline erosions. However, the smallest range (50 mm^3 or less) is the most clinically important since they represent subjects whose symptoms indicate an earlier stage of disease.

Chapter 7

Discussion

7.1 Choice of algorithms to hybridize

Manual segmentation of erosions in MR images requires a rater to trace the boundaries between erosion and surrounding tissue using a computer mouse in every slice that the erosion occupies. Some of these boundaries are difficult to interpret causing the border between the erosion and surrounding tissues (bone marrow, cortical bone, cartilage and synovium) to be subjective. Boundary subjectivity can be minimized and a high degree of accuracy in erosion volume measurement achieved if manual tracing is performed by a MSK radiologist. Regardless of the qualification of the rater however, manual tracing is time consuming as every slice containing the erosion must be individually delineated. The goal of automated segmentation is to decrease scoring time while preserving the precision and accuracy of manual tracing as performed by a radiologist.

The hybrid algorithm developed in this thesis eliminates the need for a rater to manually trace boundaries between erosions and surrounding tissues. Instead, boundaries are automatically defined after a single seed point and a set of predefined controlling parameters are chosen by a rater. The strategy adopted in developing the algorithm was to combine the strengths of a region-based segmentation algorithm; region growing-based connected thresholding, with the complimentary strengths of a boundary-based algorithm; level-set based fast marching. In general RG segmentation can delineate the boundary between

erosions and bone marrow with some success, but bleeds outside of the bone at the boundary between the erosion and the synovium (see figure 3.7). The LS algorithm does not delineate the boundary between the erosion and bone marrow as well as the RG algorithm, but it does not bleed outside of the bone. The ability of the LS algorithm to provide a segmentation constrained to lie within the bone boundary was illustrated in figure 3.10. Therefore, combining the strengths of a region-based and boundary-based segmentation algorithm provides a segmentation which clearly delineates the erosion boundaries without bleeding outside of the joint containing the erosion.

The choice of which segmentation algorithms to combine was made based on the effectiveness of each algorithm with respect to the challenges of segmenting bone erosions in MR images. These challenges include the delineation of the boundaries between the characteristic low signal of eroded bone and the low to mid-level signals of other, non-marrow tissues surrounding the erosion such as edema, cortical bone, synovial fluid and cartilage. No algorithm applied alone was found to be effective in identifying the boundary between bone erosion and soft tissue found outside of the bone. Often, these two regions were both characterized by very low signal, resulting in little to no boundary delineaton between where the erosion ends and the surrounding soft-tissue begins. Unlike all of the other algorithms explored, the LS algorithm was able to identify this type of

boundary because LS algorithms do not require threshold values, allowing them to segment features with inhomogeneous intensities. However, the LS algorithm tends to poorly delineate the boundary between bone erosions and marrow. Region growing was chosen to be combined with the LS algorithm since it addressed the major deficiency of the LS algorithm. Unlike the LS algorithm, RG can successfully delineate the boundary between bone erosion and marrow. Unlike least-cost graphing, naïve thresholding and watershed algorithms, however, the RG algorithm is localized (i.e.: able to segment a single feature of interest) and capable of segmenting features which span several image slices. This ability to provide localized segmentation made the RG algorithm a natural fit for hybridization with the LS algorithm for segmenting erosions.

Despite the watershed algorithm's limitation of being non-localized it may also be successful at segmenting bone erosions in MR images if combined with the LS algorithm. Overall the watershed algorithm failed to segment the boundary between erosion and bone marrow as well as the RG algorithm. The watershed algorithm uses the gradient magnitude of the initial MR image as a height map in order to detect boundaries. The same gradient magnitude is used by the LS algorithm to derive the propagation term which plays a similar role in determining boundaries. Unlike the watershed algorithm, RG does not use the gradient

magnitude to detect boundaries, making it a better match to the LS algorithm for hybridization.

7.2 Other hybrid segmentation algorithms

To the author's knowledge, the hybrid algorithm developed in this thesis is the first to automatically contour bone erosions in 3D image sets for determination of erosion volume (Emond et al 2011). Although the hybrid approach to contouring bone erosions is unique, hybrid segmentation has been adopted for other medical imaging applications such as those described in chapter 4 which combined RG, fuzzy connectedness and LS (Franaszek et al 2001), LS and morphological reconstruction (Gu et al 2006) and LS and morphological scal-space analysis (Lee et al 2007). Unlike the hybrid algorithm developed in this thesis, none of these methods used logical operators to combine existing segmentation techniques.

7.3 Improving automation

A major goal in developing an algorithm able to segment bone erosions in MR images was automation. The hybrid algorithm developed in this thesis cannot be considered to be fully automated because of two user-required inputs: seed placement and selection of parameters which control the segmentation. Seed placement, has two purposes: to identify individual erosions and to provide an estimate of the centre of the erosion. In order to automate seed-placement, the

algorithm would also need to provide an estimate of the centre of the bone erosion. It is likely that any algorithm which tries to automatically identify the centre of an erosion from a 3D MR image set would have an unacceptable failure rate given the complexity of tissues present. In addition, automated seed placement is likely to reduce the accuracy and precision of measuring bone erosion volumes because the boundaries of the LS algorithm (which is used by the hybrid algorithm) are greatly dependent on the location of the seed point. However, it may be possible to automate seed placement in follow-up images. By using image registration to align the anatomy of baseline and follow-up images, the position of a seed point in baseline images could be used to automatically place the seed point in follow-up scans. This may be the focus of any future improvements to the algorithm.

The second factor which prevents full automation of bone erosion volume measurement is the selection of controlling parameters. Since it was not possible to select a single set of controlling parameters required by the hybrid algorithm which could successfully segment all erosions it was tested on, an operator is required to select one of five parameter sets. Different parameters are required because erosions do not have standardized features. Parameter sets were introduced to replace the necessity of selecting the large number of controlling parameters required by the hybrid algorithm to successfully identify the various

features of an erosion. The effect was to reduce the total number of parameters required by the user from 15 to 1 (a single selection of one of the 5 parameter sets). However, removing the ability to fine-tune individual parameters increases the failure rate and reduces the accuracy of bone erosion volume measurements. There were only 8 images included in the test-set used to determine the values of controlling parameters of each parameter set. The algorithms failure rate and accuracy may be improved by re-defining the parameter sets using a much larger test-set of images.

7.4 Advantages of this work

7.4.1 May be used by trained and untrained readers

Over the course of the project it became evident that there are two possible ways to use the automated segmentation algorithm to measure bone erosion volumes. The first is to have an untrained (non radiologist) reader follow a protocol which specifies exact procedures to take during each step of volume measurement. The second use is to provide the algorithm to a trained reader (a musculoskeletal radiologist) who can use it to quickly contour erosions before manually correcting where necessary.

The first method involves using software which drives the algorithm to measure erosion volumes without the use of a trained radiologist. When used in this way

the reader is provided with a specific protocol describing how to perform each step of the algorithm described in chapter 4: placing the initial seed point as close to the centre of the erosion as possible, selecting the parameter set which best contours the erosion (section 4.3) and iteratively re-positioning the seed point (section 4.4). The purpose of a protocol that specifically describes how to proceed at each step is to rely on the algorithm to contour accurately the erosion rather than the reader contouring the lesion. Though this may result in some erosions being inaccurately segmented (since the algorithm cannot outline perfectly every possible erosion shape), it allows for erosion volumes to be measured by untrained readers at a reasonable accuracy (figure 5.2) with high reproducibility (figure 5.1).

The second method involves using the software to segment erosions and, afterward, have a trained radiologist correct the contours. When used in this way a specific protocol does not need to be followed and the contours need not be accurate since the radiologist's manual corrections are relied upon to accurately measure erosion volumes. This provides the accuracy of erosion volumes as measured by a trained radiologist without the need for the tedious and time-consuming process of manually tracing erosions one slice at a time.

7.4.2 Time factor

The automation of contour placement around an erosion substantially decreases the overall time required for volume measurement, as indicated in table 5.2. A substantial decrease in processing time is most pronounced for larger erosion volumes (> 100 mm^3) since these erosions occupy more slices, thereby increasing the total number of contours which must be manually traced. For these larger volumes the algorithm is four times faster than manual tracing. Although volumes less than 100 mm^3 require substantially less time to trace manually than larger volumes, the algorithm reduced the processing time by at least a factor of two, without any loss of accuracy.

7.4.3 Field strength independence

Though the hybrid algorithm was developed using MR images acquired using a 1 Tesla peripheral scanner, it is not limited to images acquired by that scanner. The algorithm's controlling parameters, listed in table 4.2, are percentages of intensity with respect to the highest and lowest intensity in the MR scan. Therefore, bone erosions acquired by 1.5 and 3 Tesla full-body scanners could also be segmented by the hybrid algorithm.

7.5 Limitations of this work

7.5.1 Erosion size limitations

Due to partial volume averaging there is a lower limit to the volume size which can be accurately measured by the manual or automated methods. This limit is based on the voxel size of the MR image and is caused by the intrinsic uncertainty arising from partial volume averaging. Given that the voxel size in the study was $0.27 \times 0.27 \times 1.0$ mm^3 (out-of-plane voxel size is 3.7 times larger than in-plane voxel width) and assuming that erosions are approximately spherical in shape, the uncertainty of an erosion 3.2 mm wide, or having a volume of 17.8 mm^3, is approximately 10% (see figure 4.10). This approximation indicated that it was necessary to exclude erosions which did not occupy at least three consecutive 1.0 mm slices. This approximation is consistent with the RAMRIS recommendation that erosions only be scored if visible in two planes (Ostergaard et al 2003) when scanned with a typical slice thickness of 3 to 4 mm. The algorithm performs extremely well for volumes up to 175 mm^3.

7.5.2 True reproducibility

The aggregate reproducibility was not determined. Aggregate reproducibility would require scanning participants twice in a single visit. However, it was not possible to perform a second scan due to time constraints and participant

compliance. Many participants experience joint pain caused by rheumatoid arthritis during scanning due to prolonged periods of time positioned in the scanner.

7.5.3 Lack of a phantom

An imaging phantom was not used to calibrate the accuracy of volume measurement for manual or automated segmentations. Though there are many imaging phantoms available, none accurately represent the imaging characteristics of bone erosion caused by rheumatoid arthritis. A possible alternative to an imaging phantom is a cadaver with existing bone erosions. However, since it is not clear how a prosector would measure the volume of the absence of bone it may be impossible to use a cadavric specimen for this purpose.

7.6 Other applications

Although our hybrid RG/LS algorithm was applied to segment erosions in MR images of the hand, future work may include application of the algorithm to other pathologies, anatomical sites, and image modalities. The algorithm is sufficiently generic for application to other segmentation tasks wherein a region-based algorithm (such as RG) bleeds outside of an intended tissue boundary. Specifically, the algorithm could be applied to segmenting bone erosions in CT images, lung nodules in CT images, or brain tumours in MR and CT images.

7.7 Statistical Power

There were a total of 34 erosions included in the baseline study used to determine the accuracy and precision of automated erosion measurement. It took 14 months to identify these 34 erosions from a total of 234 participant MRIs screened. Of these erosions the volume measurements derived from the gold-standard tracings resulted in 13 erosions ≤ 50 mm^3, 11 erosions > 50 mm^3 and ≤ 100 mm^3 and 10 erosions > 100 mm^3. Using these erosion scans, the algorithm was tested across a wide range of clinically representative erosion sizes. Furthermore, there were a total of 16 erosions included in the follow-up study. Of these erosions, the difference in volume from baseline to follow-up determined using the gold-standard tracings resulted in 1 erosion < -30 mm^3, 3 erosions ≥ -30 mm^3 and < 0 mm^3, 10 erosions ≥ 0 mm^3 and < 30 mm^3 and 2 erosions > 30 mm^3. Consequently there was weak statistical power in measuring the accuracy of follow-up measurements in erosions who's differential volume is outside of the 0 to ± 30 mm^3 range. However, given that the choice of participants used for follow-up measurements was random, it is likely that this range is most common in erosions being treated by a rheumatologist.

Chapter 8

Conclusion

The hybrid segmentation algorithm described in this thesis is the first tool to automatically segment bone erosions from 3D MR images. It was important to develop this algorithm because the measurement of bone erosion volume is perhaps the best indicator of the progression of rheumatoid arthritis. The algorithm could be used to track bone erosion size in large populations, a task which previously required substantial time by a highly trained MSK radiologist who is required to manually trace the erosion boundaries.

At the time of this writing there is considerable debate as to whether the treatment of rheumatoid arthritis can reverse bone erosion damage. Since the algorithm is able to provide a quantitative measurement of erosion size, its use will help to clarify this debate. In addition, evolving treatment options, such as the use of biologics to treat RA, could be studied.

In conclusion, this thesis has described for the first time a hybrid segmentation algorithm which can segment bone erosions in 3D MR images with high accuracy and reproducibility. The application of the algorithm to various clinical studies will help to better define treatment options.

Bibliography

Y. Alamanos and A. A. Drosos. Epidemiology of adult rheumatoid arthritis. Autoimmun Rev, 4(3):130-136, Mar 2005.

Y. Alamanos, P. V. Voulgari, and A. A. Drosos. Incidence and prevalence of rheumatoid arthritis, based on the 1987 american college of rheumatology criteria: a systematic review. Semin Arthritis Rheum, 36(3):182-188, Dec 2006.

D. Aletaha, F. C. Breedveld, and J. S. Smolen. The need for new classification criteria for rheumatoid arthritis. Arthritis Rheum, 52(11):3333-3336, Nov 2005.

Aletaha D and Smolen J S. The definition and measurement of disease modification in inflammatory rheumatic diseases *Rheum. Dis. Clin. North. Am*. 32, 9–44, vii, 2006

D. Aletaha, T. Neogi, A. J. Silman, J. Funovits, D. T. Felson, C. O. Bingham 3rd, N. S. Birnbaum, G. R. Burmester, V. P. Bykerk, M. D. Cohen, B. Combe, K. H. Costenbader, M. Dougados, P. Emery, G. Ferraccioli, J. M. Hazes, K. Hobbs, T. W. Huizinga, A. Kavanaugh, J. Kay, T. K. Kvien, T. Laing, P. Mease, H. A. Ménard, L. W. Moreland, R. L. Naden, T. Pincus, J. S. Smolen, E. Stanislawska-Biernat, D. Symmons, P. P. Tak, K. S. Upchurch, J. Vencovsky, F. Wolfe and G. Hawker. 2010 rheumatoid arthritis classification criteria: an American College of Rheumatology/European League Against Rheumatism collaborative initiative. Ann Rheum Dis. 2010 Sep;69(9):1580-8.

A. Alonso-Ruiz, J. I. Pijoan, E. Ansuategui, A. Urkaregi, M. Calabozo, and A. Quintana. Tumor necrosis factor alpha drugs in rheumatoid arthritis: systematic review and metaanalysis of ecacy and safety. BMC Musculoskelet Disord, 9:52, 2008.

F. C. Arnett, S. M. Edworthy, D. A. Bloch, D. J. McShane, J. F. Fries, N. S. Cooper, L. A. Healey, S. R. Kaplan, M. H. Liang, and H. S. Luthra. The american rheumatism association 1987 revised criteria for the classification of rheumatoid arthritis. Arthritis Rheum, 31(3):315-324, Mar 1988.

M. Backhaus, T. Kamradt, D. Sandrock, D. Loreck, J. Fritz, K. J. Wolf, H. Raber, B. Hamm, G. R. Burmester, and M. Bollow. Arthritis of the finger joints: a comprehensive approach comparing conventional radiogra- phy, scintigraphy, ultrasound, and contrast-enhanced magnetic resonance imaging. Arthritis Rheum, 42(6):1232-1245, Jun 1999.

N. J. Bansback, D. A. Regier, R. Ara, A. Brennan, K. Shojania, J. M. Esdaile, A. H. Anis, and C. A. Marra. An overview of economic evaluations for drugs used in rheumatoid arthritis : focus on tumour necrosis factor-alpha antagonists. Drugs, 65(4):473-496, 2005.

K. A. Beattie, P. Boulos, M. Pui, J. O'Neill, D. Inglis, C. E. Webber, and J. D. Adachi. Abnormalities identified in the knees of asymptomatic volunteers using peripheral magnetic resonance imaging. Osteoarthritis Cartilage, 13 (3):181-186, Mar 2005.

N. Benton, N. Stewart, J. Crabbe, E. Robinson, S. Yeoman, and F. M. McQueen. Mri of the wrist in early rheumatoid arthritis can be used to predict functional outcome at 6 years. Ann Rheum Dis, 63(5):555-561, May 2004. Hans Berliner. The b* tree search algorithm: A best-first proof procedure. Artificial Intelligence, 12(1):23-40, May 1979.

P. Bird, M. Lassere, R. Shnier and J. Edmonds. Computerized measurement of magnetic resonance imaging erosion volumes in patients with rheumatoid arthritis: a comparison with existing magnetic resonance imaging scoring systems and standard clinical outcome measures *Arthritis Rheum.* 48, 614–624, 2003

P. Bird, F. Joshua, M. Lassere, R. Shnier, and J. Edmonds. Training and calibration improve inter-reader reliability of joint damage assessment using magnetic resonance image scoring and computerized erosion volume measurement. J Rheumatol, 32(8):1452-1458, Aug 2005.

J. M. Bland, D. G. Altman. Statistical methods for assessing agreement between two methods of clinical measurement. Lancet 1986;1:307-310

G. B. Bluhm, D. W. Smith and W. M. Mikulashek. A radiologic method of assessment of bone and joint destruction in rheumatoid arthritis *Henry Ford Hosp Med J*, 31, 152–161, 1983

N. Boutry, E. Hachulla, R. Flipo, B. Cortet, and A. Cotten. MR imaging findings in hands in early rheumatoid arthritis: comparison with those in systemic lupus erythematosus and primary sjgren syndrome. Radiology, 236(2):593-600, Aug 2005.

L. F. Callahan. The burden of rheumatoid arthritis: facts and figures. J Rheumatol Suppl, 53:8-12, Jul 1998.

R. A. D. Carano, J. A. Lynch, J. Redei, S. Ostrowitzki, Y. Miaux, S. Zaim, D. L. White, C. G. Peterfy, and H. K. Genant. Multispectral analysis of bone lesions in the hands of patients with rheumatoid arthritis. Magn Reson Imaging, 22(4):505-514, May 2004.

V. Caselles, R. Kimmel, and G. Sapiro. Geodesic active contours. International Journal of Computer Vision, 22(1):1573-1405, February 1997.

M. A. Cimmino, S. Innocenti, F. Livrone, F. Magnaguagno, E. Silvestri, and G. Garlaschi. Dynamic gadolinium-enhanced magnetic resonance imaging of the wrist in patients with rheumatoid arthritis can discriminate active from inactive disease. Arthritis Rheum, 48(5):1207-1213, May 2003.

P. G. Conaghan, P. O'Connor, D. McGonagle, P. Astin, R. J. Wakefield, W. W. Gibbon, M. Quinn, Z. Karim, M. J. Green, S. Proudman, J. Isaacs, and P. Emery. Elucidation of the relationship between synovitis and bone damage: a randomized magnetic resonance imaging study of individual joints in patients with early rheumatoid arthritis. Arthritis Rheum, 48(1):64-71, Jan 2003.

G. Cunnane, M. Doran, and B. Bresnihan. Infections and biological therapy in rheumatoid arthritis. Best Pract Res Clin Rheumatol, 17(2):345- 363, Apr 2003.

J. Dequeker. Arthritis in emish paintings (1400-1700). Br Med J, 1(6070): 1203-1205, May 1977.

J. Dequeker. Art, history and antiquity of rheumatic deseases., pages 31-37. Elsevier, Brussels, 1987.

P. Dieppe. Did galen describe rheumatoid arthritis? Ann Rheum Dis, 47(1): 84-85, Jan 1988.

E. W. Dijkstra. A note on two problems in connexion with graphs. Numerische Mathematik, 1:269-271, 1959.

U. Moller Dohn, B. J. Ejbjerg, M. Court-Payen, M. Hasselquist, E. Narvestad, M. Szkudlarek, J. M. Moller, H. S. Thomsen, and M. Ostergaard. Are bone erosions detected by magnetic resonance imaging and ultrasonography true erosions? a comparison with computed tomography in rheumatoid arthritis metacarpophalangeal joints. Arthritis Res Ther, 8(4):R110, 2006.

U. M. Dohn, A. Boonen, M. L. Hetland, M. S. Hansen, L. S. Knudsen, A. Hansen, O. R. Madsen, M. Hasselquist, J. M. Møller and M. Ostergaard. Erosive progression is minimal, but erosion healing rare, in rheumatoid arthritis patients

treated with adalimumab. a 1 year investigator-initiated follow-up study using high-resolution computed tomography as the primary outcome measure *Ann. Rheum. Dis.* 68, 1585-90, 2009

J. Duryea, Y. Jiang, M. Zakharevich and H. K. Genant. Neural network based algorithm to quantify joint space width in joints of the hand for arthritis assessment *Med. Phys.* 27, 1185–1194, 2000a

J. Duryea, J. Li, C. G. Peterfy, C. Gordon and H. K. Genant. Trainable rule-based algorithm for the measurement of joint space width in digital radiographic images of the knee *Med. Phys.* 27, 580–591, 2000b

J. Duryea, M. Magalnick, S. Alli, L. Yao, M. Wilson and R. Goldbach-Mansky. Semiautomated three-dimensional segmentation software to quantify carpal bone volume changes on wrist ct scans for arthritis assessment *Med. Phys.* 35, 2321–2330, 2008

P. D. Emond, D. Inglis, A. Choi, J. Tricta, J. D. Adachi and C. L. Gordon. Volume measurement of bone erosions in magnetic resonance images of patients with rheumatoid arthritis. Magnetic Resonance in Medicine, DOI: 10.1002/mrm.23037, in press (published online in June, 2011)

B. J. Ejbjerg, E. Narvestad, S. Jacobsen, H. S. Thomsen, and M. Ostergaard. Optimised, low cost, low field dedicated extremity mri is highly specific and sensitive for synovitis and bone erosions in rheumatoid arthritis wrist and finger joints: comparison with conventional high field mri and radiography. Ann Rheum Dis, 64(9):1280-1287, Sep 2005.

I. Eshed, C. E. Althoff, T. Schink, A. K. Scheel, C. Schirmer, M. Backhaus, A. Lembcke, M. Bollow, B. Hamm, and K-G. A Hermann. Low-field MRI for assessing synovitis in patients with rheumatoid arthritis. impact of gd-dtpa dose on synovitis scoring. Scand J Rheumatol, 35(4):277-282, 2006. E. D. Ferucci, D. W. Templin, and A. P. Lanier. Rheumatoid arthritis in american indians and alaska natives: a review of the literature. Semin Arthritis Rheum, 34(4):662-667, Feb 2005.

D. Foley-Nolan, J. P. Stack, M. Ryan, U. Redmond, C. Barry, J. Ennis, and R. J. Coughlan. Magnetic resonance imaging in the assessment of rheumatoid arthritis-a comparison with plain film radiographs. Br J Rheumatol, 30(2):101-106, Apr 1991.

M. Franaszek, R. M. Summers, P. J. Pickhardt, and J. R. Choi. Hybrid segmentation of colon filled with air and opacified fluid for CT colonography. IEEE Trans Med Imaging, 25(3):358-368, Mar 2006. S. E. Gabriel. The epidemiology of rheumatoid arthritis. Rheum Dis Clin North Am, 27(2):269-281, May 2001.

A. B. Garrod. The nature and treatment of gout and rheumatoid gout. Walton and Maberley, London, 1859.

H. K. Genant. Methods of assessing radiographic change in rheumatoid arthritis *Am. J. Med.* 75, 35–47, 1983

J. P. Gofton and W. M. O'Brien. Effects of auranofin on the radiological progression of joint erosion in rheumatoid arthritis *J. Rheumatol. Suppl.* 8, 169–172, 1982

S. R. Goldring. Periarticular bone changes in rheumatoid arthritis: pathophysiological implications and clinical utility. Ann Rheum Dis, 68(3):297-9, March 2009.

C. L. Gordon, C. Wu, C. G. Peterfy, J. Li, J. Duryea, C. Klifa and H. K. Genant. Automated measurement of radiographic hip joint-space width *Med. Phys.* 28, 267–277, 2001

P. Goupille, B. Roulot, S. Akoka, A. M. Avimadje, P. Garaud, L. Naccache, A. Le Pape, and J. P. Valat. Magnetic resonance imaging: a valuable method for the detection of synovial inammation in rheumatoid arthritis. J Rheumatol, 28(1):35-40, Jan 2001.

L. Gu, J. Xu, and T. M. Peters. Novel multistage three-dimensional medical image segmentation: methodology and validation. IEEE Trans Inf Technol Biomed, 10(4):740-748, Oct 2006.

P. E. Hart; N. J. Nilsson and B. Raphael. A formal basis for the heuristic determination of minimum cost paths. IEEE Transactions onSystems Science and Cybernetics, 4(2):100-107, July 1968.

K-G. A Hermann. [Magnetic resonance imaging of the hand in rheumatoid arthritis. new scientific insights and practical application]. Radiologe, 46(5): 384-393, May 2006.

J. B. Higgs, D. Smith, K. F. D. Rosier and R. W. Charlesworth. Quantitative measurement of erosion growth and joint space loss in rheumatoid arthritis hand radiographs *J. Rheumatol.* 23, 265–272, 1996

D. Hoa and A. Micheau. e-MRI, Magnetic Resonance Imaging physics and technique course on the web. Campus Medica, June 2008. URL http://www.e-mri.org/.

M. C. Hochberg, A. J. Silman, J. S. Smolen, M. E. Weinblatt, and M. H. Weisman, editors. Rheumatology, volume 1. Mosby, 3rd edition, 2003.

J. L. Hoving, R. Buchbinder, S. Hall, G. Lawler, P. Coombs, S. McNealy, P. Bird, and D. Connell. A comparison of magnetic resonance imaging, sonography, and radiography of the hand in patients with early rheumatoid arthritis. J Rheumatol, 31(4):663-675, Apr 2004.

J. Huang, N. Stewart, J. Crabbe, E. Robinson, L. McLean, S. Yeoman, P. L. Tan, and F. M. McQueen. A 1-year follow-up study of dynamic magnetic resonance imaging in early rheumatoid arthritis reveals synovitis to be increased in shared epitope-positive patients and predictive of erosions at 1 year. Rheumatology (Oxford), 39(4):407-416, Apr 2000.

D. Inglis, M. Pui, G. Ioannidis, K. Beattie, P. Boulos, J. D. Adachi, C. E. Webber, and F. Eckstein. Accuracy and test-retest precision of quantitative cartilage morphology on a 1.0 t peripheral magnetic resonance imaging system. Osteoarthritis Cartilage, 15(1):110-115, Jan 2007.

S. J. Jarrett, P. G. Conaghan, V. S. Sloan, P. Papanastasiou, C-E. Ortmann, P. J. O'Connor, A. J. Grainger, and P. Emery. Preliminary evidence for a structural benefit of the new bisphosphonate zoledronic acid in early rheumatoid arthritis. Arthritis Rheum, 54(5):1410-1414, May 2006.

C. Jorgensen, C. Cyteval, J. M. Anaya, M. P. Baron, J. L. Lamarque, and J. Sany. Sensitivity of magnetic resonance imaging of the wrist in very early rheumatoid arthritis. Clin Exp Rheumatol, 11(2):163-168, 1993.

J. H. Kellgren. Radiological signs of rheumatoid arthritis; a study of observer differences in the reading of hand films *Ann. Rheum. Dis.* 15, 55–60, 1956

E. Kirkhus, A. Bjornerud, J. Thoen, V. Johnston, K. Dale, and H-J. Smith. Contrast-enhanced dynamic magnetic resonance imaging of finger joints in

osteoarthritis and rheumatoid arthritis: an analysis based on pharmacokinetic modeling. Acta Radiol, 47(8):845-851, Oct 2006.

M. Klarlund, M. Ostergaard, and I. Lorenzen. Finger joint synovitis in rheumatoid arthritis: quantitative assessment by magnetic resonance imaging. Rheumatology (Oxford), 38(1):66-72, Jan 1999.

T. K. Kvien. Epidemiology and burden of illness of rheumatoid arthritis. Pharmacoeconomics, 22(2 Suppl):1-12, 2004.

A. Larsen. Radiological grading of rheumatoid arthritis. an interobserver study *Scand J. Rheumatol.* 2, 136–138, 1973

I. Leden, E. Persson, and O. Persson. Aspects of the history of rheumatoid arthritis in the light of recent osteo-archaeological finds. Scand J Rheumatol, 17(5):341-352, 1988.

N. Lee, A. F. Laine, and R. T. Smith. A hybrid segmentation approach for geographic atrophy in fundus auto-uorescence images for diagnosis of age-related macular degeneration. Conf Proc IEEE Eng Med Biol Soc, 2007:4965-4968, 2007.

H. Lindegaard, J. Vallo, K. Horslev-Petersen, P. Junker, and M. Ostergaard. Low field dedicated magnetic resonance imaging in untreated rheumatoid arthritis of recent onset. Ann Rheum Dis, 60(8):770-776, Aug 2001.

M. D. Lockshin. Sex differences in autoimmune disease. Orthop Clin North Am, 37(4):629-633, Oct 2006.

A. J. MacGregor. Classification criteria for rheumatoid arthritis. Baillieres Clin Rheumatol, 9(2):287-304, May 1995.

A. Maetzel, L. C. Li, J. Pencharz, G. Tomlinson, C. Bombardier, Community Hypertension, and Arthritis Project Study Team. The economic burden associated with osteoarthritis, rheumatoid arthritis, and hypertension: a comparative study. Ann Rheum Dis, 63(4):395-401, Apr 2004.

H. Mahdi, B. A. Fisher, H. Kallberg, D. Plant, V. Malmstrom, J. Ronnelid, P. Charles, B. Ding, L. Alfredsson, L. Padyukov, D. P. Symmons, P. J. Venables, L. Klareskog and K. Lundberg. Specific interaction between genotype, smoking and autoimmunity to citrullinated alpha-enolase in the etiology of rheumatoid arthritis. Nature Genetics. 41(12):1319-24, Dec 2009.

R. Malladi, J.A. Sethian, and B.C. Vemuri. Shape modeling with front propagation: a level set approach. 17(2):158-175, 1995. ISSN 0162-8828.

D. McGonagle, P. G. Conaghan, P. O'Connor, W. Gibbon, M. Green, R.Wakefield, J. Ridgway, and P. Emery. The relationship between synovitis and bone changes in early untreated rheumatoid arthritis: a controlled magnetic resonance imaging study. Arthritis Rheum, 42(8):1706-1711, Aug 1999.

F. McQueen, M. Ostergaard, C. Peterfy, M. Lassere, B. Ejbjerg, P. Bird, P. O'Connor, H. Genant, R. Shnier, P. Emery, J. Edmonds, and P. Conaghan. Pitfalls in scoring mr images of rheumatoid arthritis wrist and metacarpophalangeal joints. Ann Rheum Dis, 64 Suppl 1:i48-i55, Feb 2005.

F. M. McQueen and B. Ostendorf. What is mri bone oedema in rheumatoid arthritis and why does it matter? Arthritis Res Ther, 8(6):222, 2006.

F. M. McQueen, N. Stewart, J. Crabbe, E. Robinson, S. Yeoman, P. L. Tan, and L. McLean. Magnetic resonance imaging of the wrist in early rheumatoid arthritis reveals a high prevalence of erosions at four months after symptom onset. Ann Rheum Dis, 57(6):350-356, Jun 1998.

F. M. McQueen, N. Stewart, J. Crabbe, E. Robinson, S. Yeoman, P. L. Tan, and L. McLean. Magnetic resonance imaging of the wrist in early rheumatoid arthritis reveals progression of erosions despite clinical improvement. Ann Rheum Dis, 58(3):156-163, Mar 1999.

D. J. Miller-Blair, N. Tsuchiya, A. Yamaguchi, T. P. Kenny, and D. L. Robbins. Immunologic mechanisms in common rheumatologic diseases. Clin Orthop Relat Res, (326):43-54, May 1996.

H. J. Bernelot Moens, M. A. van de Laar, and J. K. van der Korst. Comparison of the sensitivity and specificity of the 1958 and 1987 criteria for rheumatoid arthritis. J Rheumatol, 19(2):198-203, Feb 1992.

C. R. Nave. Hyper Physics. Georgia State University, June 2008. URL http://hyperphysics.phy-astr.gsu.edu/hbase/hph.html.

D. G. Nishimura. Principles of Magnetic Resonance Imaging. Stanford University, 1996.

J. C. Oostveen, A. R. Roozeboom, M. A. van de Laar, J. Heeres, J. A. denBoer, and S. F. Lindeboom. Functional turbo spin echo magnetic resonance imaging

versus tomography for evaluating cervical spine involvement in rheumatoid arthritis. Spine, 23(11):1237-1244, Jun 1998.

G. Orozco, B. Rueda, and J. Martin. Genetic basis of rheumatoid arthritis. Biomed Pharmacother, 60(10):656-662, Dec 2006.

B. Ostendorf, R. Peters, P. Dann, A. Becker, A. Scherer, F. Wedekind, J. Friemann, K. P. Schulitz, U. Mdder, and M. Schneider. Magnetic resonance imaging and miniarthroscopy of metacarpophalangeal joints: sensitive detection of morphologic changes in rheumatoid arthritis. Arthritis Rheum, 44(11):2492-2502, Nov 2001.

M. Ostergaard, M. Hansen, M. Stoltenberg, P. Gideon, M. Klarlund, K. E. Jensen, and I. Lorenzen. Magnetic resonance imaging-determined synovial membrane volume as a marker of disease activity and a predictor of progressive joint destruction in the wrists of patients with rheumatoid arthritis. Arthritis Rheum, 42(5):918-929, May 1999.

M. Ostergaard, M. Klarlund, M. Lassere, P. Conaghan, C. Peterfy, F. McQueen, P. O'Connor, R. Shnier, N. Stewart, D. McGonagle, P. Emery, H. Genant, and J. Edmonds. Interreader agreement in the assessment of magnetic resonance images of rheumatoid arthritis wrist and finger joints- an international multicenter study. J Rheumatol, 28(5):1143-1150, May 2001.

M. Ostergaard, M. Hansen, M. Stoltenberg, K. E. Jensen, M. Szkudlarek, B. Pedersen-Zbinden, and I. Lorenzen. New radiographic bone erosions in the wrists of patients with rheumatoid arthritis are detectable with magnetic resonance imaging a median of two years earlier. Arthritis Rheum, 48(8):2128-2131, Aug 2003a.

M. Ostergaard, C. Peterfy, P. Conaghan, F. McQueen, P. Bird, B. Ejbjerg, R. Shnier, P. O'Connor, M. Klarlund, P. Emery, H. Genant, M. Lassere, and J. Edmonds. Omeract rheumatoid arthritis magnetic resonance imaging studies. core set of mri acquisitions, joint pathology definitions, and the omeract ra-mri scoring system. J Rheumatol, 30(6):1385-1386, Jun 2003b.

M. Ostergaard, A. Duer, H. Nielsen, J. S. Johansen, E. Narvestad, B. J. Ejbjerg, B. Baslund, J. M. Moller, H. S. Thomsen, and J. Petersen. Magnetic resonance imaging for accelerated assessment of drug effect and prediction of subsequent radiographic progression in rheumatoid arthritis: a study of patients receiving combined anakinra and methotrexate treatment. Ann Rheum Dis, 64(10):1503-1506, Oct 2005.

K. Palosaari, J. Vuotila, R. Takalo, A. Jartti, R. Niemel, M. Haapea, I. Soini, O. Tervonen, and M. Hakala. Contrast-enhanced dynamic and static MRI correlates with quantitative 99tcm-labeled nanocolloid scintigraphy. Study of early rheumatoid arthritis patients. Rheumatology (Oxford), 43(11):1364-1373, Nov 2004.

D. Perry, N. Stewart, N. Benton, E. Robinson, S. Yeoman, J. Crabbe, and F. McQueen. Detection of erosions in the rheumatoid hand; a comparative study of multidetector computerized tomography versus magnetic resonance scanning. J Rheumatol, 32(2):256-267, Feb 2005. F. Pucino, P. T. Harbus, and R. Goldbach-Mansky. Use of biologics in rheumatoid arthritis: where are we going? Am J Health Syst Pharm, 63(18 Suppl 4):S19-S41, Sep 2006.

C. Peterfy. Structural characterization of rheumatoid arthritis by mri: applications in clinical research and in clinical practice Musculoskelet. Neuronal. Interact. 4, 360–361, 2004

A. C. Rat and M. C. Boissier. Rheumatoid arthritis: direct and indirect costs. Joint Bone Spine, 71(6):518-524, Nov 2004.

T. Ray, D. S. Reddy, A. Mukherjee, J. Chatterjee, R. R. Paul and P. K. Dutta.. Detection of constituent layers of histological oral sub-mucous fibrosis: images using the hybrid segmentation algorithm. Oral Oncol, 44(12):1167-1171, Dec 2008.

J. Rogers and P. Dieppe. Skeletal palaeopathology and the rheumatic diseases: where are we now? Ann Rheum Dis, 49(11):885-886, Nov 1990.

B. M. Rothschild and R. J. Woods. Symmetrical erosive disease in archaic indians: the origin of rheumatoid arthritis in the new world? Semin Arthritis Rheum, 19(5):278-284, Apr 1990.

A. Saraux, J. M. Berthelot, G. Chals, C. Le Henaff, J. B. Thorel, S. Hoang, I. Valls, V. Devauchelle, A. Martin, D. Baron, Y. Pennec, E. Botton, J. Y. Mary, P. Le Goff, and P. Youinou. Ability of the american college of rheumatology 1987 criteria to predict rheumatoid arthritis in patients with early arthritis and classification of these patients two years later. Arthritis Rheum, 44(11):2485-2491, Nov 2001.

A. Savnik, H. Malmskov, H. S. Thomsen, T. Bretlau, L. B. Graff, H. Nielsen, B. Danneskiold-Samsoe, J. Boesen, and H. Bliddal. Mri of the arthritic small joints:

comparison of extremity mri (0.2 t) vs high-field mri (1.5 t). Eur Radiol, 11(6):1030-1038, 2001.

A. K. Scheel, K-G. A Hermann, S. Ohrndorf, C. Werner, C. Schirmer, J. Detert, M. Bollow, B. Hamm, G. A. Mller, G. R. Burmester, and M. Backhaus. Prospective 7 year follow up imaging study comparing radiography, ultra-sonography, and magnetic resonance imaging in rheumatoid arthritis finger joints. Ann Rheum Dis, 65(5):595-600, May 2006.

C. Schirmer, A. K. Scheel, C. E. Althoff, T. Schink, I. Eshed, A. Lembcke, G-R. Burmester, M. Backhaus, B. Hamm, and K-G. A Hermann. Diagnostic quality and scoring of synovitis, tenosynovitis and erosions in low-field mri of patients with rheumatoid arthritis: a comparison with conventional mri. Ann Rheum Dis, 66(4):522-529, Apr 2007.

H. Schoellnast, H. A. Deutschmann, J. Hermann, G. J Schaer, P. Reittner, F. Kammerhuber, D. H. Szolar, and K. W. Preidler. Psoriatic arthritis and rheumatoid arthritis: findings in contrast-enhanced mri. AJR Am J Roentgenol, 187(2):351-357, Aug 2006.

J. A. Sethian. Level Set Methods and Fast Marching Methods, chapter 8. Cambridge Press, second edition, 1999.

J. T. Sharp, M. D. Lidsky, L. C. Collins, and J. Moreland. Methods of scoring the progression of radiologic changes in rheumatoid arthritis. correlation of radiologic, clinical and laboratory abnormalities Arthritis Rheum. 14, 706–720, 1971

C. L. Short. The antiquity of rheumatoid arthritis. Arthritis Rheum, 17(3): 193-205, 1974.

K. Sievers. The rheumatoid factor in definite rheumatoid arthritis. an analysis of 1279 adult patients, with a follow-up study Acta. Rheumatol. Scand. Suppl. pp. SUPPL 9:1–SUPPL 121, 1965

O. J. Sommer, A. Kladosek, V. Weiler, H. Czembirek, M. Boeck and M. Stiskal. Rheumatoid arthritis: a practical guide to state-of-the-art imaging, image interpretation, and clinical implications Radiographics 25, 381–398, 2005

E. Snorrason. Landr-beauvais and his “goutte asthnique primitive”. Acta Med Scand Suppl, 266:115-118, 1952.

Softways. Magnetic Resonance - Technology Information Portal. Softways, June 2008. URL: www.mr-tip.com

E. Solau-Gervais, J-L. Legrand, B. Cortet, B. Duquesnoy, and R-M. Flipo. Magnetic resonance imaging of the hand for the diagnosis of rheumatoid arthritis in the absence of anti-cyclic cit-rullinated peptide antibodies: a prospective study. J Rheumatol, 33(9): 1760-1765, Sep 2006.

M. R. Spiegel. Fourier Analysis with Applications to Boundary Value Problems. Schaum's Outlines. McGraw-Hill, 1974.

O. Steinbrocker, C. H. Traeger and R. C. Batterman. Therapeutic criteria in rheumatoid arthritis *J Am. Med. Assoc.* 140, 659–662, 1949

H. Sugimoto, A. Takeda, J. Masuyama, and M. Furuse. Early-stage rheumatoid arthritis: diagnostic accuracy of mr imaging. Radiology, 198(1):185-192, Jan 1996.

H. Sugimoto, A. Takeda, and S. Kano. Assessment of disease activity in rheumatoid arthritis using magnetic resonance imaging: quantification of pannus volume in the hands. Br J Rheumatol, 37(8):854-861, Aug 1998.

S. Sykora. K-space formulation of MRI, volume I of Stan's Library. Extra Byte, June 2008.

D. Symmons, G. Turner, R.Webb, P. Asten, E. Barrett, M. Lunt, D. Scott, and A. Silman. The prevalence of rheumatoid arthritis in the united kingdom: new estimates for a new century. Rheumatology (Oxford), 41(7):793-800, Jul 2002.

D. P. Symmons, E. M. Barrett, C. R. Bankhead, D. G. Scott, and A. J. Silman. The incidence of rheumatoid arthritis in the united kingdom: results from the norfolk arthritis register. Br J Rheumatol, 33(8):735-739, Aug 1994.

P. P. Tak and B. Bresnihan. The pathogenesis and prevention of joint damage in rheumatoid arthritis: advances from synovial biopsy and tissue analysis. Arthritis Rheum, 43(12):2619-2633, Dec 2000.

N. Tanaka, H. Sakahashi, S. Ishii, E. Sato, K. Hirose, and T. Ishima. Synovial membrane enhancement and bone erosion by magnetic resonance imaging for prediction of radiologic progression in patients with early rheumatoid arthritis. Rheumatol Int, 25(2):103-107, Mar 2005.

B. Taouli, S. Zaim, C. G. Peterfy, J. A. Lynch, A. Stork, A. Guermazi, B. Fan, K. H. Fye, and H. K. Genant. Rheumatoid arthritis of the hand and wrist: comparison of three imaging techniques. AJR Am J Roentgenol, 182(4):937-943, Apr 2004.

J. Tehranzadeh, O. Ashikyan, J. Dascalos, and C. Dennehey. MRI of large intraosseous lesions in patients with inammatory arthritis. AJR Am J Roentgenol, 183(5):1453-1463, Nov 2004.

L. Terslev, S. Torp-Pedersen, A. Savnik, P. von der Recke, E. Qvistgaard, B. Danneskiold-Samsoe, and H. Bliddal. Doppler ultrasound and magnetic resonance imaging of synovial inammation of the hand in rheumatoid arthritis: a comparative study. Arthritis Rheum, 48(9):2434-2441, Sep 2003.

J. K. Udupa and S. Samarasekera. Fuzzy connectedness and object definition: theory, algorithms, and applications in image segmentation. Graphical Models and Image Processing, 58(3):246-261, 1996.

T. Uhlig and T. K. Kvien. Is rheumatoid arthritis disappearing? Ann Rheum Dis, 64(1):7-10, Jan 2005.

G. Valeri, C. Ferrara, P. Ercolani, E. De Nigris, and A. Giovagnoni. Tendon involvement in rheumatoid arthritis of the wrist: Mri findings. Skeletal Radiol, 30(3):138-143, Mar 2001.

D. M. van der Heijde, P. L. van Riel, I. H. Nuver-Zwart, F. W. Gribnau and L. B. vad de Putte. Effects of hydroxychloroquine and sulphasalazine on progression of joint damage in rheumatoid arthritis *Lancet* 1, 1036–1038, 1989

O. Vittecoq, T. Lequerre, V. Goeb, X. Le Loet, T. A. Abdesselam and N. Klemmer. Smoking and inflammatory diseases. Best Practice & Research in Clinical Rheumatology. 22(5):923-35, Oct 2008

C. M. Weyand. New insights into the pathogenesis of rheumatoid arthritis. Rheumatology (Oxford), 39 Suppl 1:3-8, Jun 2000.

G. M. Williams. Antitumor necrosis factor-alpha therapy and potential cancer inhibition. Eur J Cancer Prev, 17(2):169-177, Apr 2008.

L. Yao, M. Magalnick, M. Wilson, P. Lipsky, and R. Goldbach-Mansky. Periarticular bone findings in rheumatoid arthritis: T2-weighted versus contrast-enhanced t1-weighted mri. AJR Am J Roentgenol, 187(2):358-363, Aug 2006.

H. Yoshioka, S. Ito, S. Handa, S. Tomiha, K. Kose, T. Haishi, A. Tsutsumi, and T. Sumida. Low-field compact magnetic resonance imaging system for the hand and wrist in rheumatoid arthritis. J Magn Reson Imaging, 23(3):370-376, Mar 2006.

A. K. Zikou, M. I. Argyropoulou, P. V. Voulgari, V. G. Xydis, S. N. Nikas, S. C. Efremidis, and A. A. Drosos. Magnetic resonance imaging quantification of hand synovitis in patients with rheumatoid arthritis treated with adalimumab. J Rheumatol, 33(2)

Appendix

A.1 **Dijkstra's Algorithm**

```
function Dijkstra( graph[], start )
    visited[] ← ∅

    // Make cost of all but starting vertex infinite
    for all v in graph[] do
        cost[v] ← ∞
    end for
    cost[start] ← 0
    focus ← start

    // Loop until all vertices have been visited
    while visited[] ≠ graph[] do
        // Add all neighbours of focus that have not been visited
        // to the working set and set their parent to focus
        for all vertices v in neighbours( focus ) do
            if v ∉ visited[] then
                parent[v] ← focus
                working[] ← working[] + v
            end if
        end for

        // Mark the focus as visited and remove it from the
        // working set
        working[] ← working[] - focus
        visited[] ← visited[] + focus

        // For all vertices in the working set, calculate the cost
        // and set focus to the vertex with the minimum cost
        focus ← null
        for all v in working[] do
            cost[v] ← cost[parent[v]] + edgecost( parent[v], v )
            if cost[v] < cost[focus] then focus ← v
        end for
    end while
    return cost[]
end function
```

The set of all vertices in the graph is provided by `graph[]`, the initial starting vertex is `start` and the calculated lowest cost of traversal from the starting vertex to every other vertex in `graph[]` is returned as `cost[]`. The functions `neighbours(v)`, `cost(v)` and `edgecost(v1, v2)` return a set of all

vertices directly connected to vertex `v` by a single edge, the cost to traverse from the starting vertex to vertex `v` and the cost to traverse from vertices `v1` to `v2`, respectively. The algorithm is displayed visually in figure 3.3.

A.2 **Connected Thresholding (Region Growing)**

```
function ConnectedThresholding( intensity[], seeds[] )
    segmentation[] ← ∅
    working[] ← seeds[]

    while working ≠ ∅ do
        focus := first vertex in working[]
        for all voxels v in neighbours( focus ) do
            if v ∉ segmentation[] and intensity[v] ∈ [T_l, T_u]
                then working[] := working[] + v
            end if
            working[] := working[] – focus
            segmentation[] := segmentation + focus
        end for
    end while
    return segmentation[]
end function
```

In this algorithm the intensity of all voxels is provided by the set `intensity[]`, the seed points are provided by the set `seeds[]` and the function `neighbours(v)` returns a set of the 26 neighbouring voxels to `v`. When the algorithm is complete all voxels which belong to the segmentation will be included in the `segmentation[]` set. The algorithm is shown visually in figure 3.7.

A.3 **Fast Marching (Level Set)**

```
function FastMarching( intensity[], seed, stop )
    segmentation[] ← ∅
    time[] = InverseGradientMagnitude( intensity[] )

    cost[] ← ∅
    for all voxels v in intensity[] do
        // find the cost of traversal to v
        cost[v] := 0
        line[] ← all voxels in line joining seed and v
        for all voxels l in line[] do
            cost[v] := cost[v] + time[v]
        end for

        // include v if the cost is less than the stopping time
        if( cost[v] <= stop ) then
            segmentation[] := segmentation + v
        end if
    end for
    return segmentation[]
end function
```

In this algorithm the intensity of all voxels is provided by the set `intensity[]`, the seed point is provided by the voxel `seed`, the stopping time is provided by the scalar `stop` and the function `InverseGradientMagnitude(I)` returns a set of the inverse gradient magnitude the set `I`. When the algorithm is complete all voxels which belong to the segmentation will be included in the `segmentation[]` set. An example of the inverse gradient magnitude is shown in figure 3.9 and the algorithm is shown visually in figure 3.10.